

# Friction Stir Welding of Copper and Microstructure and Properties of the Welds

---

**Kati Savolainen**



# Friction Stir Welding of Copper and Microstructure and Properties of the Welds

**Kati Savolainen**

Doctoral dissertation for the degree of Doctor of Science in  
Technology to be presented with due permission of the School of  
Engineering for public examination and debate in Auditorium 216 at  
the Aalto University School of Engineering (Espoo, Finland) on the  
17th of February 2012 at 12 noon.

**Aalto University**  
**School of Engineering**  
**Department of Engineering Design and Production**  
**Engineering Materials**

**Supervisor**

Professor Hannu Hänninen

**Instructor**

Professor Hannu Hänninen

**Preliminary examiners**

Professor Hiroyuki Kokawa, Tohoku University, Japan

Professor Tuomo Tiainen, Tampere University of Technology, Finland

**Opponents**

Professor Hiroyuki Kokawa, Tohoku University, Japan

Dr. Sc. (Tech.) Martti Vilpas, STUK - Radiation and Nuclear Safety Authority, Finland

Aalto University publication series

**DOCTORAL DISSERTATIONS** 13/2012

© Kati Savolainen

ISBN 978-952-60-4500-9 (pdf)

ISSN-L 1799-4934

ISSN 1799-4942 (pdf)

Unigrafia Oy

Helsinki 2012

Finland

The dissertation can be read at <http://lib.tkk.fi/Diss/>

**Author**

Kati Savolainen

**Name of the doctoral dissertation**

Friction Stir Welding of Copper and Microstructure and Properties of the Welds

**Publisher** School of Engineering**Unit** Department of Engineering Design and Production**Series** Aalto University publication series DOCTORAL DISSERTATIONS 13/2012**Field of research** Engineering Materials**Manuscript submitted** 4 November 2011**Manuscript revised** 23 January 2012**Date of the defence** 17 February 2012**Language** English **Monograph** **Article dissertation (summary + original articles)****Abstract**

A reliable welding method producing joint properties as similar to those of the base materials as possible is needed in sealing the copper corrosion barrier of the final disposal canister for spent nuclear fuel. Friction stir welding (FSW) and electron beam welding (EBW) are currently the two potential methods.

FSW is a new and innovative joining method. It is a solid state method, where the detrimental phenomena related to melting do not occur. Other advantages include small and uniform grain size, equiaxed grains, random texture, as well as good mechanical properties of the joints. Friction stir processing (FSP) is a variation of FSW, and it is used to e.g. heal casting defects and improve corrosion properties.

The work in this Doctoral Thesis concentrated on FSW of copper and the microstructure of the welds as well as on the formation of the microstructure. The studied subjects include recrystallization, banding, as well as entrapped oxide particles and their influence on the localization of deformation. The results indicate that the microstructure and mechanical properties of the FSW welds are very similar to those of the base materials (unlike EB welds), making FSW a preferable method for sealing the canisters for spent nuclear fuel.

**Keywords** Friction stir welding, FSW, copper, oxide particles, microstructure**ISBN (printed)****ISBN (pdf)** 978-952-60-4500-9**ISSN-L** 1799-4934**ISSN (printed)** 1799-4934**ISSN (pdf)** 1799-4942**Location of publisher** Espoo**Location of printing** Helsinki**Year** 2012**Pages** 170**The dissertation can be read at** <http://lib.tkk.fi/Diss/>



**Tekijä**

Kati Savolainen

**Väitöskirjan nimi**

Kuparin kitkahitsaus pyörivällä työkalulla ja hitsien mikrorakenne ja ominaisuudet

**Julkaisija** Insinööritieteiden korkeakoulu**Yksikkö** Koneenrakennustekniikan laitos**Sarja** Aalto University publication series DOCTORAL DISSERTATIONS 13/2012**Tutkimusala** Materiaalitekniikka**Käsikirjoituksen pvm** 04.11.2011**Korjatun käsikirjoituksen pvm** 23.01.2012**Väitöspäivä** 17.02.2012**Kieli** Englanti **Monografia** **Yhdistelmäväitöskirja (yhteenveto-osa + erillisartikkelit)****Tiivistelmä**

Ydinjätteen loppusijoittamisessa käytettävien kuparista valmistettujen korroosionestokapseleiden sulkemiseen tarvitaan luotettava hitsausmenetelmä. Hitsausliitosten ominaisuuksien tulee olla mahdollisimman samanlaiset verrattuna perusaineen ominaisuuksiin. Kitkahitsaus pyörivällä työkalulla ja elektronisuihkuhitsaus ovat tällä hetkellä mahdolliset vaihtoehdot.

Kitkahitsaus pyörivällä työkalulla (tunnetaan myös kitkatappihitsauksena) on uusi ja innovatiivinen liittämismenetelmä. Koska liittäminen tapahtuu kiinteässä tilassa, sulamiseen ja jähmettymiseen liittyviä hitsausvirheitä ei muodostu. Menetelmän muita etuja ovat hitsiaineen pieni raekoko, tasainen ja suuntautumaton raerakenne sekä hyvät mekaaniset ominaisuudet. Kitkaprocessointi pyörivällä työkalulla on kitkatappihitsauksen variaatio, jota käytetään mm. valuvirheiden korjaamiseen sekä korroosio-ominaisuuksien parantamiseen.

Tässä väitöskirjassa tehty työ keskittyi kuparin kitkahitsaukseen pyörivällä työkalulla sekä hitsien mikrorakenteeseen ja sen muodostumiseen. Tutkittuja aiheita olivat mm. rekristallisaatio, nauharakenne (banding), oksidipartikkelit ja deformaation paikallistuminen. Tulokset osoittavat, että kitkatappihitsien mikrorakenne ja mekaaniset ominaisuudet ovat hyvin samankaltaiset verrattuna perusaineisiin (päinvastoin kuin elektronisuihkuhitseillä). Kitkatappihitsaus vaikuttaa siten paremmalta vaihtoehdolta ydinjätteen loppusijoituksessa käytettävien kuparikapseleiden sulkemiseen.

**Avainsanat** Kitkahitsaus pyörivällä työkalulla, kitkatappihitsaus, kupari, oksidipartikkelit, mikrorakenne**ISBN (painettu)****ISBN (pdf)** 978-952-60-4500-9**ISSN-L** 1799-4934**ISSN (painettu)** 1799-4934**ISSN (pdf)** 1799-4942**Julkaisupaikka** Espoo**Painopaikka** Helsinki**Vuosi** 2012**Sivumäärä** 170**Luettavissa verkossa osoitteessa** <http://lib.tkk.fi/Diss/>



## **PREFACE**

The research for this Doctoral Thesis was mainly carried out in the Laboratory of Engineering Materials at Aalto University – School of Engineering (formerly Helsinki University of Technology). The work was carried out during three projects (STIR, KUUMA, and KYT). Funding by Tekes, KYT2010 and KYT2014 research programs, and participating companies is gratefully acknowledged.

I am grateful for the help and guidance of several people. Most of all, I wish to thank Professor Hannu Hänninen for his encouragement and his ability to inspire. I also thank Mr. Tapio Saukkonen for his help with SEM and EBSD and Mr. Jari Hellgren for his enthusiasm and tireless efforts in improving FSW at the laboratory. Mr. Kim Widell is acknowledged for tensile testing and optical strain measurements and Ms. Laura Tiainen for her help in sample preparation. I am grateful to many others in the staff of the Laboratory of Engineering Materials. I have enjoyed my years there, it has been a wonderful place to work.

I would also like to acknowledge the FSW society. There are so many nice people with wonderful minds and lots of ideas.

Special thanks go to my family and friends, who helped in keeping my working life and private life in balance. My parents, my husband Jukka, and Vanilja, my bunny and constant companion during the writing of this Doctoral Thesis are all especially appreciated.

Kati Savolainen

## CONTENTS

Preface .....	7
Contents .....	8
List of Abbreviations and Symbols .....	12
Original Features .....	14
1 Introduction .....	16
1.1 Background and Motivation .....	16
1.2 Structure of the Thesis .....	18
2 Friction Stir Welding of Copper .....	20
2.1 Process .....	20
2.1.1 Principle .....	20
2.1.2 Material Flow .....	21
2.1.3 Welding Parameters .....	28
2.2 Tool .....	30
2.2.1 Tool Geometry .....	31
2.2.2 Tool Material .....	32
2.3 Microstructure of the Welds .....	33
2.3.1 Zones of FSW Welds .....	34
2.3.2 Grain Size .....	36
2.4 Banding .....	36
2.5 Copper as Base Material in FSW .....	40
2.5.1 Properties of Copper .....	40
2.5.2 Flow Stress .....	41
2.5.3 Dynamic Recrystallization .....	42
3 Friction Stir Processing .....	45
3.1 Process .....	46
3.2 Tool .....	47
3.3 FSP of Copper .....	48
4 Dissimilar Metal Welding .....	49
4.1 FSW of Dissimilar Materials .....	49
4.2 Cu/Al Dissimilar Metal FSW .....	50
5 Entrapped Oxide Particles .....	54

6	Welding Defects .....	56
6.1	Formation of Welding Defects.....	56
6.2	Welding Defects in Copper FSW Welds.....	57
6.2.1	Voids .....	57
6.2.2	Lack of Penetration .....	59
6.2.3	Entrapped Oxide Particles .....	60
6.2.4	Joint Line Hooking.....	62
6.2.5	Faying Surface Flaw.....	63
6.2.6	Tool Trace Material.....	64
6.2.7	Pores .....	65
7	Mechanical Properties of the Welds .....	66
7.1	Tensile Tests .....	66
7.2	Hardness Profiles .....	67
8	Objective of the Doctoral Thesis .....	68
9	Experimental .....	69
9.1	Base Materials.....	69
9.2	Tools.....	71
9.3	Arrangements .....	73
9.4	Welding Trials.....	74
9.5	Experimental Methods.....	75
9.5.1	Sample Preparation .....	75
9.5.2	Optical Microscopy .....	76
9.5.3	Scanning Electron Microscopy .....	76
9.5.4	Electron Backscatter Diffraction.....	76
9.5.5	Tensile Tests .....	77
9.5.6	Hardness Measurements .....	78
9.5.7	Bend Tests .....	78
9.5.8	Optical Strain Measurement .....	79
9.5.9	Hydrogen Annealing .....	80
9.5.10	Electrical Resistivity Measurements .....	80
9.5.11	Temperature and Power Measurements .....	81
10	Results.....	82
10.1	Microstructure.....	82
10.1.1	Grain Structure.....	82

10.1.2	Grain Size .....	85
10.1.3	Texture.....	88
10.1.4	Precipitates.....	88
10.2	Banding.....	91
10.3	Cu/Al Dissimilar Metal FSW.....	95
10.3.1	Tensile Tests .....	98
10.3.2	Hardness Profiles .....	98
10.3.3	Electrical Resistivity .....	99
10.3.4	Intermetallic Compounds .....	100
10.4	Entrapped Oxide Particles .....	104
10.4.1	Origin of Entrapped Oxide Particles .....	104
10.4.2	Avoidance of Entrapped Oxide Particles .....	106
10.4.3	Pinning Effect of Entrapped Oxide Particles.....	115
10.5	Optical Strain Measurement .....	117
10.6	Mechanical Properties of the Welds.....	120
10.6.1	Tensile Tests .....	120
10.6.2	Hardness Profiles .....	131
10.6.3	Bend tests.....	134
10.7	Temperature Measurements.....	135
11	Discussion .....	137
11.1	FSW of Copper and Copper Alloys .....	137
11.2	Microstructure of the Welds .....	137
11.2.1	Grain Structure.....	137
11.2.2	Grain Size .....	138
11.2.3	Texture.....	138
11.2.4	Precipitates.....	139
11.3	Banding.....	139
11.4	Cu/Al Dissimilar Metal FSW Welds.....	140
11.4.1	Tensile Tests .....	141
11.4.2	Hardness Tests .....	141
11.4.3	Electrical Resistivity/Conductivity .....	141
11.4.4	Intermetallic Compounds .....	142
11.5	Entrapped Oxide Particles .....	143
11.6	Localization of Plastic Strain.....	145

11.7	Mechanical Properties of FSW Joints .....	146
11.7.1	Tensile tests .....	146
11.7.2	Hardness profiles.....	147
11.7.3	Bend tests.....	148
12	Conclusions .....	149
13	Suggestions for Future Work .....	151
14	References.....	153

## LIST OF ABBREVIATIONS AND SYMBOLS

BSE	Backscattered electron
CCD	Charge-coupled device
CDRX	Continuous dynamic recrystallization
CS4	Convex scrolled shoulder step spiral pin tool
Cu-DHP	Phosphorus-deoxidized copper, high residual phosphorus
Cu-OF	Oxygen-free copper
Cu-OFHC	Oxygen-free high conductivity copper
Cu-OFP	Oxygen-free phosphorus-doped copper
$D_0$	Original grain size
DRX	Dynamic recrystallization
$D_s$	Steady-state grain size
EBSD	Electron backscatter diffraction
EBW	Electron beam welding
EDS	Energy dispersive x-ray spectroscopy
fcc	Face-centred cubic (crystal structure)
FSP	Friction stir processing
FSW	Friction stir welding
HAZ	Heat affected zone
HV	Hardness (Vickers)
IMC	Intermetallic compound
IPF	Inverse pole figure
JLH	Joint line hooking
NDT	Non-destructive testing
LOP	Lack of penetration
ODS	Oxide dispersion strengthened alloys
PCBN	Polycrystalline cubic boron nitride
PVD	Physical vapour deposition
Q	Activation energy for deformation
R	Gas constant
SEM	Scanning electron microscopy
SiC	Silicon carbide

SFE	Stacking fault energy
SKB	The Swedish Nuclear Fuel and Waste Management Co.
T	Absolute temperature (in K)
TEM	Transmission electron microscopy
TMAZ	Thermo-mechanically affected zone
TWI	The Welding Institute
X force	Force in the welding direction
XRD	X-ray diffraction
Z	Zener-Hollomon parameter
Z force	Downward force
$\dot{\epsilon}$	Strain rate
4NCu	Copper with 99.99 mass percent purity
7NCu	Copper with 99.99999 mass percent purity

## ORIGINAL FEATURES

This thesis addresses many aspects of friction stir welding of copper. The following features are believed to be original:

1. The confirmation of the existence of entrapped oxide particles in copper FSW welds.
2. A detailed understanding of the entrapped oxide particles in copper friction stir welds, including their origin and formation. Development of a feasible way of avoiding entrapped oxide particles in copper friction stir welds. The successful method is a combination of oxide removal from the butting faces and the use of inert shielding gas during welding.
3. In the most critical application of FSW of copper, 50 mm thick corrosion barrier canisters for the final disposal of spent nuclear fuel, it was discovered that plastic deformation and the resulting ductile fracture in FSW welds localise mainly on a processing line or occasionally on the line of entrapped oxide particles.
4. Different testing methods revealed that the microstructure, texture, and mechanical properties of copper friction stir welds are similar to those of the base materials in hot deformed or annealed state.
5. The comparison of different parts of the spent nuclear fuel canister (base materials as well as FSW and EB welds) using almost the entire material or weld thickness samples revealed that the mechanical properties of the FSW welds are significantly better than those of the welds produced by the other possible method, electron beam welding.
6. Banding in copper FSW welds consists of layers (bands) with smaller and larger grain sizes. The amount of local misorientation is higher in the bands of smaller grain size than in the bands of larger grain size. Contrary to aluminium FSW welds, the copper FSW welds exhibit almost random texture and no texture changes between the bands of smaller and larger grain sizes.

7. Defect-free dissimilar metal welds were produced between copper and aluminium.  
The welds exhibit very good tensile strength and electrical properties.

# 1 INTRODUCTION

## 1.1 Background and Motivation

Friction stir welding (FSW) is a new, innovative welding method where joining occurs in the solid state. Properties of the welds (for example in aluminium alloys) are similar to those of the base material. FSW welds have high strength, increased fatigue life, smaller residual stresses, and higher corrosion resistance as compared to welds produced by fusion welding methods. FSW is widely used in many industries for joining aluminium alloys. The applications include space shuttles, air planes, amphibious assault vehicles for the US Marine Corps, trains, ships, components for the automotive industry, etc. There are few industrial applications for FSW of copper. One of them is the fabrication of water-cooled backing plates (Okamoto et al. 2001). (Threadgill and Nunn 2003; Kallee and Nicholas 1998; Colligan et al. 2003; Arbegast 2006)

Friction stir processing (FSP) is a variation of FSW. It is used, for example, in marine propellers to improve the corrosion properties and to heal shrinkage porosity (Mahoney et al. on-line; Mahoney and Lynch on-line). It can also be used to create high strain rate superplasticity and to produce surface composites (Mahoney et al. 2001a; Mahoney et al. 2001b; Mishra et al. 2003).

Copper has many good properties (such as high electrical and thermal conductivity, excellent corrosion resistance, and good formability) which cannot be fully utilized due to restrictions in its weldability. Copper is difficult to join using conventional fusion welding methods due to its high thermal conductivity. FSW is suitable for joining copper because the heat is created on the spot by friction between the tool and the base material.

The most important and critical application of FSW in joining copper is the corrosion barrier canister for spent nuclear fuel. The plan is to encapsulate the spent nuclear fuel after cooling. The fuel elements will be placed in a cast iron insert which provides the mechanical strength, surrounded by a copper canister which acts as a corrosion barrier. The canisters will be deposited 500 m deep in the crystalline bedrock embedded in bentonite clay. Figure 1 shows the different barriers in the final disposal of spent nuclear fuel. (Andersson and Andrews 1999)

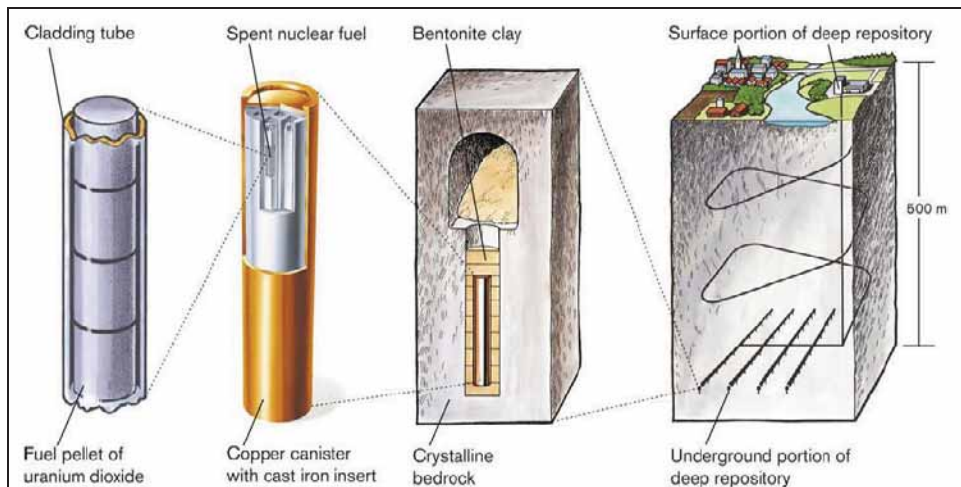


**Figure 1. System for the disposal of spent nuclear fuel (Cederqvist 2006).**

The spent nuclear fuel should be contained in the canisters for at least 100 000 years, until the radiation is on a safe level. Copper is selected due to its good corrosion properties under the repository conditions. Due to the reducing environment many materials, e.g. stainless steel, would corrode quickly as the protective oxide layer could not renew itself. Copper is also deformed readily, thus accommodating, e.g., rock displacements assuring the leak-tightness of the copper canister.

The copper corrosion barrier is a crucial part of the system for the disposal of spent nuclear fuel. The canisters will be made of phosphorus-doped oxygen-free copper (Cu-OFP). The addition of about 50 ppm of phosphorus improves the creep properties of the copper significantly. The grain size of the copper must be 360  $\mu\text{m}$  or smaller in order to guarantee a hot-worked condition and suitability for ultrasonic inspection. The grain size requirement is readily fulfilled using FSW, whereas the grain size in electron beam welds (EBW) can be up to 12-15 mm. The canister thickness will be 50 mm, diameter 1050 mm, and the length and weight will vary depending on the fuel type (3600-5250 mm and 5300-7585 kg, respectively). The lid (and the bottom when not using tubes with integrated bottoms) will be joined to the tube by either FSW or EBW. It is estimated that approximately 3000 canisters will be used in Finland and 6000 canisters in Sweden. The Swedish Nuclear Fuel and Waste Management Co. (SKB) has chosen FSW as their reference method, whereas

Posiva Oy in Finland is studying the use of EBW. (Andersson et al. 2000; Andersson and Andrews 1999; Cederqvist and Andrews 2003; Raiko 2005; SKB 2007)

Despite their many advantages, FSW and FSP are fairly unknown and little used in Finland. Improving the knowledge level on the methods could lead to benefits in many industries. FSW of copper in particular is very interesting, as it will be used in the final disposal of spent nuclear fuel. It is important to understand the factors influencing FSW of copper to ensure the best possible weld quality and safe final disposal.

## **1.2 Structure of the Thesis**

This Doctoral Thesis consists of a theoretical section (Chapters 2-7) describing the state-of-the-art of FSW and FSP of copper and an experimental section (Chapters 8-11) describing the objective, experimental methods, results, and discussion, followed by conclusions and suggestions for future work. The contents of the Chapters are as follows:

Chapter 2 gives an overview of FSW of copper. The welding process, material flow, microstructure, banding, and welding parameters are described, along with tool geometry and materials. Then the role of copper as base material and factors such as flow stress and dynamic recrystallization are considered.

Chapter 3 introduces FSP, the most important variation of FSW. A general description of the process and the tool geometry as well as the resulting improvements in microstructure and other properties as compared to the as-manufactured state are given and FSP of copper is discussed.

Chapter 4 concentrates on dissimilar metal welding. FSW is used to join different aluminium alloys together as well as aluminium to copper, steel, magnesium, titanium, etc. Emphasis is on FSW of copper to aluminium. The method, resulting microstructure, and the formation of intermetallic compounds are described.

Chapter 5 focuses on entrapped oxide particles in FSW welds. The origin, avoidance, and effect of entrapped oxide particles are discussed.

Chapter 6 concentrates on welding defects in copper FSW welds. Welding defects in copper FSW welds are different from those in fusion welds and also from those in aluminium FSW welds. A classification of the welding defects is provided along with a description of the welding defects and their formation.

Chapter 7 describes the mechanical properties of copper FSW welds. Tensile properties and hardness profiles of copper FSW welds are described.

Chapter 8 outlines the objective as well as the scope of this Doctoral Thesis.

Chapter 9 describes the experimental investigations of this Doctoral Thesis. The subjects include base materials, tool materials and geometries, arrangements, welding trials, and experimental methods. The used experimental methods were sample preparation, optical microscopy, SEM, EBSD, tensile testing, hardness measurements, three-point bend tests, electric resistivity measurements, and optical strain measurement.

Chapter 10 shows the results obtained in this Doctoral Thesis. Results include the microstructure and mechanical properties of copper and Cu/Al dissimilar metal FSW welds as well as the localization of plastic deformation in different parts of the copper corrosion barrier canister for spent nuclear fuel and entrapped oxide particles in copper FSW welds.

Chapter 11 contains the discussion of obtained results. Results are also compared to those of other studies.

Chapter 12 provides the conclusions of the Doctoral Thesis.

Chapter 13 suggests topics for future research.

## **2 FRICTION STIR WELDING OF COPPER**

FSW is a new welding method invented at The Welding Institute (TWI) in UK in 1991. It is a solid state joining method and therefore the defects of fusion welding due to the liquid state, such as solidification cracking, are either greatly diminished or completely avoided. It offers excellent weld quality with mechanical properties generally equal or superior to those of the base material, especially as compared to fusion welding methods. There is no steep gradient in the joint properties or microstructure. Additionally, it is safe, clean, and environmentally friendly. It does not require expensive filler wires or high level of operator skill or training, and it can take place in all positions from downhand to overhead. At the moment it is mainly used for joining aluminium alloys, although it is feasible for a variety of materials, including steel as well as copper, nickel, and titanium alloys. (Dawes 1995; Threadgill and Nunn 2003; Arbegast 2006; Ahmed et al. 2008)

### **2.1 Process**

Even though the principle of FSW is simple, the mechanisms behind the formation of the weld are very complex (De Vuyst et al. 2006). Material flow during FSW is dependent on the base material, tool geometry, and welding parameters.

#### **2.1.1 Principle**

The principle of FSW is as follows. A non-consumable, rotating tool is plunged between the rigidly clamped pieces to be welded. Heat generated by friction between the tool and the base material and plastic shear deformation softens the base material but does not melt it. Frictional heating dominates in the upper region of the weld and plastic work-induced heating in the lower region (Song and Kovecevic 2003; Colligan and Mishra 2008). As the tool is moved along the joint line, the butting surfaces are “stirred” together by the severe plastic flow around the rotating tool. The tool transports the plasticized base material from the leading side of the tool to the trailing side of the tool in a manner similar to extrusion or forging. On the trailing side of the tool, the material cools and a solid-state weld is formed. Figure 2 shows a schematic presentation of the FSW process and the main terminology.

(Thomas et al. 1991; Dawes 1995; Shercliff and Colegrove 2002; Threadgill and Nunn 2003; Kallee and Nicholas 1998; Ahmed et al. 2008; Çam 2011)

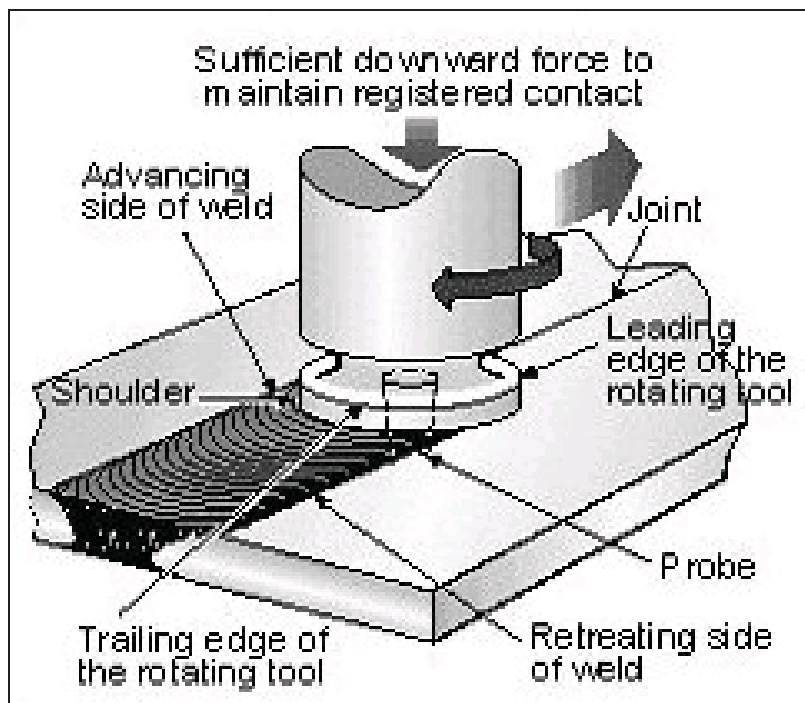


**Figure 2. A schematic presentation of the friction stir welding process with the main terminology (Kallee and Nicholas 1998).**

Local melting of the base material near the tool is a much debated topic. There is no microstructural evidence of melting, and furthermore, local melting generally does not cause problems related to bulk melting, such as hot cracking, observed in fusion welds. Colegrove and Shercliff (2005) suggest that at higher temperatures slip (instead of stick condition) occurs reducing heat generation and, consequently, avoiding material melting. An alternative theory by Seidel and Reynolds (2001) is that heat generation is reduced by material softening at higher temperatures.

### 2.1.2 Material Flow

The base material is moved by the tool in a flowing manner during FSW. The material flow is very complex and it depends on tool design, welding parameters, base material, and the contact condition between the tool and the base material. The material flow is very

different on the advancing side as compared to the retreating side. While material on the retreating side is merely wiped from the front of the tool to behind it, the flow of the material on the advancing side is much more complex (Figure 3). The material on the advancing side enters a rotational zone close to the probe, rotating for one or several revolutions before being deposited behind the tool over a much wider region. The more the material from the advancing side is rotated around the tool probe, the more highly deformed it becomes. According to the marker material studies, most of the material ends up behind its original position, the distance of about one probe diameter. A final position in front of the original position is noticed mainly near the tool shoulder. Some studies show evidence of vertical displacement due to the downward force caused by the tool threads. (Guerra et al. 2003; Schmidt et al. 2006; Zettler et al. 2006; Zhang et al. 2005; Seidel and Reynolds 2001; Zhang et al. 2007; Guerra et al. 2001; London et al. 2003; De Vuyst et al. 2006)

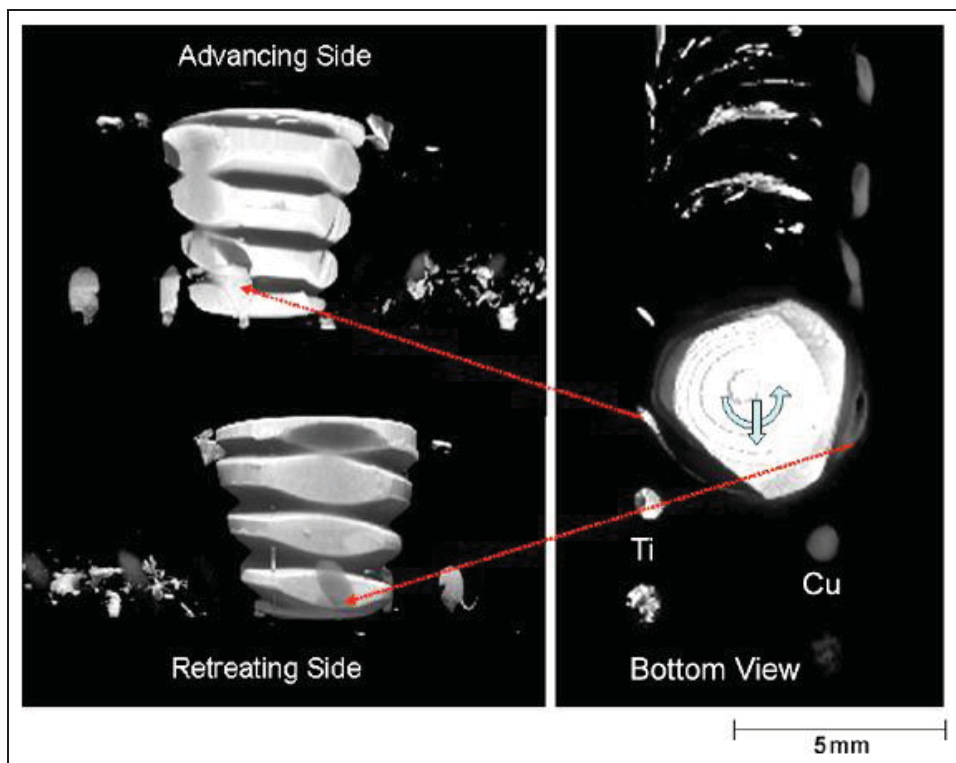


**Figure 3. Displacement of marker materials (titanium on the advancing side and copper on the retreating side) during FSW of an aluminium alloy (Zettler et al. 2006).**



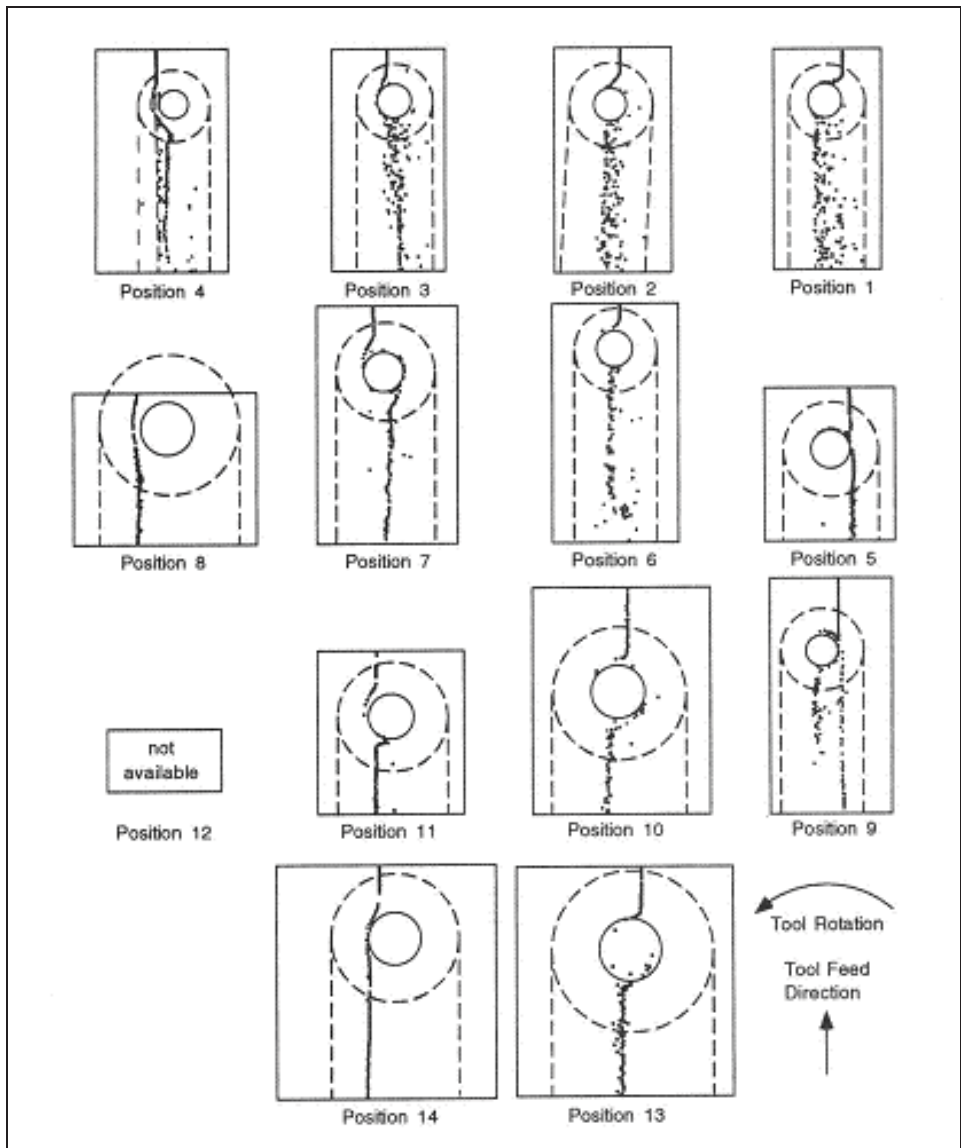
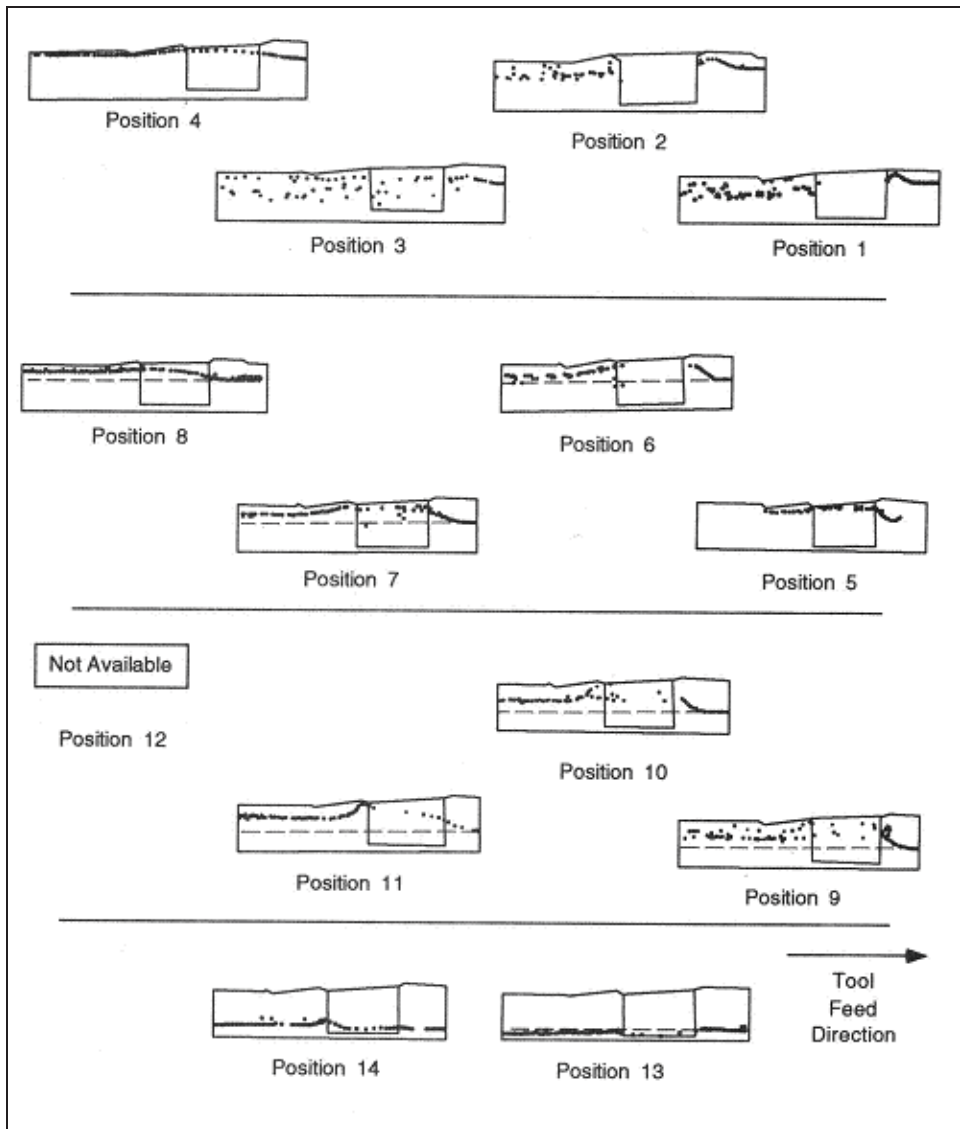


Figure 5. Horizontal view of the positions of the steel shot tracer material in aluminium alloy 7075-T6 FSW welds (Colligan 1999).



**Figure 6. Side view of the positions of the steel shot tracer material in aluminium alloy 7075-T6 FSW welds (Colligan 1999).**

Schneider et al. (2006) introduced a model of the flow components in FSW (Figure 7) based on marker material studies using lead embedded in aluminium alloy 2195-T81. The flow components are rigid body rotation, uniform translation, and ring vortex. The rigid body rotation represents the material surrounding the tool and rotating with it. It is separated from the rest of the weld metal by a cylindrical shearing surface of velocity discontinuity. The uniform translation denotes the tool traverse velocity. It is a homogeneous, constant velocity flow field. The ring vortex encircling the tool represents

the effects of axial motion. The downward flow is caused by the features of the tool probe and shoulder. The upward flow at a greater radius results from the backing plate (under the pieces to be welded) changing the direction of the downward flow. Only the radial components of the ring vortex flow interact with the two other flow components, leading to lateral shifts of the tracers. Heurtier et al. (2006) presented essentially the same flow components as Schneider et al.'s (2006) model. They concluded that as the material on the advancing side spends a longer time in the ring vortex field and is more affected by it, the strain and the resulting grain structure refinement are higher on the advancing side as compared to the retreating side.

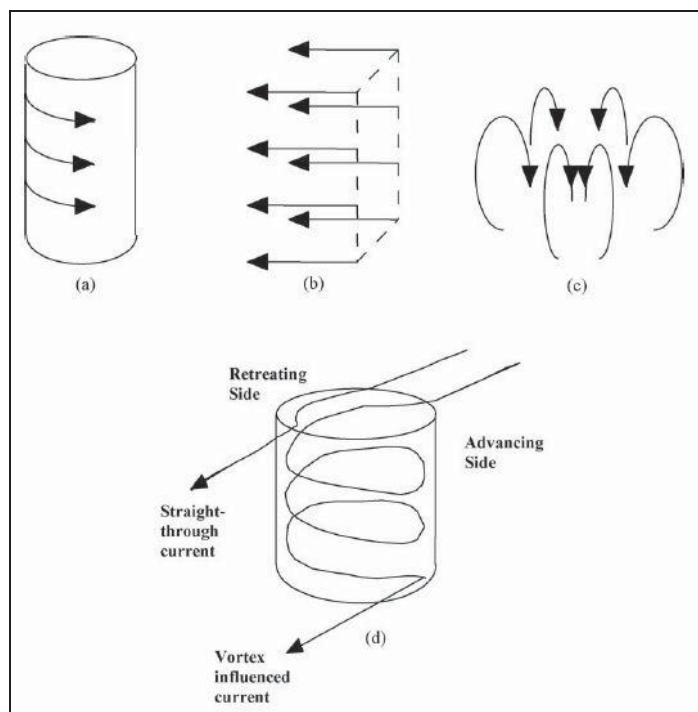


**Figure 7. Schematic of the flow fields in FSW by Schneider et al. (2006). The flow components are rigid body rotation (a), uniform translation (b), and ring vortex (c). The combined effect of these is seen in (d).**

Schmidt et al. (2006) studied material flow in FSW of aluminium alloy AA2024-T3 and presented a somewhat different model for the material flow. They concluded that there are several flow zones (e.g. rotation zone, transition zone, and deflection zone), as seen in Figure 8, which are closely linked to the corresponding material flow. Figure 9 shows computer tomography images of horizontal sections of AA2024-T3 joints with copper

strips as marker material in different configurations, demonstrating the model of Schmidt et al. (2006). Advancing side of the weld is on the right and traverse direction is from the bottom to the top of the figures. Figure 9b illustrates the presence of marker material traces several probe diameters in front of the original marker material line, indicating that the material has been transported forward in the rotation zone. It is assumed that the marker material has first entered the transition zone, moved forward in the rotation zone, and then back to the transition zone, from which it is deposited. However, even though traces of the marker material are deposited in front of the original marker material line, most of it is deposited behind the original line, as can be seen in Figures 9b and c.

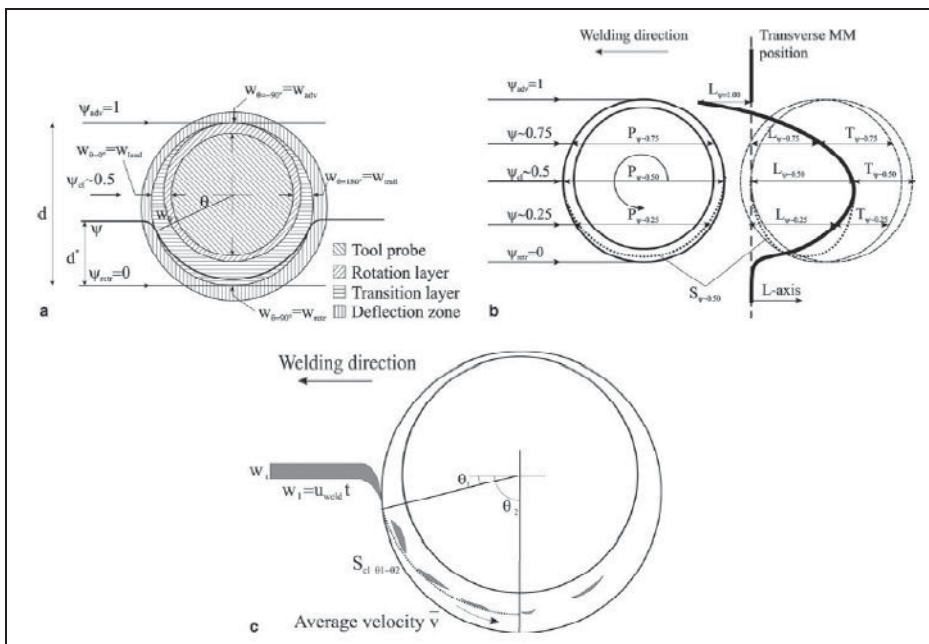
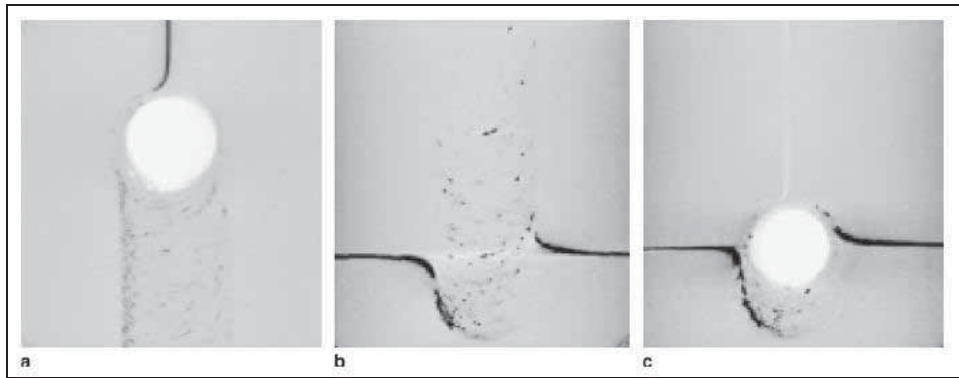


Figure 8. A schematic presentation of the different flow zones in the model by Schmidt et al. (2006).



**Figure 9. Computer tomography images of horizontal sections of AA2024-T3 joints with copper strips as marker material (Schmidt et al. 2006).**

Several studies have divided the material flow into two components: shoulder-driven and probe-driven flows. Shoulder-driven flow is dominant just below the surface of the base material, under the shoulder. The shoulder provides frictional heating and constrains the plasticized base material. The probe-driven flow occurs deeper in the base material, around the tool probe. The rotating probe induces heating by plastic deformation. The two flow components merge and form a defect-free FSW weld. (Kumar and Kailas 2008; Chen and Maginnes 2004; Heurtier et al. 2006; De Vuyst et al. 2006; Dong et al. 1999; Guerra et al. 2003)

### 2.1.3 Welding Parameters

There is a consensus that the most important welding parameter is the rotation speed, but that the traverse speed and plunge depth are also very significant. Rotation speed determines the heat input and temperature as well as the shear experienced by the FSW welds. Consequently, it influences the microstructure and mechanical properties of the FSW welds. Other welding parameters include tilt angle, spindle power, torque, Z force, as well as the distance between the FSW weld and the side of the plate. (Record et al. 2004; Dawes and Thomas 1999; Nandan et al. 2008; Mishra and Ma 2005; Gould et al. 1998; Surekha and Els-Botes 2011; Yan et al. 2004; Cederqvist 2011; Cederqvist 2006; Fehrenbacher et al. 2011; Ahmed et al. 2008; Dubourg et al. 2006)

Many factors affect the process of FSW. Colligan and Mishra (2008) developed a conceptual model of the influence of different welding parameters on the FSW process.

Figure 10 shows the model of the relationships between different welding parameters and their effects.

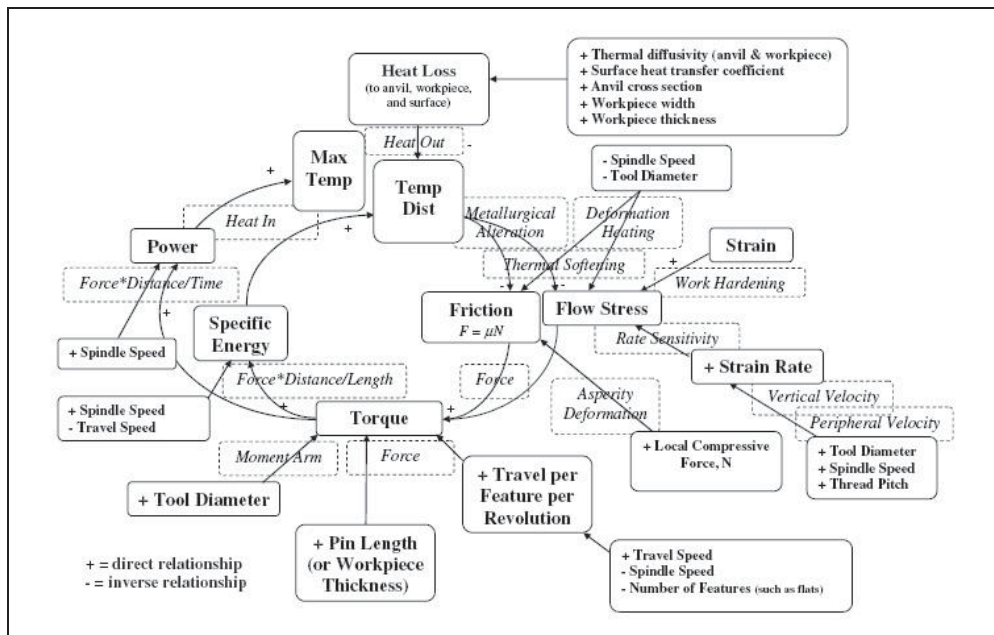


Figure 10. Conceptual model of the relationships between welding parameters and their effects (Colligan and Mishra 2008).

An example of the formation of a FSW welding parameter window in Cu-OF can be seen in Table 1. It shows the effect of rotation and traverse speeds on the formation of welding defects in the welds. Around the area where defect-free welds are formed, the amount and severity of welding defects grows as a function of the deviation from the values of the welding parameter window. (Savolainen et al. 2004)

**Table 1. Example of a FSW welding parameter window for Cu-OF showing the influence of rotation and traverse speeds on welding defect formation (Savolainen et al. 2004).**

RPM	Cu-OF				
	1400	Good weld 300	Good weld 600		
1120	Good weld 250	Very small void	Small void 750	Large void 1000	
900	Good weld 200	Good weld 400	Void 600		
710	Small void 150	Small void 300	Surface-breaking void 450	Surface-breaking void 600	Surface-breaking void 750
450	Void 100		Surface-breaking void 300	Surface-breaking void 400	Surface-breaking void 500
355	Large void 50	Large void 100	Large void 150	Surface-breaking void 200	Surface-breaking void 250

The FSW process can be efficiently controlled by maintaining a constant welding temperature (about 850 °C for copper). Temperature control is based on changing the input values, mainly tool rotation speed. Temperature control by tool rotation speed is much more sensitive than that by traverse speed or axial force. (Cederqvist and Andrews 2003; Cederqvist 2006; Fehrenbacher et al. 2011)

Generally, there is little need for joint preparation, oxide removal, or the use of shielding gas (Dawes 1995; Threadgill and Nunn 2003). In critical applications, when the amount of entrapped oxide particles needs to be minimized, shielding gas during FSW or oxide removal prior to welding can be used. However, oxide removal from the butting faces prior to welding is harmful, unless shielding gas is used during welding. Removal of the protective oxide layer leads to increased oxidation of the butting faces and increased amount of entrapped oxide particles. Additionally, the use of shielding gas makes the process more stable with fewer variations in power input and torque (Cederqvist 2011). (Savolainen et al. 2008)

## 2.2 Tool

The tool is the most significant factor in FSW along with the correct welding parameters. The functions of the tool include heating and softening the base material, dispersing the

oxide layer, extruding the base material from front of the tool to the back and from the top of the weld to the bottom, and finally consolidating the softened material to form a solid phase joint. The tool plays a critical role in the material flow. (Threadgill and Nunn 2003; Mishra and Ma 2005; Nandan et al. 2008)

### 2.2.1 Tool Geometry

The tool consists of a shoulder and a probe. The length of the probe is relative to the thickness of the material to be welded (Dawes 1995). Generally both the shoulder and the probe have features (threads, flutes, flats, scrolls, etc.) to improve the welding action. In thin section welds the effect of the shoulder is more important, but as the section thickness grows, the effect of the probe becomes more dominant. Savolainen et al. (2004) noticed that for FSW of thin section copper a triflat shape is adequate. Thicker sections require more complex tool geometries. (Shercliff and Colegrove 2002; Threadgill and Nunn 2003; Andersson and Andrews 1999; Dawes and Thomas 1999)

Tool geometry is very important as it influences the resulting microstructure and size of the weld and the dispersion of oxides. Tool geometry also contributes to the strength of the tool. A successful tool geometry produces welds with no defects, no surface undercutting, and no flash. In addition, the geometry should be easily machinable. Unfortunately, tool designs are currently based on observations and limited experimental data, not on the understanding of the fundamental process principles. (Dawes 1995; Nelson 2005)

As the welding speed or section thickness grows, the need for more complicated tool geometries increases. One innovative development has been a tool geometry where the shoulder is convex and scrolled, which both constrains the welding material and compensates for plate thickness variations. Tapered shoulder tool and convex scrolled shoulder step spiral (CS4) tool also facilitate welding perpendicular to the material surface, so that there is little thinning and flash. (Colligan and Pickens 2005; Sorenson et al. 2007)

Figure 11 shows the tool design currently used by SKB for FSW of 50 mm thick copper to be applied for manufacturing spent nuclear fuel canisters. The tool probe is a complex MX Triflute variant and the shoulder has a CS4 design. (Cederqvist 2011; Cederqvist 2006)



**Figure 11. The tool currently used by SKB for FSW of 50 mm thick Cu-OFP to be applied for manufacturing spent nuclear fuel canisters. The tool has a probe with a complex triflute design and a CS4 shoulder. (Cederqvist 2011)**

### 2.2.2 Tool Material

The tool material is ideally non-consumable in order to maintain the tool features and to avoid contamination of the weld with tool trace material. With increasing welding temperature the requirements for the tool material become more challenging. Temperature during FSW of copper varies between 790-910 °C. Welding cycle lasts 45 minutes for the 50 mm thick copper canisters for spent nuclear fuel. (Cederqvist 2006, Cederqvist 2011)

Required properties for tool materials include sufficient strength at welding temperature, wear and creep resistance, fracture toughness at ambient and welding temperatures, inertness to the material to be welded, thermal stability, and good friction compatibility with the base material. The essential and desired properties are summarized in Table 2. (Threadgill and Nunn 2003; Gould et al. 1998; Colegrove et al. 2003)

**Table 2. Essential and desirable properties of tool material at welding temperature (Threadgill 2003).**

<b>Essential Properties</b>	<b>Desirable Properties</b>
<b>Sufficient high temperature strength</b>	<b>Oxidation resistance</b>
<b>Wear resistance at ambient and operating temperatures</b>	<b>Established material</b>
<b>Fracture toughness at ambient and operating temperature</b>	<b>Inert to workpiece</b>
<b>Good creep performance</b>	<b>Low toxicity</b>
<b>Machinability</b>	<b>Affordability</b>
<b>Stable microstructure at operating temperature</b>	<b>Multiple Suppliers</b>
<b>Inert to workpiece at operating temperature</b>	<b>Short lead times</b>
<b>Microstructural uniformity</b>	

At the moment wrought nickel-based superalloys are the most promising tool materials for FSW of copper. The tool currently used by SKB for FSW of 50 mm thick copper is made of a Nimonic 105 probe and a Densimet (sintered tungsten alloy) shoulder (Figure 11). The tool probe is coated with chromium nitride using PVD (physical vapour deposition) in order to reduce crack formation (Cederqvist 2011). Inconel 738LC and Inconel 939 were used successfully by Savolainen et al. (2004). Hautala (2001) used Inconel 718 with limited success. Polycrystalline cubic boron nitride (PCBN) is also promising, but there are problems associated with brittleness and size constraints (probe length of only 12 mm is achievable at the moment). Other, less successful tool materials include cemented carbides, ceramics, refractory metals, cast superalloys, and oxide dispersion strengthened (ODS) alloys. (Cederqvist and Andrews 2003)

### **2.3 Microstructure of the Welds**

The microstructure of copper FSW welds is very complicated. It has been studied using many different methods in a variety of copper grades and plate thicknesses. Zones, grain structure and size, texture, and precipitates are discussed.

### 2.3.1 Zones of FSW Welds

The typical transverse microstructure of a FSW weld is comprised of four zones. The nugget, often referred to as the dynamically recrystallized zone, is in the centre. The restoration mechanism depends on the base material. The nugget has undergone the most severe plastic deformation and the highest temperature. The nugget is surrounded by the thermo-mechanically affected zone (TMAZ). In TMAZ, strain and temperature are lower, resulting only in partial recrystallization. TMAZ is followed by the heat affected zone (HAZ), where the base material property changes are due to the heating caused by FSW. Beyond this lies the unaffected base material. The microstructure is formed by the extrusion-like deformation process as well as the rotation of the tool. Subsequent static changes (such as grain growth) take place in the weld. The different zones of the microstructure correlate with the distribution of equivalent plastic strain. Figure 12 shows a schematic presentation of the zones and Figure 13 shows them in a 50 mm thick copper FSW weld. (Shercliff and Colegrove 2002; Källgren 2010; Zhang et al. 2007; Seidel and Reynolds 2001)

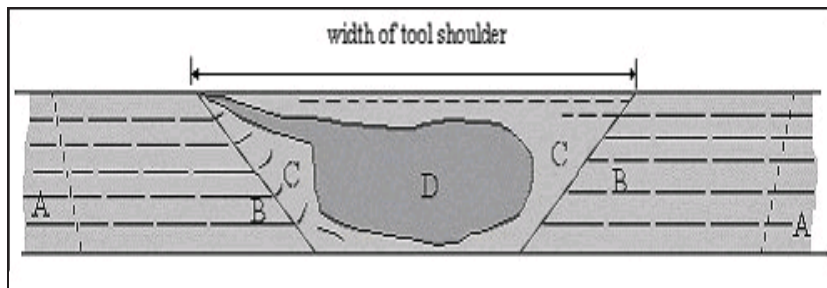


**Figure 12. A schematic presentation of the typical transverse microstructure of a friction stir weld or processed zone illustrating the different zones: unaffected material (A), thermally affected (B), thermo-mechanically affected (C), and dynamically recrystallised material (D). Advancing side is on the left and retreating side on the right. (Kallee and Nicholas 1998)**

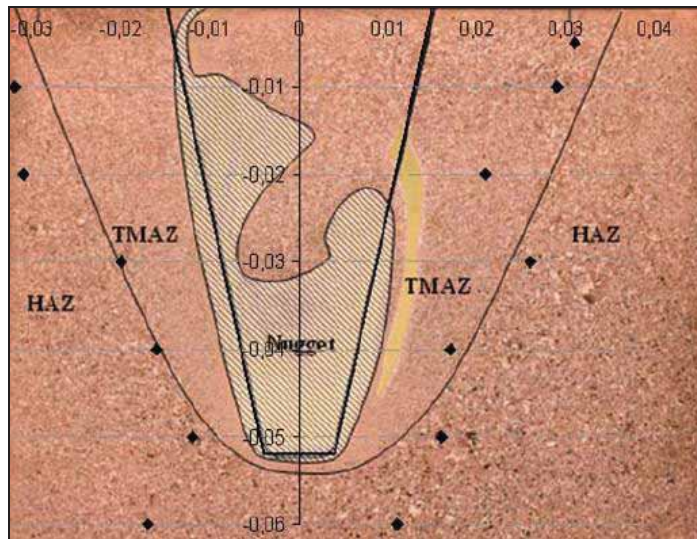


**Figure 13.** Different microstructural zones in a 50 mm thick copper FSW weld (Källgren 2010).

When the 50 mm thick Cu-OFP FSW welds are electrolytically polished, three “processing lines” are revealed. Their location is shown in Figure 14.

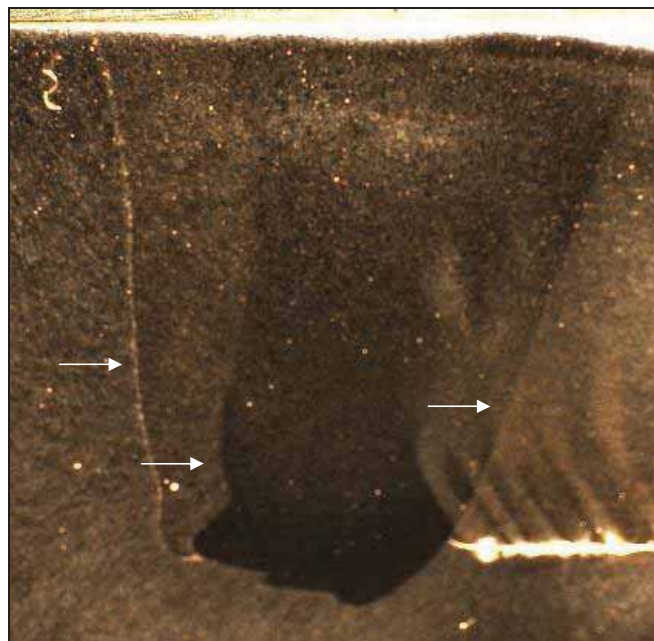


**Figure 14.** The location of processing lines is indicated by arrows in a hydrogen annealed 50 mm thick Cu-OFP FSW weld. The processing line on the left also contains entrapped oxide particles.

### 2.3.2 Grain Size

In copper FSW welds the grain size depends on the strain rate and temperature causing dynamic recrystallization during FSW. Lower heat input either by decreasing the tool rotation speed or by increasing the traverse speed results in smaller grain size. It has also been noticed that grain growth occurs in the wake of the tool. (Xie et al. 2007; Su et al. 2011; Surekha and Els-Botes 2011; Çam 2011; Belyakov et al. 1998)

The grain size of the FSW welds influences their mechanical properties. Although the grain size may be smaller in the nugget, the hardness and strength of the weld may be lower there due to the loss of work-hardening (i.e. reduction in dislocation density). However, a good compatibility between the grain size and mechanical properties can be achieved with Hall-Petch relationship if the subgrain size is used as the main strengthening contribution. (Dalla Torre et al. 2007; Çam 2011)

## 2.4 Banding

Banding is a feature in the nugget of friction stir welds. It is a repeating pattern, the shape of which depends on the base material, tool geometry and welding parameters. In aluminium alloy FSW welds banding appears as cyclic variations in grain size, particle distribution, texture, and/or hardness. (Reynolds 2008; Yang et al. 2004; Sutton et al. 2003; Fonda et al. 2004; Zettler et al. 2006; Booth et al. 2007; Fonda and Bingert 2007)

Banding consists of periodic bands which, in horizontal cross-section, are thicker in the centre and thinner on the edges due to the forward motion of the tool. Figure 15 shows a horizontal cross-section of an aluminium FSW weld. Band spacing corresponds to the feed per revolution as well as to the tool geometry (features such as flutes and flats). The microstructure is more homogeneous and, consequently, the band contrast is lower in slow (“hotter”) FSW welds than in medium and fast (“colder”) welds. (Fonda et al. 2004; Ahmed et al. 2008; Yang et al. 2004; Cui et al. 2008; De Vuyst et al. 2006; Krishnan 2002; Xu and Deng 2008; Li et al. 1999)

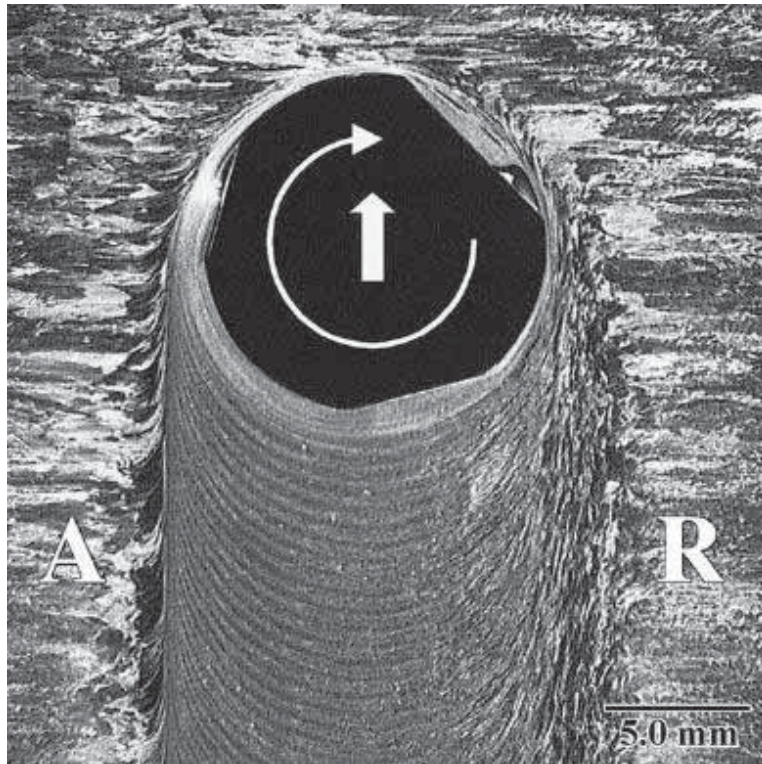


**Figure 15. Horizontal cross-section of an aluminium FSW weld. Advancing (A) and retreating (R) sides of the weld as well as the rotation and traverse directions are marked. (Fonda et al. 2004)**

On the advancing side of the weld the bands are very sharp and well defined but on the retreating side they are more diffuse/obscured (Fonda et al. 2004; Ahmed et al. 2008). The constituent particle size is larger on the advancing side and smaller on the retreating side of the weld. Volume fraction of the particles is also higher on the retreating side. This may be due to the considerably higher estimated strains on the advancing side as compared to the retreating side, leading to more pronounced refinement of particles on the advancing side of the weld. (Fonda et al. 2004; Yang et al. 2004; Sutton et al. 2003; Cui et al. 2008; Zhang et al. 2006)

Chen and Cui (2007) studied the formation mechanisms of banding. They caused the tool probe to break suddenly and analysed the material around the probe. They noticed that the bands are formed as the material is forged and spread by the tool flanks. Each thread space is geometrically restricted (consisting of upper and lower flanks, crests of the thread, and

root) and produces one layer of banded material in the nugget in one rotation of the tool. Also Krishnan (2002) concluded that in FSW a semicylindrical layer of material is extruded by the tool in one rotation of the tool, resulting in the formation of banding. Figure 16 shows the formation of the weld and the banded structure as a result of the geometrically restricted deposition of the material in a layered manner.

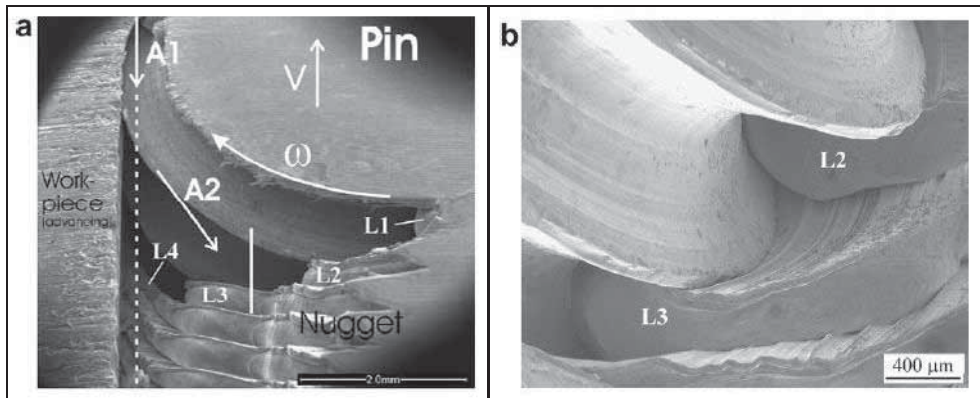


**Figure 16. Formation of banding as a result of the geometrically restricted depositing of material in a layered manner (Chen and Cui 2007).**

In aluminium alloy FSW welds the formation of banding depends on the tool rotation speed as seen in a schematic diagram in Figure 17. Low rotation speeds lead to a zigzag pattern and banding is only formed at higher rotation speeds. Banding forms as material from the retreating and advancing sides with different histories are layered and mixed. (Xu and Deng 2008; Hamilton et al. 2008; Guerra et al. 2003)

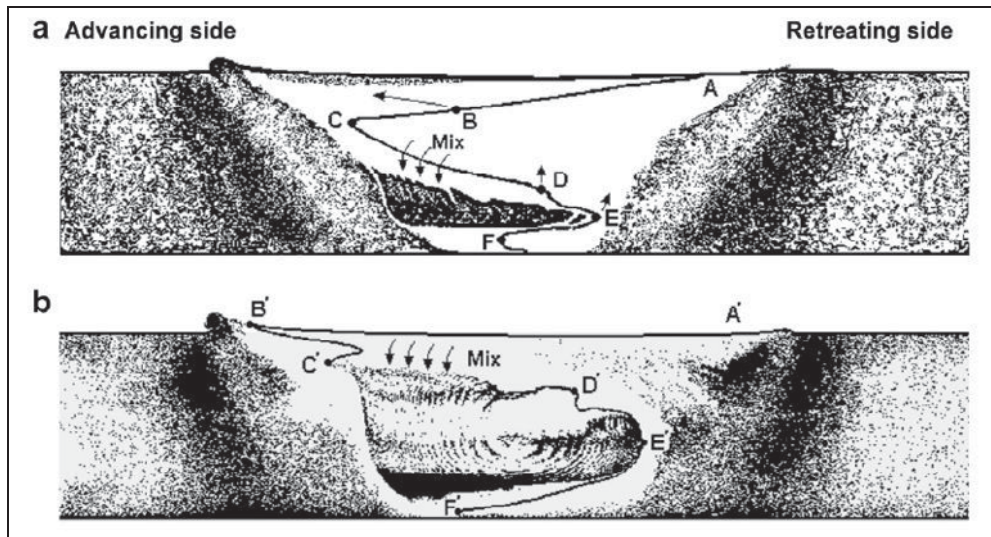


**Figure 17.** A schematic presentation of the effect of tool rotation speed on the formation of banding in aluminium alloy FSW welds. A transverse cross-section of a weld produced by low rotation speed shows a slightly deformed weld interface (a) while at high tool rotation speed the interface is highly deformed and banding appears (b). (Xu and Deng 2008)

In aluminium alloy FSW welds the complex thermal and deformation histories greatly affect the resulting microstructure. Slight variations in the original crystallographic orientations of the base material have also an effect on the microstructure, as they react differently to the shear deformation during FSW. (Fonda and Bingert 2007; Ahmed et al. 2008)

According to Prangnell and Heason (2005), the orientation differences in aluminium alloy FSW welds are due to rigid body rotations between adjacent bands caused by irregularities in the material flow, whereas Fonda and Bingert (2007) state that the orientation differences are caused by periodically changing deformation conditions (variations in strain rate or temperature) resulting in texture variations between the bands. Also Chen and Cui (2007) concluded that microstructural variations in the bands (e.g. variations in grain size, particle distribution, or texture) are due to shear deformation variations within the layers.

Reynolds (2008) noticed a cyclic fluctuation in torque and X-force corresponding to the banding in aluminium alloy FSW welds. Both he and Schneider et al. (2006) suggest that

the material flow is affected by the contact conditions (stick-slip) between the tool and base material, thus varying the strain rate.

## **2.5 Copper as Base Material in FSW**

FSW of copper is more difficult as compared to FSW of aluminium as copper has significantly higher melting point, thermal conductivity, and flow stress. According to Mahoney (2003), the flow stress at welding temperature determines the friction stir weldability of a given material. Restoration process influences the resulting microstructure and mechanical properties. Källgren and Sandström (2003) state that in FSW of copper the main restoration process is recrystallization, which is visible in the nugget (completely recrystallised) and also in the TMAZ (partially recrystallised). Dynamic recrystallization (DRX) lowers the flow stress during deformation at elevated temperatures. There are also some other factors that are considered to influence the friction stir weldability of a material. Heat transfer characteristics (such as thermal conductivity, heat capacity, and thermal diffusivity) of the base material largely define the required process conditions for welding. For example, low thermal diffusivity reduces the heat transfer rate, which can be compensated with lower tool rotation and higher traverse speeds and a larger tool shoulder diameter. Melting temperature of the base material gives an indication of the operating temperatures and stresses of the tool. Effective plastic range is the range of temperatures over which the weldable material can achieve a plastic state. A wide plastic range of the weld material results in a wide range of processing conditions. (Gould et al. 1998)

### **2.5.1 Properties of Copper**

Copper has a face-centred cubic (fcc) crystal structure and it does not undergo phase changes after solidification. Melting point of copper is 1084 °C. Copper has a significantly lower stacking fault energy (SFE, 78 mJ/ m<sup>2</sup>) as compared to that of aluminium, affecting the restoration process. Other properties of copper include high thermal and electrical conductivity, formability, and corrosion resistance. (McNalley et al. 2007)

## 2.5.2 Flow Stress

Mahoney (2003) concluded that flow stress at the welding temperature determines the ability of a metal to be friction stir welded. Flow stress is the average of the yield and tensile stresses of the material. Gao et al. (1999) tested copper with 99.99 and 99.9999 mass percent purities (4NCu and 7NCu, respectively). It was noticed that increasing the temperature or decreasing the strain rate lowers the flow stress, as seen in Figure 18. The increasing amount of impurities has also a large increasing influence on the flow stress. DRX is indicated by softening and steady state after a peak stress on the flow curves of the material. The same flow stress can be obtained with various combinations of temperature and strain rate. The combined influence of temperature and strain rate can be defined with the Zener-Hollomon parameter ( $Z$ ), shown in the following equation:

$$Z = \dot{\epsilon} \exp(Q/RT), \quad (1)$$

where  $\dot{\epsilon}$  is the strain rate,  $T$  is the absolute temperature,  $R$  is the gas constant, and  $Q$  is the activation energy for deformation. The apparent activation energy for hot deformation of copper in the high temperature (700-950 °C) and high strain rate (3-100 s<sup>-1</sup>) region suggests that the rate-controlling mechanism is grain boundary self-diffusion. (Prasad and Rao 2004)

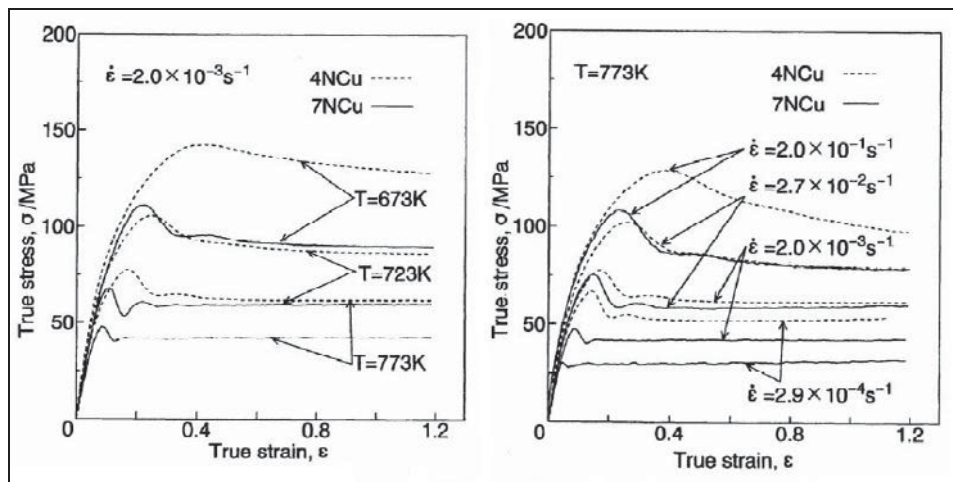


**Figure 18.** The influence of temperature (left) and strain rate (right) on the flow stress of copper with different purity grades (Gao et al. 1999).

### 2.5.3 Dynamic Recrystallization

Dynamic recrystallization is a restoration process which occurs during high-temperature metal working operations, for example hot rolling, forging, and extrusion. Many researchers (e.g. Källgren and Sandström 2003) have reported on dynamic recrystallization occurring during friction stir welding of copper, especially in the weld nugget. It is consistent with the observations of Shercliff and Colegrove (2002), who report that some aspects of FSW can be compared to extrusion and forging. Dynamic recrystallization is beneficial as it lowers the flow stress of the material and enables the material to be more easily deformed. It also influences the texture and grain size of the worked material, thus affecting its properties. (Humphreys and Hatherly 1995)

DRX is dependent on temperature, strain, stress, and the initial microstructure. Impurities increase the temperature of recrystallization. DRX is a continuous process of deformation, nucleation of grains, and subsequent migration of grain boundaries leaving new dislocation-free grains, which then deform further. The driving force for DRX arises from the elimination of dislocations generated during deformation. In metals with low or medium stacking fault energy (SFE), such as copper and its alloys, in which restoration processes are slow, DRX may take place when a critical deformation condition is reached (dislocation density increases to a critical value necessary for DRX to occur). Figure 19 shows a schematic of the typical characteristics of DRX with changes in the deformation conditions, including stress-strain response, grain size evolution, and stress dependence on grain size. Grain size in DRX is only dependent on the processing conditions, not on the initial grain size. (Humphreys and Hatherly 1995; Cram et al. 2009)

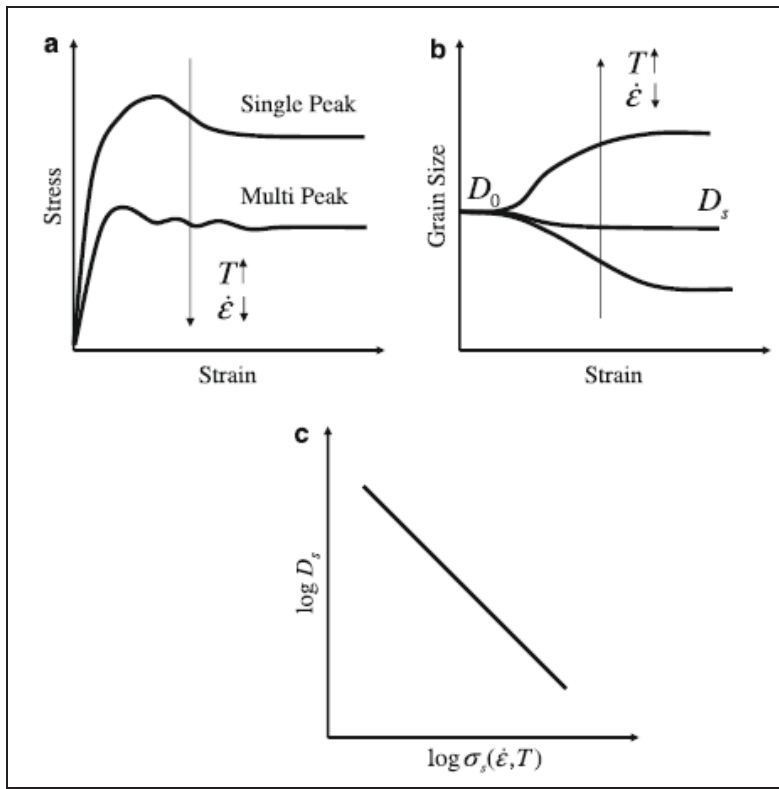


**Figure 19. Schematic illustration of the typical characteristics for DRX with changes in deformation conditions. a) Stress-strain curves with transition from single-peak to multi-peak behavior. b) Evolution of the grain size from the initial  $D_0$  to the steady-state  $D_s$  grain size. c) Dependence of stress on the grain size. (Cram et al. 2009)**

A simplified description of DRX is as follows. During high-temperature deformation new grains originate at the high-angle boundaries (misorientation greater than 10-15°, generally old grain boundaries). As the material deformation continues, the dislocation density of the new grains increases and reduces the driving force for their growth. Finally the recrystallized grains cease to grow and a new grain structure is formed. Figure 20 shows the development of microstructure during dynamic recrystallization. DRX generally starts at the old grain boundaries (Figure 20a). New grains are nucleated at the boundaries of the growing grains (Figure 20b) and in this way a thickening band of recrystallized grains is formed (Figure 20c). Eventually the material will become fully recrystallized (Figure 20d). (Humphreys and Hatherly 1995; Doherty et al. 1997)

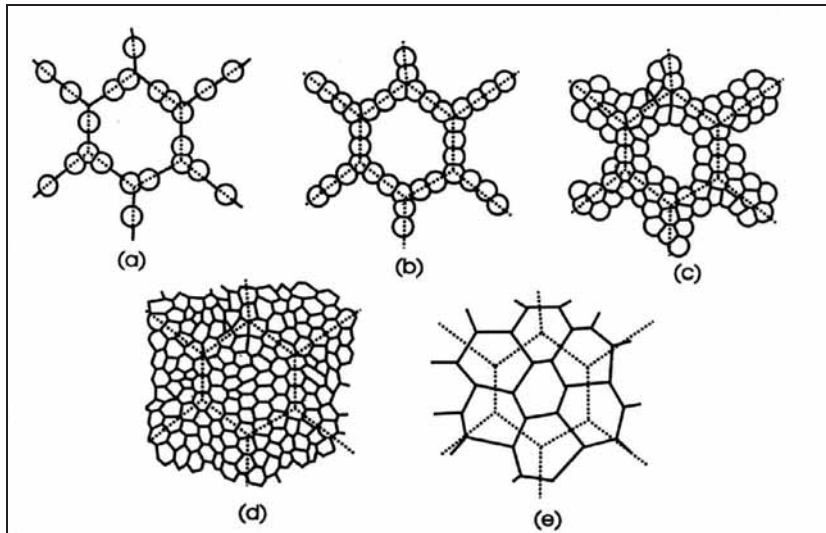


Figure 20. The development of microstructure during dynamic recrystallization. In (a-d) with large initial grain size and (e) with small initial grain size. (Humphreys and Hatherly 1995)

### 3 FRICTION STIR PROCESSING

Friction stir processing (FSP) is the most important variant of FSW. The process and tools are similar, but instead of creating a joint as in FSW, the aim of FSP is to locally alter the microstructure of the base material to obtain desirable properties. By FSP, materials can be processed selectively at specific locations, without changing the properties of the entire structure. It can be used to tailor the microstructure of materials to be suitable for various applications, affecting either only the surface of the material or through-thickness sections. It creates a gradual transition from the processed material to the unaffected base material. FSP produces a homogeneous microstructure with a fine grain size and a uniform second phase particle distribution. FSP can be used, for example, to improve strength, ductility, resistance to corrosion and fatigue, as well as to enhance thick section formability, eliminate casting defects, produce surface composites, and create high strain rate superplasticity (Figure 21). A review of the state-of-the-art of FSP was made by Savolainen et al. (2006), including the principle, tools, applications, and materials. (Fuller et al. 2003; Mahoney et al. 2001a; Mahoney et al. on-line; Mahoney and Lynch on-line; Mishra et al. 2003; Ma et al. 2004)

FSP has been used in many applications for aluminium alloys. It has been applied to the enhancement of fatigue life by microstructural refinement and homogenization as well as to the elimination of casting defects, production of high strength (650 MPa) and good ductility in cryomilled nanophase aluminium alloys, to the improvement of tensile properties of fusion welded dissimilar aluminium alloys by eliminating porosity and refining the microstructure, to the creation of high strain rate superplasticity, and to the production of ultra-fine grained aluminium with excellent mechanical properties. (Sharma et al. 2004; Berbon et al. 2001; Fuller et al. 2004; Charit and Mishra 2003; Kwon et al. 2003)

In addition to aluminium alloys, FSP has been applied to many other materials. Lee et al. (2008) reported in-situ production of aluminium-iron nanocomposites with enhanced modulus and tensile strength. FSP was used to harden the surface of cast iron by forming extremely fine martensite with the resulting microstructure possessing average hardness of 700 HV (Fujii et al. 2008). The effects of arc welding in 304L stainless steel were

diminished by FSP which lowered the residual stresses and eliminated the cast microstructure as well as defects such as cracking and porosity (Sterling et al. on-line). FSP eliminated casting defects of Ni-based superalloy Inconel 718 while producing homogeneous microstructure and fine grain size as well as yielding the fracture toughness and microhardness values above those of the base material (Jasthi et al. 2011).

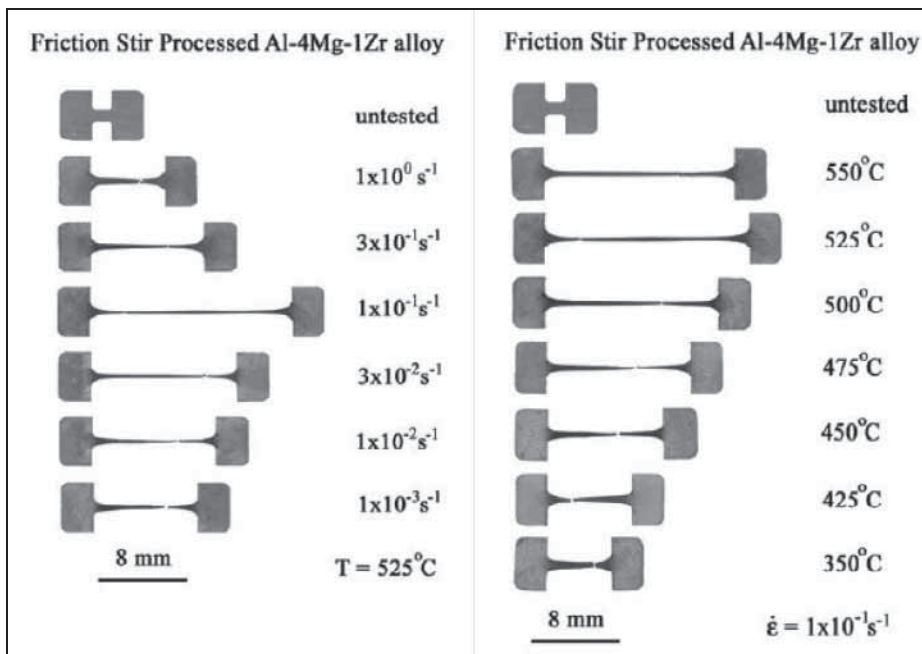


**Figure 21. Al-4Mg-1Zr specimens produced by FSP before and after superplastic deformation. a) At  $525^{\circ}\text{C}$  and different strain rates and b) at  $2 \times 10^{-1} \text{ s}^{-1}$  and different temperatures. (Ma et al. 2003)**

### 3.1 Process

In FSP, the material modification mechanisms are the same as in FSW. The tool is traversed until the entire area to be processed has been covered. The passes are overlapping, the tool probe typically being moved by  $\frac{1}{2}$  probe diameter to the advancing side of the previous pass. Posada (2006) reported the use of a spiral raster in moving the tool in order to eliminate the advancing side and the defects associated with it. Figure 22 shows a schematic presentation of FSP. (Dawes 1995; Mahoney and Lynch on-line; Fuller et al. 2003)

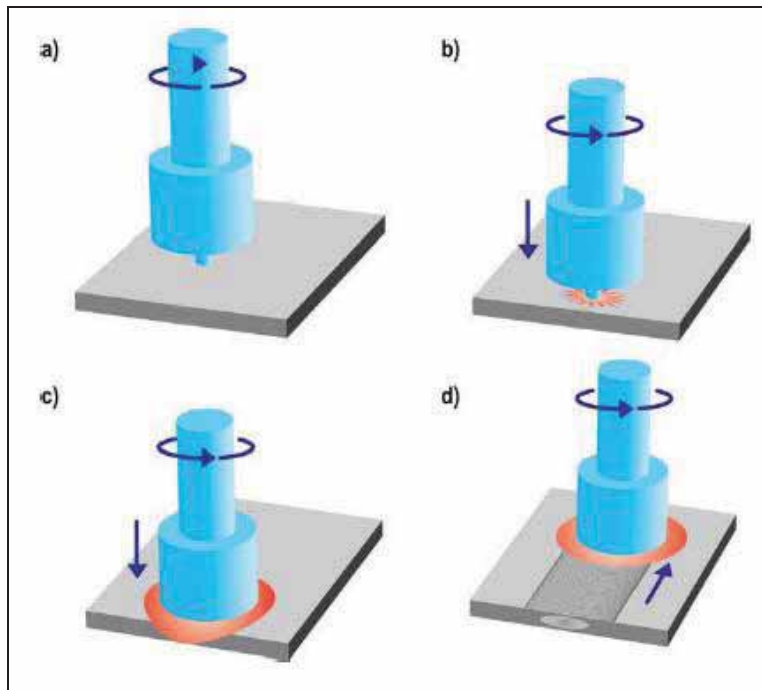


**Figure 22. A schematic presentation of FSP. A rotating tool is plunged into a work piece. Friction heats and plasticizes the base material and as the tool is traversed, a processed zone is created. (Mahoney and Lynch on-line).**

### 3.2 Tool

The geometry of the FSP tool depends on the application. The tool shoulder and length of the probe control the thickness of the processed zone. When processing thicker sections, the geometry can be the same as in FSW, with a shoulder and a probe. When only the surface needs to be processed, a tool without a probe can be used. Figure 23 shows a probeless FSP tool, which is effectively just a scrolled shoulder. A scrolled shoulder was noticed to reduce the amount of flash as well as to produce a greater FSP depth. (Shercliff and Colegrove 2002; Dawes and Thomas 1999; Fuller et al. 2004; Dawes 1995; Mahoney et al. 2001a)

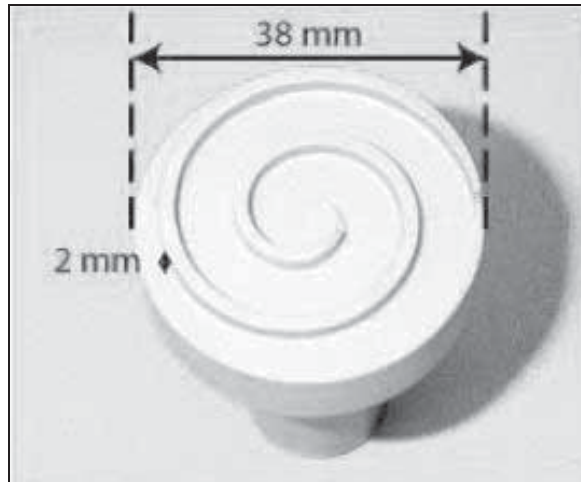


**Figure 23.** A probeless FSP tool with a 38 mm diameter scrolled shoulder and a 2 mm deep web (Fuller et al. 2004).

### 3.3 FSP of Copper

FSP is used to improve the mechanical properties of pure copper. The mechanical properties of the processed material as compared to those of the base material depend on the condition of the base material (annealed or work-hardened) as well as on the heat input during FSP. When compared to annealed base material, FSP increases hardness as well as yield and ultimate tensile strength values with little effect on elongation to fracture. FSP of work hardened material lowers hardness as well as yield and ultimate tensile strength values and it also significantly improves the elongation to fracture. Lower heat input during FSP (achieved by increasing traverse speed and/or decreasing rotation speed) leads to smaller grain size, higher hardness as well as yield and ultimate tensile strength values, and lower elongation to fracture. It was also noticed that FSP does not impair the electrical conductivity of copper despite the smaller grain size. (Surekha and Els-Botes 2011; Barmouz et al. 2011a; Barmouz et al. 2011b)

Su et al. (2011) produced nanocrystalline structures in oxygen-free high conductivity copper (Cu-OFHC) by FSP in a single step. They used small tools and rapid cooling with dry ice in order to minimize the heat input. The resulting microstructure had equiaxed grains with the grain size varying from 50-300 nm (174 nm in average) and nearly random orientation.

## 4 DISSIMILAR METAL WELDING

FSW offers interesting possibilities for the joining of dissimilar materials due to the solid state nature of the method. Metals with different melting points or materials which cannot be welded using fusion welding methods can be joined using FSW. Dissimilar material welds between, for example, different aluminium alloys (marine and aerospace industry), aluminium and steel (automotive industry), aluminium and titanium (aviation industry), as well as aluminium and magnesium (automotive industry) are possible. (Tanaka et al. 2009; Lee et al. 2006; Watanabe et al. 2006; Okamura and Aota 2004; Cavaliere et al. 2009; Choi et al. 2011; Karlsson et al. 2000; Dressler et al. 2009).

Copper and aluminium are widely used in the electric power industry. However, it is difficult to join them using fusion welding methods due to their large differences in physical and chemical properties and the tendency to form brittle intermetallic compounds (IMC). FSW of Cu/Al dissimilar metal joints is discussed in more detail in the following. (Xue et al. 2011a; Braunović and Alexandrov 1994; Elrefaey et al. 2005)

### 4.1 FSW of Dissimilar Materials

The arrangement of the base materials in regard to FSW is important. Generally, the lower strength material should be on the retreating side in order to prevent it from being displaced from the weld as flash and from causing large voids and poor surface quality. If the base materials have similar properties (such as Al/Al or Al/Mg), the arrangement is not so critical. (Okamura and Aota 2004; Xue et al. 2011a; Cavaliere et al. 2009; Karlsson et al. 2000; Uzun et al. 2005; Watanabe et al. 2006)

Another important aspect in FSW of dissimilar metals is the location of the probe in relation to the joint line. Displacement of the probe from the centre line has been proven to be beneficial. Okamura and Aota (2004), Xue et al. (2010; 2011a; 2011b), Watanabe et al. (2006), and Uzun et al. (2005) offset the probe significantly to the side of the softer material, barely touching the harder material. According to them, it makes the joining of materials with different properties feasible. The temperature is lower as compared to welding at the centre of the joint line, leading to the formation of a smaller amount of

brittle IMC layers, but also less mixing of the base materials. In the study by Savolainen et al. (2005), the probe offset was slightly on the copper side, as the tool geometry was initially designed for making copper welds. Good quality dissimilar metal welds were produced also with this configuration.

IMC structures are found in FSW welds of dissimilar materials (Cu/Al, Al/Mg, Al/Ti, etc.). They were also discovered by Savolainen et al. (2005) between copper and aluminium. The thickness of the IMC layers increases with increasing tool rotation speed and decreasing tool traverse speed, corresponding to higher temperatures and longer duration times. The IMC structures have a significant influence on the mechanical properties of the joints. While a thin IMC layer or structure improves the mechanical properties, a thick layer decreases them dramatically. (Choi et al. 2011; Dressler et al. 2009; Ouyang et al. 2006; Xue et al. 2011a; Sarrafi et al. 2011)

## **4.2 Cu/Al Dissimilar Metal FSW**

For Cu/Al dissimilar metal FSW it applies that copper should be on the advancing side in order to produce defect-free welds with good surface quality. Copper with its higher flow stress and melting point is more difficult to transport than aluminium. When copper is on the retreating side, material flow is more difficult which leads to poor weld surface quality, high amount of flash, and weld defects. (Xue et al. 2011a; Okamura and Aota 2004; Avettand-Fènoël et al. 2010; Sarrafi et al. 2011, Savolainen et al. 2004)

Cracks, voids, large copper particles, and poor surface quality were observed at small probe offsets due to the difficult mixing between copper particles and aluminium matrix. At sufficiently large probe offsets (to the aluminium side) the welds exhibited good surface quality and defect-free welds with a fairly uniform mixture of Cu particles in aluminium matrix. Savolainen et al. (2005) produced good quality welds with probe offset to the copper side (Figure 24). They used a tool geometry designed for FSW of copper, whereas in the other studies a tool geometry used for FSW of aluminium has been used. Avettand-Fènoël et al. (2010) also suggest that the tool offset should be to the copper side in order to obtain higher deformability of copper. (Xue et al. 2011a; Okamura and Aota 2004; Sarrafi et al. 2011)

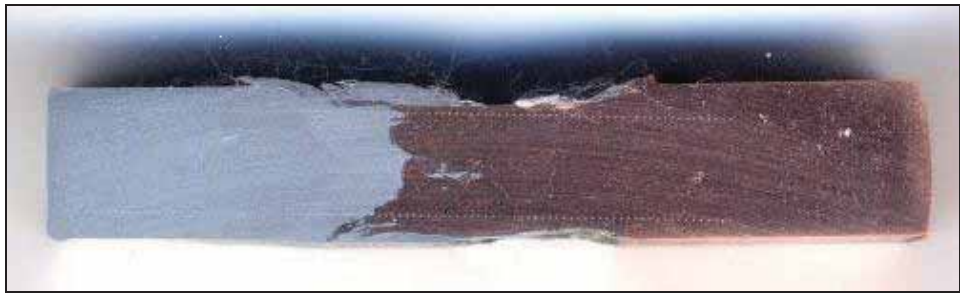


**Figure 24. A transverse cross-section of a double-sided Cu/Al dissimilar metal FSW weld.**

Xue et al. (2011b) studied the influence of welding parameters on FSW of Cu/Al dissimilar metal joints. They noticed that at lower tool rotation speeds voids are formed due to insufficient heat formation. At medium rotation speeds good quality welds with a continuous, thin IMC layers were produced. With too high rotation speeds the layered IMC structures grew too thick, having an adverse effect on the mechanical properties of the welds. The weld surface quality also suffered greatly from the formation of too excessive IMCs.

Generally, the tensile strength of good quality Cu/Al dissimilar metal FSW joints is similar to that of the weaker base material. Tensile strength is lowered by low rotation speeds and/or large probe offsets leading to insufficient mixing of the base materials. Elongation to fracture is often low in Cu/Al dissimilar metal FSW joints due to the formation of brittle IMC layers. Minimizing the brittle layer at the weld interface leads to higher elongation to fracture. (Liu et al. 2008; Xue et al. 2010; Xue et al. 2011a; Okamura and Aota 2004, Savolainen et al. 2005)

Sarrafi et al. (2011) reported that the ultimate tensile strength of Cu/Al dissimilar metal FSW joints was 75 % of that of the cold-worked aluminium base material. Fracture occurred on the aluminium side in the HAZ where FSW had annealed the base material.

Xue et al. (2010) studied Cu/Al dissimilar metal FSW weld interfaces using very small tensile test specimens. The test samples containing the IMC layer fractured at the particle rich zone. Tensile strength was up to 210 MPa, being much higher than that of the weaker

base material (aluminium). They concluded that Orowan strengthening by the IMC particles had strengthened the structure.

Xue et al. (2011a; 2010) studied Cu/Al dissimilar metal FSW joints using three-point bend tests. Samples made at the tool rotation speed of 600 rpm and probe offset of 2 mm exhibited very good results. They could be bent 180° without fracture. At higher tool rotation speeds the bending properties were poor due to the layered IMC structures at the weld interface.

Liu et al. (2008) noticed different structures on the copper and aluminium sides of the nugget. They suggested that they were due to the different thermal conductivities of aluminium and copper, leading to a temperature reduction in the copper side. Continuous dynamic recrystallization (CDRX) was noticed on the Al side with significant grain refinement. They estimated that the material temperature was below 500 °C and that therefore copper did not experience CDRX, only plastic flow. According to them, no obvious metallurgical bonding occurred between copper and aluminium during FSW, resulting in the formation of a weld nugget with a lamellar structure. Contrary to Liu et al. (2008), Avettand-Fènoël et al. (2010) concluded that dynamic recrystallization occurs both in aluminium and copper during FSW of Cu/Al dissimilar metal joints and Belyakov et al. (1998) state that DRX takes place in copper fully or partly at temperatures higher than 250 °C.

Many authors have detected the existence of IMC layers in Cu/Al dissimilar metal FSW welds. According to X-ray diffraction (XRD) analysis, the detected IMCs are  $\text{Al}_2\text{Cu}$ ,  $\text{AlCu}$ , and  $\text{Al}_4\text{Cu}_9$ . The layers are continuous and uniform with thicknesses of about 1  $\mu\text{m}$ . The layers also contained  $\alpha$ -Al and the saturated solid solution of Al in Cu. Only Liu et al. (2008) reported that according to XRD analysis no new IMCs were generated during FSW. Even though the temperature during FSW is lower than the melting points of copper or aluminium, it is sufficiently high to form hyper-eutectic Cu-Al alloys. (Ouyang et al. 2006; Xue et al. 2010; Xue et al. 2011a; Sarrafi et al. 2011; Elrefaey et al. 2005)

Intermetallic compounds between copper and aluminium are hard and brittle due to their non-metallic covalent bonding and they have high electrical resistance which reduces the strength and electrical conductivity with increasing thickness of the IMC layer (Abbasi et

al. 2001). The formation of the different IMCs depends on the annealing time and temperature (Lee et al. 2004). Increasing the welding temperature also increases the amount of IMCs, both at the interface and in the nugget. In FSW the annealing time and temperature depend on the welding parameters (mainly rotation and traverse speeds of the tool). Thickness of the IMC layers increases with increasing temperature and time (Braunović and Alexandrov 1994). It was noticed that a thin foil (50  $\mu\text{m}$ ) of zinc between copper and aluminium decreases the amount of harmful IMCs forming during FSW of lap joints. The average fracture load of the joints with zinc intermediate layer was three times higher as compared to the joints without the zinc layer. According to Xue et al. (2011), a thin layer of IMCs is required at the weld interface to ensure bonding between copper and aluminium. (Elrefaey et al. 2005)

## 5 ENTRAPPED OXIDE PARTICLES

Entrapped oxide particles (also known as kissing bond, joint line remnants, or line-type artefact) have been studied mainly in aluminium FSW welds. Entrapped oxide particles form a line, generally in a zigzag pattern. The line meanders partially or completely through the weld. The line consists of small oxide inclusions (<100 nm) with varying degrees of amount and connectivity. The particles are located at grain boundaries. The amount and connectivity of the particles decreases with increasing distance from the root of the weld due to the more efficient mixing near the shoulder of the tool. (Vugrin et al. 2005; Sato et al. 2004; Palm et al. 2003; Okamura et al. 2002)

The line of entrapped oxide particles is formed by fragmentation and dispersion of the oxide layers of the initial butting surfaces and it is not seen in bead-on-plate welds. The pattern of the entrapped oxide particles depends on the welding parameters, base material, and tool design. As the thickness of the original oxide layer or the alloying element content of the base material increases, the line of entrapped oxide particles becomes more pronounced. Removal of the original oxide layers by pickling, brushing, or milling has the opposite effect. (Palm et al. 2003; Sato et al. 2004; Okamura et al. 2002; Warsinski et al. 2011; Jene et al. 2006)

Although generally considered as harmless, on certain occasions the entrapped oxide particle lines have been noticed to reduce the mechanical strength of the welds. Figure 25 shows the crack path in a tensile tested aluminium alloy along the line of entrapped oxide particles. Root and face of the FSW weld were removed prior to testing. Entrapped oxide particle lines can be occasionally linked with the premature joint failures. SEM studies have shown that different failure modes are active depending on the location of the fracture. Failure at the line of entrapped oxide particles exhibits a less ductile fracture due to the strain localization, while fracture occurs in a highly ductile manner elsewhere in the weld. The line of entrapped oxide particles is also assumed to adversely affect the corrosion properties of the welds. (Jene et al. 2006; Sato et al. 2004; Warsinski et al. 2011; Palm et al. 2003; Okamura et al. 2002)

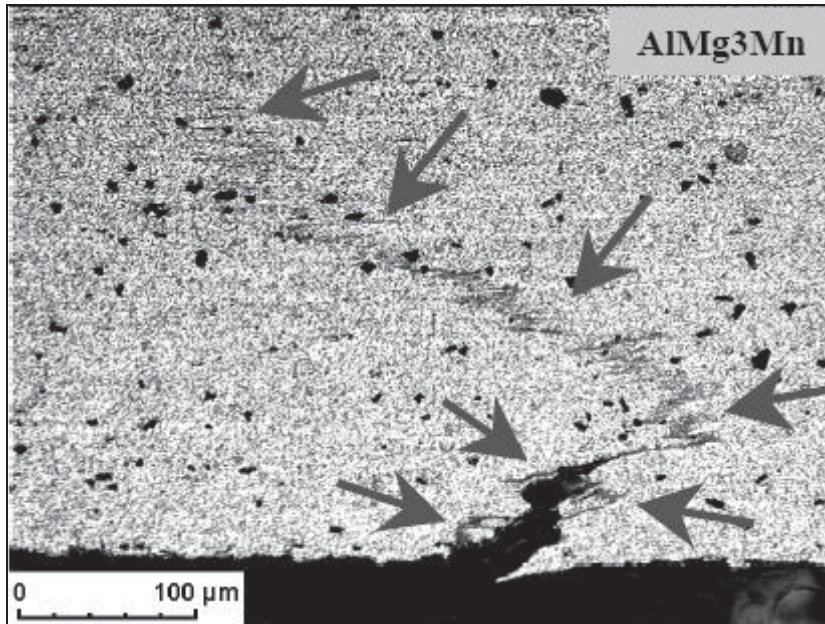


**Figure 25.** Crack path in a tensile tested aluminium alloy FSW weld. The fracture is located at the line of entrapped oxide particles. The root and face of the weld were removed prior to testing. (Jene et al. 2006)

## **6 WELDING DEFECTS**

Welding defects occurring in FSW welds differ from those in fusion welds due to the solid state nature of FSW. This Doctoral Thesis concentrates on defects occurring in copper FSW butt welds in general and on those in copper spent nuclear fuel canisters in particular. The formation of welding defects is discussed and a classification and description of the different defects are given.

### **6.1 Formation of Welding Defects**

When defects begin to form in FSW, they are typically continuous, encompassing the entire remaining length of the joint. Defects are usually located on the advancing side of the joint. The defects can be caused by several incorrect variables, such as tool geometry, traverse and rotation speeds of the tool, plunge depth, and tilt angle. A too wide welding gap as well as plate thickness mismatch and variation can also lead to the formation of welding defects. Different welding variables influence the material flow, which in turn defines the formation of the weld as well as the welding defects. Cederqvist and Andrews (2003) concluded that the major cause for the formation of weld defects in FSW of 50 mm thick copper was process instability. They also noticed that a control system of the welding temperature not only improved weld quality, but also simplified weld production. (Bendzak et al. 2000; Leonard and Lockyer 2003; Zettler et al. 2010; Arbegast 2008)

In their 3D model of FSW, Bendzak et al. (2000) attributed the formation of welding defects to the chaotic transition region of the material flow on the advancing side of the weld. The transition region is between the region of rotation immediately below the shoulder and the region of extrusion near the probe. Colegrove and Shercliff (2005) have also modelled the FSW process and concluded that defects occur on the advancing side of the FSW weld due to a stagnation point. Experimental results by Leonard and Lockyer (2003) have supported the theoretical models.

## 6.2 Welding Defects in Copper FSW Welds

Arbegast (2008) and Zettler et al. (2010) have analyzed and classified the welding defects occurring in aluminium alloy FSW welds, but their results are not directly applicable to copper FSW welds. Figure 26 shows a schematic presentation of the appearance and location of welding defects in copper FSW welds. Flash formation and plate thinning due to the effect of the tilted shoulder are not considered as welding defects in this Doctoral Thesis, but as characteristic features of FSW welds.

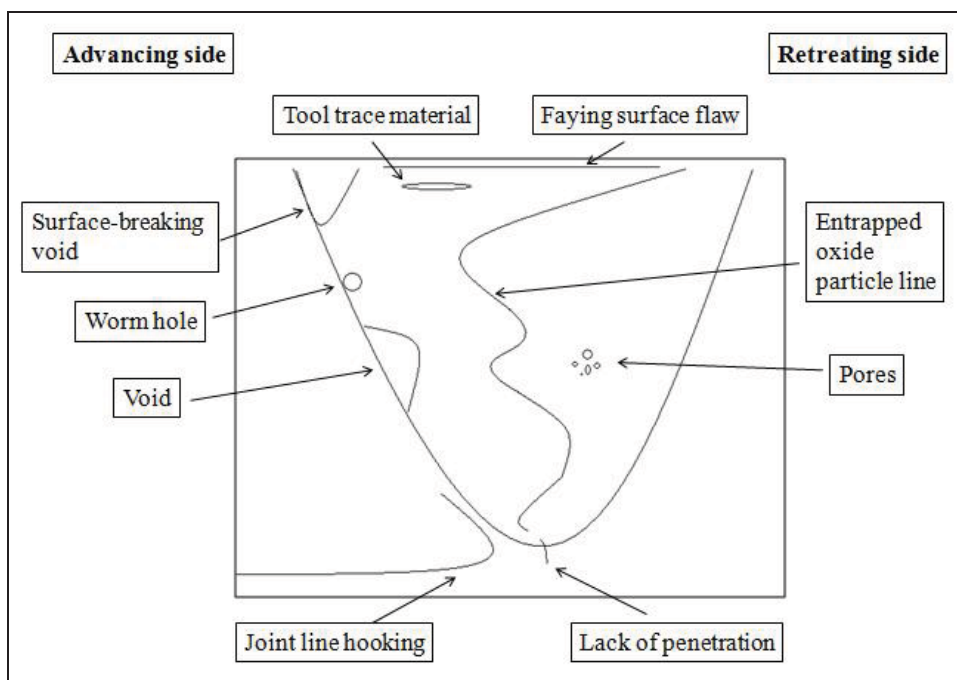


**Figure 26.** A schematic presentation of the location of different welding defects in copper FSW welds.

### 6.2.1 Voids

Voids are volumetric, contain no material, and are aligned with the welding direction. They are generally continuous throughout the entire weld. Figure 27 shows a double-sided weld of Cu-DHP with a void on the advancing sides of the welds. The voids can be located on the advancing side or at the root of the weld depending on the process variables. The size of the voids varies also greatly. Voids indicate that the weld has been too cold. The

temperature has not been sufficient to properly plasticize and deform the material. This is due either to a too high traverse speed, too low rotation speed, or too low plunge depth. Plate thickness variations or too wide welding gaps can also cause the formation of voids. In this work the defects known as “worm holes” are considered as voids. Worm holes are small voids which are aligned through the wall thickness direction instead of along the welding direction. (Leonard and Lockyer 2003; Bird 2003; Fuller 2007; Källgren 2010)

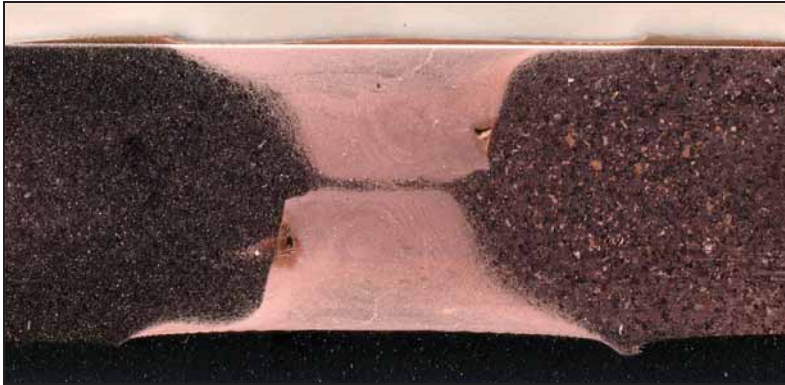


**Figure 27. An example of a double-sided Cu-DHP FSW weld with voids on the advancing sides of the welds.**

There are different opinions related to the definition of a void. In this work voids can be surface-breaking or sub-surface as they are closely related to each other. Figure 28 shows the similarity in the formation of surface-breaking and sub-surface voids. Voids form when the amount of heat and pressure has not been adequate to fill the space behind and below the tool.



**Figure 28. Similarity in the formation of surface-breaking and sub-surface voids in a copper FSW weld.**

Surface-breaking voids are often detected by visual inspection. Dye penetrant and eddy current testing can also be used for their detection. It is possible to detect sub-surface voids using non-destructive testing (NDT) methods, such as radiographic and ultrasonic testing (Bird 2003).

In the upper region of the weld (influenced by the tool shoulder) even surface breaking voids may form. In FSW of 50 mm thick copper, voids up to 10 mm in diameter have been noticed on the advancing side. According to SKB (2005), they are due to insufficient welding temperature, caused in particular by too low tool plunge depth.



**Figure 29. Void in the upper part of a 50 mm thick copper FSW weld (SKB 2005).**

### 6.2.2 Lack of Penetration

Lack of penetration (LOP) leaves the plates at the root of the weld unjoined, though they may have some weak bonding. This type of defect is effectively a crack, which causes the structure to fracture easily due to the high stress concentration factor. It causes a reduction in tensile strength and loss of fatigue strength. The severity of the defect depends on its size. The primary reason for LOP is a too short tool probe. It can be caused also by a too

low plunge depth, plate thickness variation, improper tool design, or tool misalignment in relation to the butting surfaces. It is possible to detect LOP with radiographic, ultrasonic, eddy current, or dye penetrant testing (in through-thickness welds), but no reliable NDT method is available at the moment. The only definitive method is a bend test with the root in tension. In critical applications, the weld root is recommended to be machined. Figure 30 shows a LOP defect in a Cu-DHP weld. (Bird 2003; Leonard and Lockyer 2003; Zettler et al. 2010; Fuller 2007)



**Figure 30. LOP in a Cu-DHP weld.**

### 6.2.3 Entrapped Oxide Particles

Entrapped oxide particle lines are occasionally called “lazy S” or “kissing bond”. They consist of a semi-continuous layer of oxide particles along the joint line. The amount and connectivity of the micron-sized voids is highest at the root of the weld and diminishes towards the top of the weld. Figure 31 shows entrapped oxide particle lines in a Cu-OF weld. (Bird 2003; Vugrin et al. 2005; Fuller 2007)

Entrapped oxide particles are due to insufficient cleaning of the butting surfaces prior to welding or insufficient breaking and mixing of the original oxide layers on the butting faces. The formation of entrapped oxide particle lines can be prevented by decreasing the traverse speed, increasing the rotation speed, or placing the butting faces on the advancing side of the tool where more efficient mixing occurs. Improvements in the tool design can also disrupt the oxidised layers more efficiently. Entrapped oxide particles are undesirable, as they may lead to a loss of mechanical properties or cracking, although they may be tolerated in certain circumstances. Entrapped oxide particles are very difficult to detect

using NDT methods. Bird (2003) claims to be able to detect its possibility by determining the depth of penetration with material noise ratio analysis in ultrasonic testing. (Leonard and Lockyer 2003; Jene et al. 2006; Vugrin et al. 2005; Fuller 2007; Bird 2003)

The origin of entrapped oxide particles in FSW welds of oxygen-free copper with about 40 ppm of phosphorus (Cu-OFP) was studied by Savolainen et al. (2008). It was noticed that oxide removal using nitric acid and the use of shielding gas both reduce the amount of entrapped oxide particles, and that best results are obtained when using both measures simultaneously.



**Figure 31. Entrapped oxide particle lines in a double-sided Cu-OF FSW weld.**

The second form of entrapped oxide particles is large inclusions. The presence of oxide inclusions (smaller than 300  $\mu\text{m}$ ) has been noticed in FSW welds of 50 mm thick copper. They are generally found near the surface in the overlap zone of the weld. They are thought to be caused by oxidation due to welding in air and they can be possibly avoided by using shielding gas during welding. The oxide inclusions can only be seen with metallographic studies, not by NDT methods. (SKB 2005)

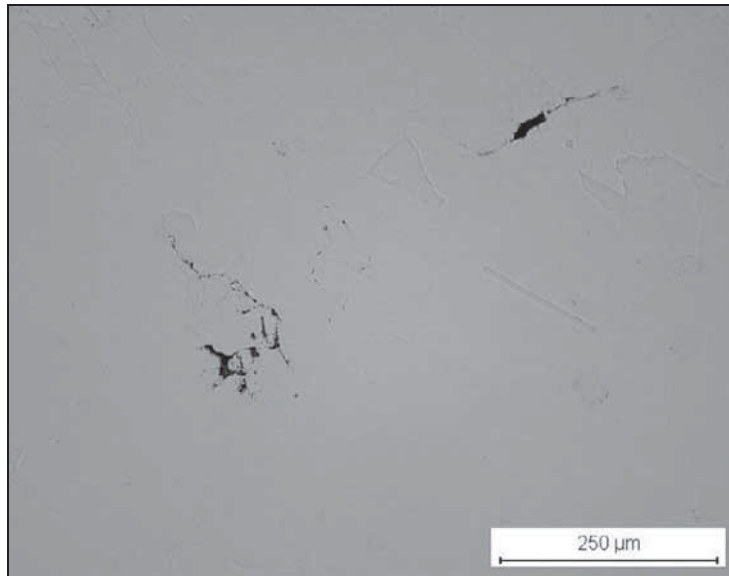


**Figure 32. Oxide inclusions in the overlap zone of 50 mm thick copper FSW weld (SKB 2005).**

#### 6.2.4 Joint Line Hooking

Joint line hooking (JLH) is generally seen in lap joints, but due to the special joint geometry of the spent nuclear fuel canister weld, it is also detected at the root of the 50 mm thick copper FSW weld. An example is shown in Figure 33. It forms when the vertical joint line is pulled out in the horizontal direction by the material flow. It may also be due to too long tool probe or too large plunge depth. JLH was most pronounced where the circular welds overlapped. The size of the defect has been reduced from the maximum of 4.5 mm to the minimum of 1 mm by shortening the tool probe and/or by using a mirror-image tool probe. JLH can be easily detected using ultrasound, but not with radiography. (SKB 2005; Ronneteg et al. 2006; Cederqvist 2006).

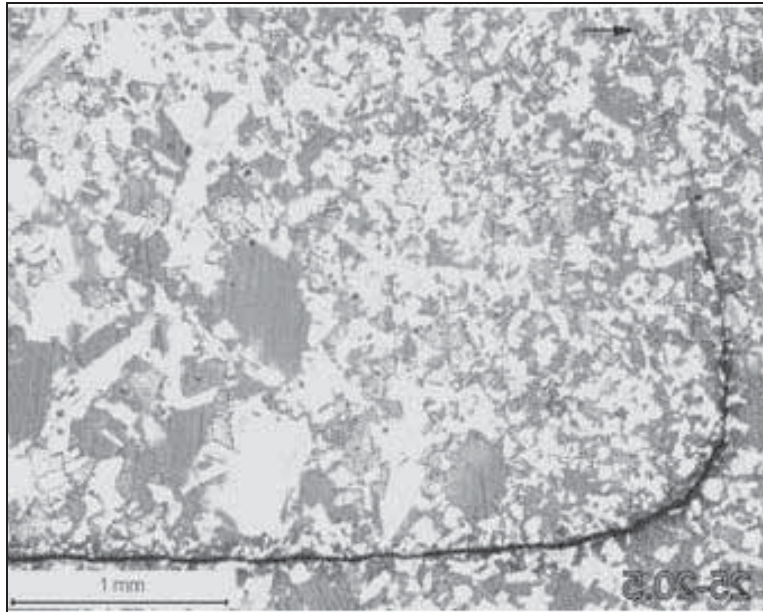


**Figure 33. Joint line hooking in a 50 mm thick copper FSW weld (Cederqvist 2006).**

#### 6.2.5 Faying Surface Flaw

According to Bird (2003), faying surface flaw is located at the top surface of the plate and it is a surface-breaking defect. It can contain oxides and it is metallurgically similar to a rolling lap. Figure 34 shows a faying surface flaw in a Cu-DHP weld.

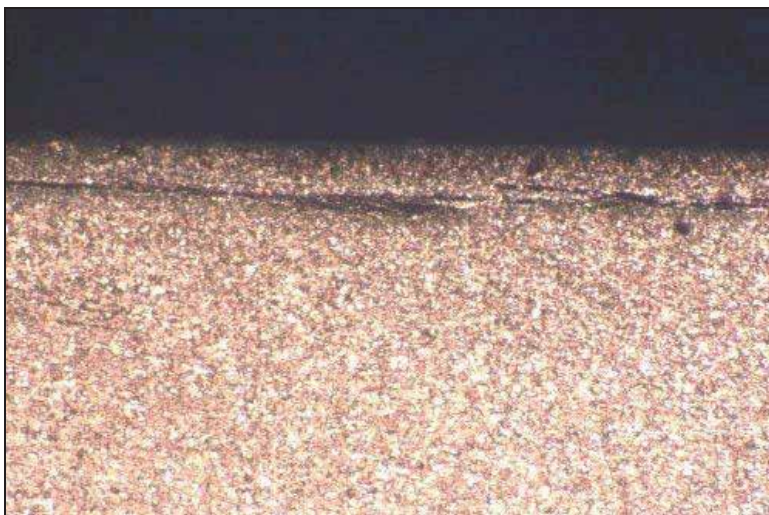


**Figure 34. Faying surface flaw in a Cu-DHP weld.**

There is no information in the literature regarding the formation or effects of the faying surface flaw. Colegrove et al. (2003) noticed that near the top of the weld, where the shoulder is dominant, the thin copper strip placed in the joint line (while friction stir welding aluminium) was very little disturbed by the flow. It can be assumed that the faying surface flaw is formed in a similar manner. Instead of the copper strip, it is the oxide layer from the joint line which is not properly dispersed near the tool shoulder and that is what the faying surface flaw consists of. Faying surface flaw may have harmful effects on the corrosion properties of the material.

#### 6.2.6 Tool Trace Material

Traces of nickel (20 ppm) were found in 50 mm thick copper FSW welds when using nickel-based superalloy Nimonic 105 as tool probe material (Cederqvist 2006). The trace material is usually located close to the surface, but it may be found anywhere in the weld. The size of the inclusions is smaller than 300  $\mu\text{m}$ . They originate from tool wear caused by high temperatures and process forces. They can be detected using high-sensitivity radiography or chemical analysis. (SKB 2005)

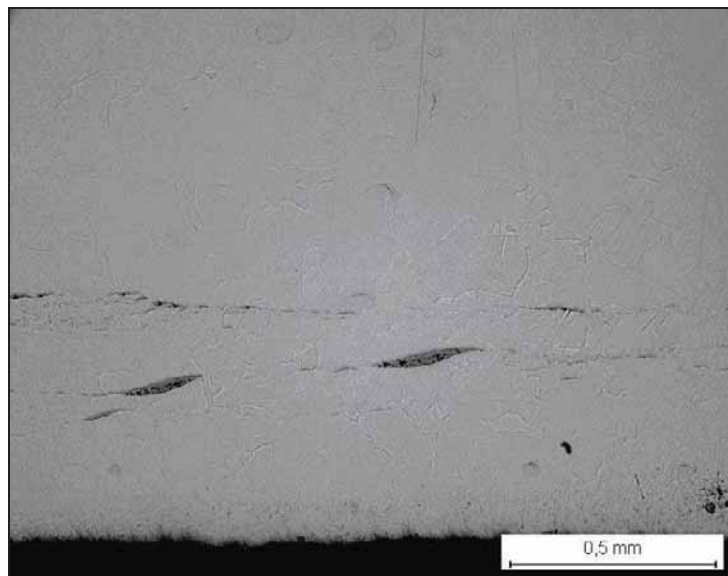


**Figure 35. Trace material from the nickel-based superalloy Nimonic 105 tool (SKB 2005).**

### 6.2.7 Pores

Copper FSW welds have been noticed to contain single pores or pore lines in all areas of the weld. Single pores are 0.1-0.5 mm in diameter, and pore lines may be up to 9 mm in length. They are due to incorrect welding parameters, especially too small tool plunge depth. They can only be detected with metallographic studies, not with NDT methods. (SKB 2005)

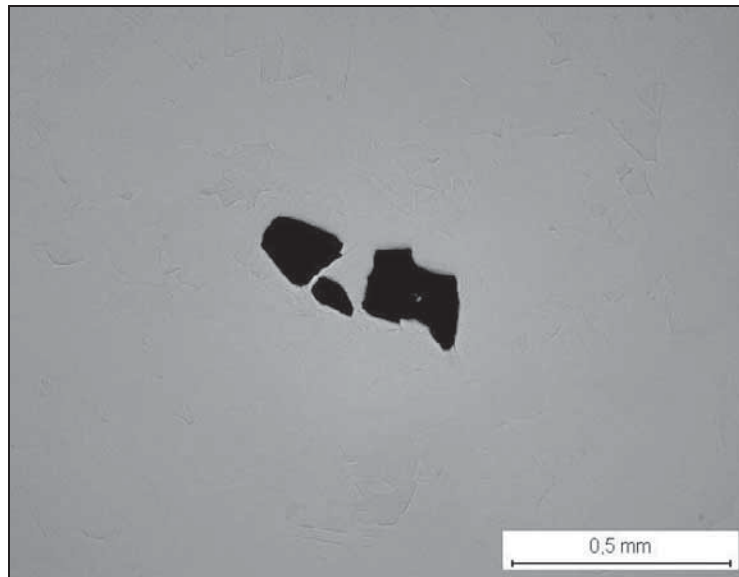


**Figure 36. Pores in the overlap zone of a 50 mm thick copper FSW weld (SKB 2005).**

## 7 MECHANICAL PROPERTIES OF THE WELDS

There is very little information available in the literature regarding the mechanical properties of copper FSW welds. Generally, the results have shown that the mechanical properties of copper FSW welds are similar to those of the base material, assuming that suitable welding parameters are used. The mechanical properties seem to be directly related to the material flow during FSW. (Çam 2011; Zettler et al. 2006)

### 7.1 Tensile Tests

Heat input during welding and the resulting grain size influence the tensile properties of copper FSW welds. Lower heat input (lower tool rotation speed or higher traverse speed) with reduced grain size results in increased yield and tensile strength values and reduced ductility. Tensile properties of the welds as compared to those of the base material depend on the condition of the base material (annealed or work hardened) as well as on the heat input of the welding. (Surekha and Els-Botes 2011; Xie et al. 2007)

Xue et al. (2011b) studied FSW of pure copper using welding parameters with low heat input and rapid water cooling on the trailing edge of the tool. The resulting welds exhibited nearly equal tensile properties (yield and ultimate tensile strength values as well as elongation to fracture) as compared to the base material.

Sun and Fujii (2010) welded 2 mm thick commercially pure copper. They noticed that increasing the applied load decreases the resulting grain size more than reducing the tool rotation speed. By increasing the load and consequently obtaining higher hardness than that of the base material, the samples fractured at the base material in tensile tests.

Andersson and Andrews (1999) compared the tensile strength values of 10 mm thick phosphorus-doped copper FSW welds at various locations (start, middle, and end of the weld) and the base material. Tensile strength values of the welds were uniform, but lower as compared to those of the base material (216-218 MPa and 280 MPa, respectively). The welds fractured at random locations along the gauge length showing no preferred location.

## 7.2 Hardness Profiles

Two competitive mechanisms influence the hardness of copper FSW welds: anneal softening and grain refinement. The hardness of the weld depends on the dominant mechanism. The weld hardness in relation to that of the base material depends on the condition of the base material (annealed or work-hardened) as well as on the heat input of the welding. Heat input increases with increasing tool rotation rate and decreasing traverse speed and leads to annealing softening and lower hardness. Lowering the heat input leads to refined grain size and eventually to higher hardness of the welds as compared to the base material. (Xie et al. 2007; Surekha and Els-Botes 2011; Çam 2011)

An interesting approach was that by Xue et al. (2011b). They made FSW welds of pure copper with minimal heat input and rapid water cooling on the trailing edge of the tool. The resulting joints had hardness nearly equal to that of the work-hardened base material.

## **8 OBJECTIVE OF THE DOCTORAL THESIS**

The application of using FSW in the sealing of copper corrosion barrier canisters for final disposal of spent nuclear fuel has made FSW of copper an important research subject. Increased understanding of the different factors influencing the microstructure and properties of the welds is necessary to ensure reliable modelling of the behaviour of the spent nuclear fuel canister. As the required life-time (100,000 years) of the canister cannot be experimentally validated, the durability of the canister must be predicted based on shorter-term experiments and modelling.

Cu/Al dissimilar metal FSW welds are of interest to the electric power industry. Cu/Al dissimilar metal FSW joints with good mechanical properties and high electrical conductivity could be useful in many applications.

The aim of this Doctoral Thesis was to study FSW of copper and Cu/Al dissimilar metal FSW as well as the microstructure and properties of the welds. The welding configurations in this Doctoral Thesis are limited to butt welding. Single-sided welding of 5 mm thick and double-sided welding of 10-11 mm thick material was studied. The microstructure and mechanical properties of the copper and Cu/Al dissimilar metal FSW welds were studied.

Other topics studied in this Doctoral Thesis were the origin, detection, and avoidance of entrapped oxide particles as well as the localization of strain in different parts of the copper corrosion barrier canister for spent nuclear fuel.

## **9 EXPERIMENTAL**

The experimental part of the study included welding tests, microstructural studies, and evaluation of the mechanical properties of the welds.

### **9.1 Base Materials**

The following base materials were studied:

Cu-OF: Oxygen-free electrolytically refined copper with less than 40 ppm impurities and less than 10 ppm oxygen. Table 3 shows the composition of the Cu-OF material. Cu-OF was in a cold-rolled condition and the plate thickness was 10 mm. It is a work hardenable material. Material was provided by Luvata Oy (formerly Outokumpu Poricopper Oy).

Cu-DHP: Phosphorus-deoxidised copper – high residual phosphorus with less than 40 ppm impurities, less than 30 ppm oxygen, and about 250 ppm phosphorus. Table 3 shows the composition of the Cu-DHP material. Cu-DHP was hot rolled with an 11 mm plate thickness. It is a solution strengthened, work hardenable material. Material was provided by Luvata Oy (formerly Outokumpu Poricopper Oy).

**Table 3. The chemical compositions of Cu-OF and Cu-DHP materials (Luvata Oy, formerly Outokumpu Poricopper Oy).**

	Cu-OF (ppm)	Cu-DHP (ppm)
<b>Cu</b>	99.997%	99.981%
<b>Ag</b>	10.4	11
<b>Al</b>	<0.08	<1
<b>As</b>	0.99	2
<b>Bi</b>	0.32	<1
<b>Cr</b>	0.06	<1
<b>Fe</b>	0.9	5
<b>H</b>	0.5	0.62
<b>Mg</b>	2	<1
<b>Mn</b>	<0.1	<1
<b>Ni</b>	1.1	1
<b>O</b>	2.6	25
<b>P</b>	<0.3	161
<b>Pb</b>	0.22	<2
<b>S</b>	7.1	4
<b>Sn</b>	0.1	<2
<b>Te</b>	0.33	<4
<b>Zn</b>	0.5	<2

Cu-OFP: oxygen-free copper with approximately 50 ppm phosphorus. Table 4 shows the composition of Cu-OFP. Cu-OFP was in hot-worked condition (hot-rolled). The material was provided by Posiva Oy.

**Table 4. The chemical composition of Cu-OFP (Posiva Oy).**

		Spec.	Meas.	
			168791	168792
<b>Cu</b>	% min	99,99	99,992	99,992
<b>Ag</b>	ppm max	25	13,9	14,1
<b>As</b>	"	5	0,92	0,98
<b>Bi</b>	"	1	0,13	0,14
<b>Cd</b>	"	1	<0,003	<0,003
<b>Fe</b>	"	10	0,6	0,7
<b>H</b>	"	<0.6	0,5	0,3
<b>Hg</b>	"	1	<0,5	<0,5
<b>Mn</b>	"	0.5	<0,1	<0,1
<b>Ni</b>	"	10	0,6	0,8
<b>O</b>	"	<5	1,8	1,5
<b>P</b>	"	30-70	51	49
<b>Pb</b>	"	5	0,26	0,27
<b>S</b>	"	<8	5,0	5,2
<b>Sb</b>	"	4	0,06	0,07
<b>Se</b>	"	3	0,1	<0,1
<b>Sn</b>	"	2	0,06	0,06
<b>Te</b>	"	2	0,08	0,07
<b>Zn</b>	"	1	<0,1	<0,1

In the Cu/Al dissimilar metal FSW welds the studied base materials were Cu-OF and extruded aluminium alloy EN-AW 6060 T6 with plate thickness of 10 mm. Aluminium alloy EN-AW 6060 T6 was provided by Nordic Aluminium Oy.

Good quality, defect-free 50 mm thick Cu-OF FSW and EB welds as well as the base materials were provided by SKB and Posiva Oy, respectively. The lid base materials were forged and tube base materials were extruded. The base materials were oxygen-free copper with nominally 30-70 ppm phosphorus (specific compositions were different for each of the four lid and tube base materials).

## 9.2 Tools

Two tool types were used in the welding experiments. All welding trials except the banding experiments were made with nickel-based precipitation hardenable superalloy IN738LC tools (chemical composition is shown in Table 5). The alloy IN738LC has excellent high temperature creep-rupture strength and maximum operating temperature of about 980 °C. It is used for turbine blades and other demanding applications. The tool geometry used for the nickel-based superalloy IN738LC tools is shown in Figure 37. The tool consists of a shank, a concave shoulder, a conical probe with three flats, and cooling channels inside the tool.

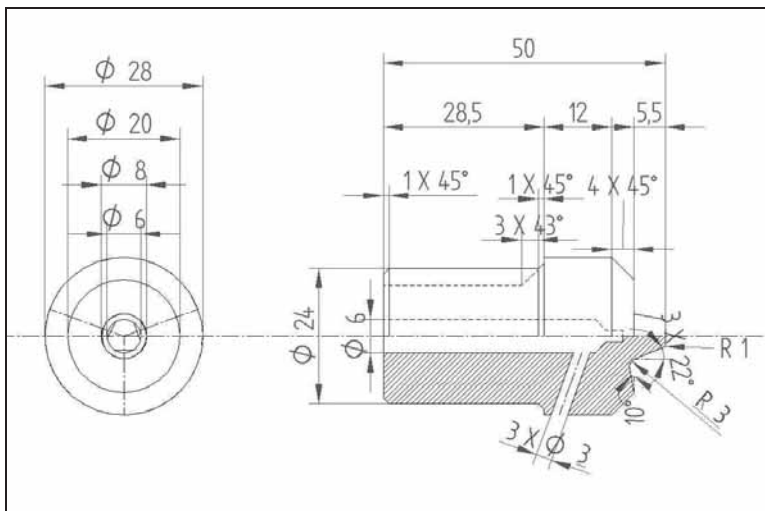


Figure 37. The tool geometry used for the nickel-based superalloy IN738LC tools.

**Table 5. The chemical composition of the nickel-based superalloy IN738LC tool material in wt. %.**

IN738LC		
<b>Al</b>		1.84
<b>B</b>		0.011
<b>C</b>		0.151
<b>Co</b>		18.9
<b>Cr</b>		22.43
<b>Cu</b>	<	0.02
<b>Fe</b>		0.15
<b>Hf</b>	<	0.05
<b>Mg</b>	ppm	32.3
<b>Mn</b>	<	0.05
<b>Mo</b>	<	0.05
<b>N</b>	ppm	34
<b>Nb</b>		1.01
<b>Ni</b>		48.05
<b>O</b>	ppm	7
<b>P</b>	<	0.002
<b>S</b>	ppm	10
<b>Si</b>	<	0.1
<b>Ta</b>		1.41
<b>Ti</b>		3.78
<b>V</b>	<	0.1
<b>W</b>		2.03
<b>Y</b>	<	0.05
<b>Zr</b>		0.092

A “cold” Cu-OF weld showing banding was made with a commercially available PCBN tool from MegaStir Inc. PCBN is a superabrasive material primarily used in machining of Ni-based superalloys, high-strength ferrous materials, and cast irons. As an FSW tool material, it is used mainly for joining high temperature materials such as steels or stainless steels. PCBN has a very high hot strength. The PCBN tool had a slightly concave shoulder and a conical probe with three flats. Probe length was 6 mm, probe diameter 9 mm at the root of the probe and 6 mm at the tip of the probe. The tool geometry of the PCBN tool was very similar to that of the IN738LC tools. The lower friction coefficient of PCBN as compared to IN738LC resulted in less frictional heating of the base material during FSW and, consequently, a “cold” FSW weld.

### 9.3 Arrangements

A converted milling machine (TOS FGS 50T Plus) was used for the friction stir welding trials. Figure 38 shows an overall view of the arrangement. The arrangement included tool temperature, power, and tool rotation speed measurement as well as a near-infrared sensitive video camera, air/gas cooling of the tool, and clamping. The tools had internal cooling channels and they were usually air-cooled. Gas shielding and internal tool cooling by carbon dioxide or argon were used in some welds.



**Figure 38. An overall view of the welding arrangement.**

Figure 39 shows the clamping. Blue L-bars were used to push the sample plates together from the sides and thick bars to clamp them rigidly to the backing bars (one thick and one thin, which had to be replaced occasionally as the heat from welding distorted it).

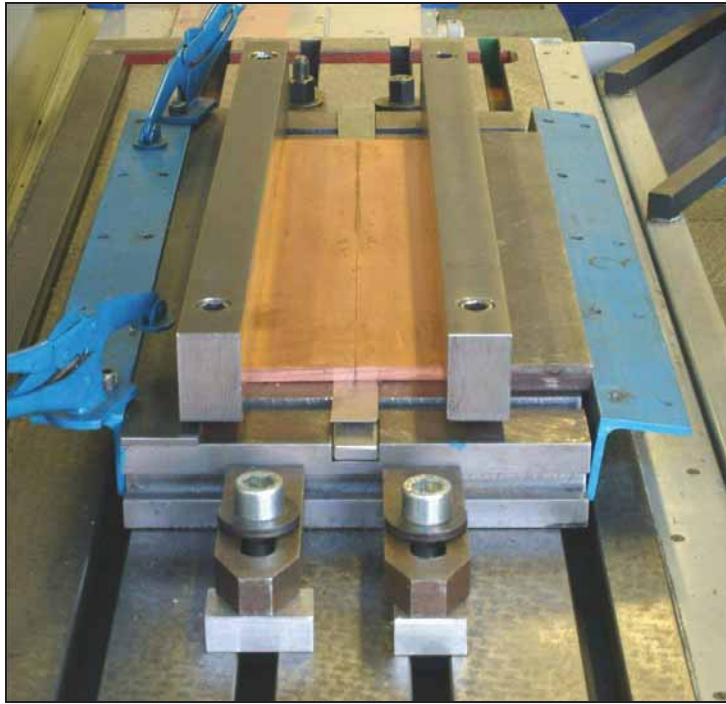


**Figure 39. The clamping arrangement.**

#### **9.4 Welding Trials**

Prior to welding, joint preparation was used when needed by cleaning, grinding, or etching the surfaces to be welded. The plates were clamped tightly against each other and the backing plate. Before welding the tool rotation speed was set to the desired value. The plunge depth was manually controlled by a Z-axis tool display. The traverse speed was also manually controlled and it was accelerated to the desired value over a distance of 20-30 mm in order to avoid high stresses on the tool. Tool tilt angle was  $2.5^\circ$  for copper FSW welds and it was varied for the Cu/Al dissimilar metal FSW joints. In double-sided welding, the plates were first welded from one side and then after flash removal from the opposite side. The length of the probe and the plunge depth were chosen so that the double-sided welds overlapped by 1-2 mm. The shielding gas (when used) was argon. Prior to welding the work pieces were put in a plastic cover encompassing also the welding head and table and rinsed with argon for at least five minutes so that argon would replace air also in the grooves (argon is heavier than air). The work pieces were then welded in argon inside the plastic cover.

## 9.5 Experimental Methods

Sample preparation of copper specimens is challenging especially for scanning electron microscopy (SEM) and electron backscatter diffraction (EBSD) studies and for the detection of entrapped oxide particles. Much time and effort was put to the development of sample preparation methods. FSW welds were studied using optical microscopy, SEM, EBSD, tensile tests, hardness measurements, bend tests, optical strain measurement, hydrogen annealing, and electrical resistivity measurements.

### 9.5.1 Sample Preparation

The basic sample preparation of grinding and polishing was performed with Struers LaboPol-21 equipment using SiC water grinding papers and diamond polishing paste down to 1  $\mu\text{m}$  particle size.

The samples were further electrolytically polished to ensure a strain-free surface for SEM and EBSD studies. The samples were electrolytically polished using Struers LectroPol-5. The polishing liquid was D2 (250 ml phosphoric acid, 500 ml distilled water, 250 ml ethanol, 2 ml Vogel's Sparbeize, 50 ml propanol, and 5 g urea). Polishing parameters varied depending on the size of the sample.

An experimental electrolytic etching method was used to study the microstructure of the FSW welds, for example to reveal the presence of entrapped oxide particles. The method exaggerates the size and amount of oxide particles in order to make them more visible. The method removes the entrapped oxide particles and increases the size of the remaining "holes". The electrolytic etching was performed using Struers LectroPol-5 and electrolyte D2. The parameters of the electrolytic etching were more severe than in electrolytic polishing and they depended on the size of the sample.

To reveal the microstructure for optical microscopy, the samples were etched using a 50%/50% solution of distilled water and nitric acid for 60 s.

Oxide removal prior to welding was performed by immersing the samples in a 50% / 50% solution of water and 65% HNO<sub>3</sub> for 30 s. The samples were ultrasonically cleaned in ethanol before and after oxide removal. The samples were welded promptly after oxide removal to minimize the formation of a new oxide layer.

### 9.5.2 Optical Microscopy

Optical microscopy was performed using Nikon Epiphot 200 microscope. Samples were either etched or electrolytically etched using an experimental method to reveal the feature to be studied.

### 9.5.3 Scanning Electron Microscopy

Scanning electron microscopy (SEM) was used to study the features in the copper FSW welds and base materials. Zeiss DMS 962 SEM was used to study the Cu-OF and Cu-DHP FSW welds as well as the Cu/Al dissimilar metal FSW welds. For other FSW welds, Zeiss Ultra 55 field emission gun scanning electron microscope (FEG-SEM) was used. SEM parameters depended on the used equipment and on the studied samples. Energy dispersive x-ray spectroscopy (EDS) was also used for the chemical composition measurements of the samples.

Some fracture surfaces of Cu/Al dissimilar metal FSW welds were nickel-plated to preserve all the surface layers for the SEM examination of the cross-sections.

### 9.5.4 Electron Backscatter Diffraction

Electron backscatter diffraction (EBSD) method was extensively used in the studies. It was used to map the crystallographic orientations in the base materials and the weld nuggets. EBSD acquisition and analyses were performed with Oxford Instruments Nordlys II camera and Channel 5 software (originally by HKL Technologies). Acceleration voltage was 20 keV, working distance 20 mm, and tilting of the samples 70°. Other EBSD parameters, such as step size and magnification, varied depending on the application.

### 9.5.5 Tensile Tests

The transverse tensile tests of 5 mm thick Cu-OF and Cu-DHP FSW welds were performed using an MTS 810 testing machine according to the standard SFS-EN 895. The standard is for fusion welds, but it is applicable also to friction stir welded joints. Sub-size transverse test specimens according to ASTM E 8M – 96 were used. The strain rate was  $4 \times 10^{-4}$  1/s with an extensometer and  $9 \times 10^{-4}$  1/s after the removal of the extensometer. Two specimens were made of each weld. Figure 40 shows the geometry and dimensions of the sub-size transverse tensile test specimens. The welds were located at the centre of the test specimens and they cover a maximum of 20 mm of the total gauge length (32 mm).

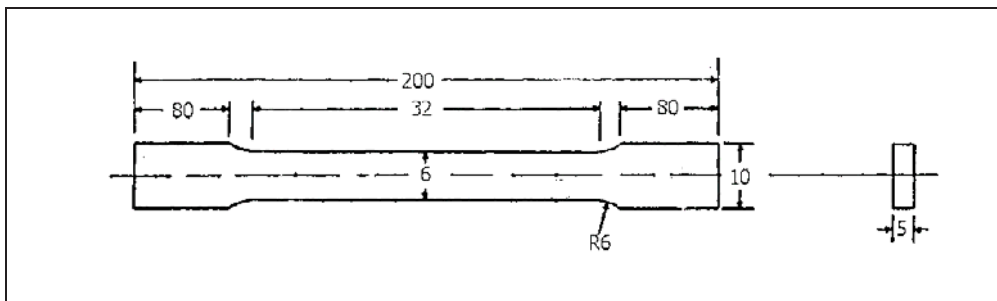


**Figure 40. The geometry and dimensions of the sub-size transverse tensile test specimens. The image is not in scale. (ASTM E 8M – 96)**

Tensile testing for studying the localization of plastic strain in different parts of the copper canister for spent nuclear fuel was performed using an MTS 810 material test system. The Cu-OF samples were tested at constant strain rates of  $5 \times 10^{-4}$ ,  $10^{-5}$ , and  $10^{-6}$  1/s using flat tensile test samples. Gauge length of the dog-bone shaped samples was 40 mm, width 35 mm, and thickness 5 mm. FSW and EB welds were cut transverse to the welding direction by electro-discharge machining and they were located at the centre of the gauge length.

Transverse tensile tests for Cu/Al dissimilar metal FSW samples were performed using an MTS 810 material test system. The dimensions of the flat specimens were 4 x 25 x 176 mm for the one-sided welds and 8 x 25 x 176 mm for the double-sided welds. The specimens were machined to remove the effect of the weld surfaces. Strain rate was  $5 \times 10^{-4}$  1/s. Welds were located at the centre of the specimens.

### 9.5.6 Hardness Measurements

Buehler Omnimet hardness tester was used for the hardness profile measurements of the Cu-OF and Cu-DHP FSW welds. The hardness was measured from the centre of the weld. For Cu-OF the weight of 1 kg was used (HV 1), whereas for Cu-DHP the weight of 0.5 kg was used (HV 0.5). The results were verified with Zwick 3202 and Gnehm Brickers 220 hardness measurement devices.

The hardness of the tool materials was measured using Zwick 3202 or Gnehm Brickers 220 hardness measurement devices. The result is the average of five measurements.

Hardness profiles of the Cu-OF FSW samples were measured using Buehler Micromet 2101 microhardness tester and weight of 1 kg (HV 1). Hardness profiles were measured both horizontally and vertically in the middle of the weld.

Buehler Omnimet was used to measure the hardness (HV) of the Cu/Al dissimilar metal FSW welds. Hardness profiles were measured horizontally at the distance of 2 mm from the surface (in the double-sided welds from both surfaces). Step size was 0.5 mm and the weight of 0.5 kg was used.

### 9.5.7 Bend Tests

Three point bend tests of Cu-OF and Cu-DHP FSW welds were performed according to the standard SFS-EN 910 using a former and transverse face bend test specimen (FBB). Both sides of the welds were tested. The specimen thickness ( $a$ ) was equal to the thickness of the base material adjacent to the welded joint. Width of the test specimen ( $b$ ) was 22 mm and the total length ( $L_t$ ) varied between 200 and 210 mm, depending on the width of the plates. The specimen surfaces were machined and the edges of the test specimens on the face in tension were rounded ( $r < 0.2 a$ ). Diameter of the rollers was 30 mm, distance between the rollers was 40 mm, and the diameter of the former was 20 mm. Specimens were bent gradually so that the minimum angle was 90°, 105°, 120°, and 180°. Figure 41 shows the geometry of the bend test specimens.

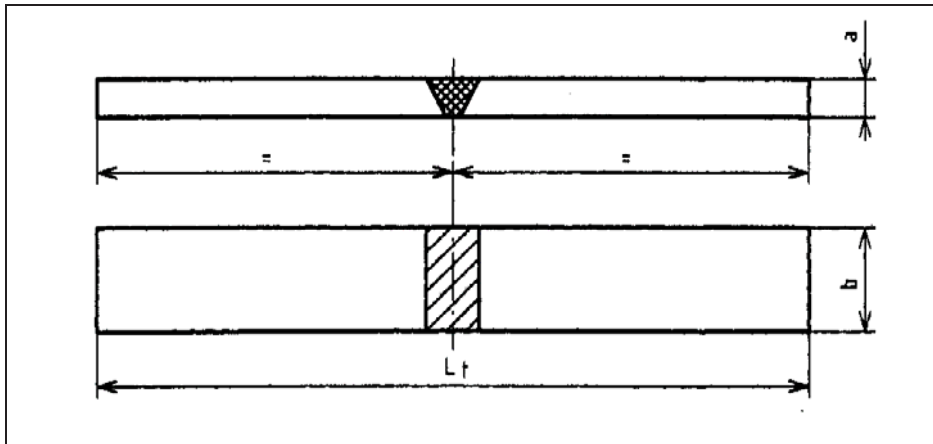


**Figure 41. The geometry of the bend test specimens (SFS-EN 910).**

#### 9.5.8 Optical Strain Measurement

An optical strain measurement system consisting of a CCD camera and a PC with imaging software was used to measure and analyze the deformation of 50 mm thick Cu-OFP FSW samples containing almost the entire weld or material thickness. Images for optical strain measurement were obtained at a rate of 0.3 Hz during tensile testing with an MTS 810 material test system at a constant strain rate of  $5 \times 10^{-4}$  1/s using flat tensile test samples. FSW and EB weld samples were taken transverse to the welding direction by electro-discharge machining, which provides a good surface for optical strain measurement without additional painting. Gauge length of the samples was 40 mm, width 35 mm, and thickness 5 mm. Welds were located at the centre of the gauge length. The system records successive images of the sample surface during deformation and constructs the deformation fields using advanced cross-correlation algorithms. Deformation fields were determined using StrainMaster optical strain measurement system delivered by LaVision. Figure 42 shows the optical strain measurement arrangement.

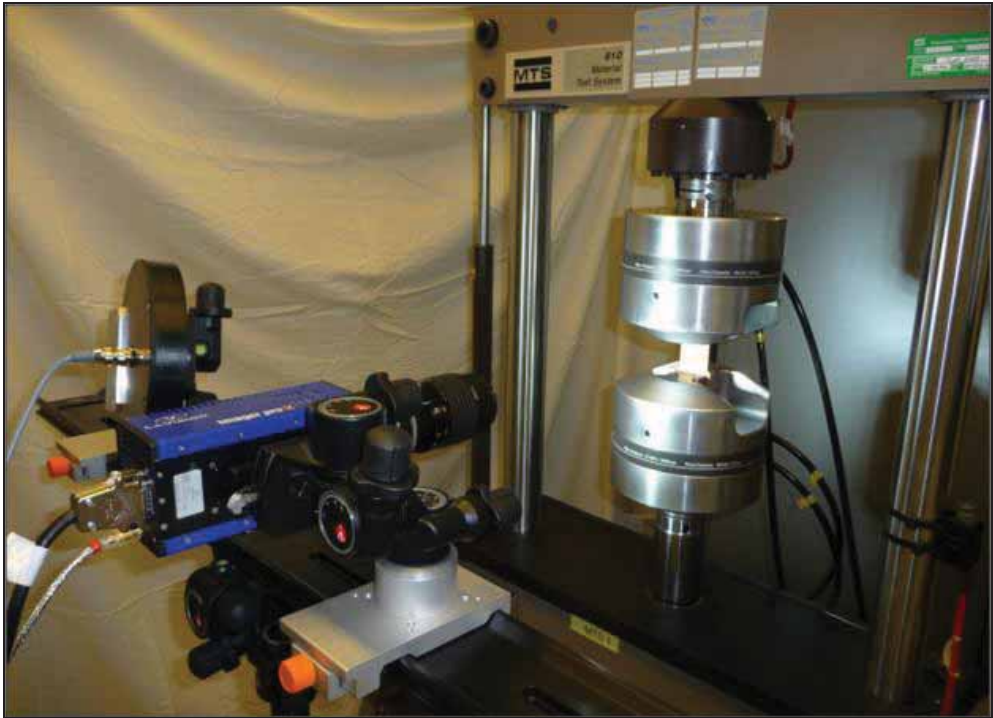


**Figure 42. Arrangement of the optical strain measurement. The electro-discharge machined dog-bone shaped sample is being tensile tested using an MTS 810 material test system. A powerful lamp is used to provide sufficient lighting of the sample for obtaining the images by a charge-coupled device (CCD) camera.**

#### 9.5.9 Hydrogen Annealing

Friction stir welded Cu-OFP samples with different joint preparation methods and shielding gas combinations were hydrogen annealed in order to reveal the presence of oxide particles in the welds. Hydrogen annealing was carried out by annealing the electrolytically polished samples for 30 min at 850 °C in N + 10 % H<sub>2</sub> gas. After annealing the samples were left to cool with the furnace. During hydrogen annealing hydrogen reacts with oxide particles in the copper producing water. At the elevated temperature of hydrogen annealing, the water evaporates leaving voids in the structure.

#### 9.5.10 Electrical Resistivity Measurements

The electrical resistivity measurements were made using a Cropico Digital Microhmmeter DO7. The measurement length was 99 mm. Resistance values of both base materials and

welded Al/Cu joints were measured. In the case of welded joints, the specimens were positioned so that the original joint line before welding was in the middle of the measurement length. The arrangements of the electrical resistivity measurements are shown in Figure 43.

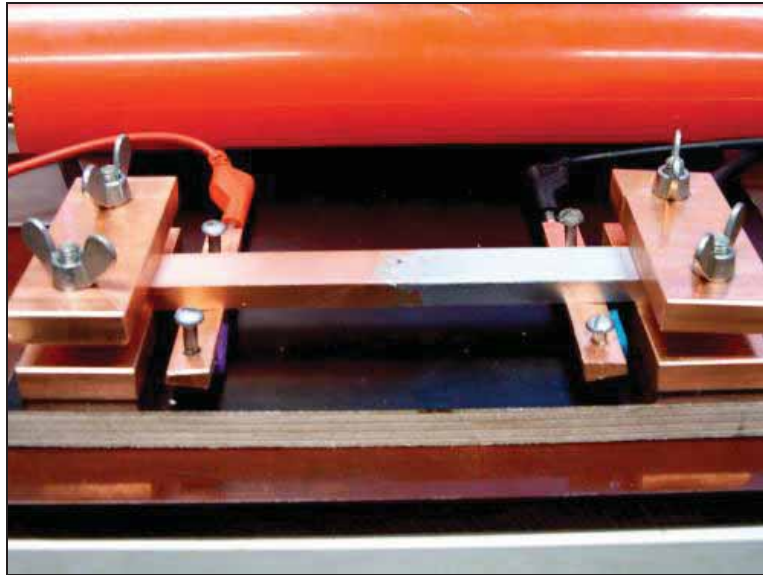


**Figure 43. The arrangement of electrical conductivity measurements. The measurement length was 99 mm.**

#### 9.5.11 Temperature and Power Measurements

Temperature measurement was performed using a K-type thermal element inside the tool pin. Logging occurred once per second and was the average of 18 000 measurements. The thermal element was kept in constant contact with the tool by a spring. The results obtained with the thermal element inside the tool were not absolute values, because the cooling of the tool affected the measurements. Power used by the milling machine was measured from the inverter feeding the spindle motor. The idle power of the machine was approximately 1 kW. The measurements were made using Virtual Bench Logger program.

## 10 RESULTS

The results obtained in this work show the microstructure and mechanical properties of copper and Cu/Al dissimilar metal FSW welds. The results also include the origin, detection, and avoidance of entrapped oxide particles as well as the localization of plastic strain in different parts of the copper corrosion barrier canister for spent nuclear fuel.

### 10.1 Microstructure

Different aspects of the microstructure of copper FSW welds were studied. The studied features included grain structure, grain size, texture, and precipitates.

#### 10.1.1 Grain Structure

Figures 44 and 45 show the transverse cross-sections of double-sided copper FSW welds with 10 mm plate thickness and 50 mm thick copper FSW welds, respectively. The base material in the 5 mm thick weld is cold-rolled Cu-OF with large grain size and elongated grain structure. The extruded and forged base materials of the 50 mm thick Cu-OFP FSW weld have small grain sizes. In the 50 mm thick weld the different zones of the microstructure of the weld are clearly visible, whereas in the 5 mm thick weld they are not clearly revealed.



**Figure 44. Double-sided FSW weld of cold-rolled Cu-OF with 10 mm plate thickness. Smaller grain size in the weld is evident. No separate zones are readily seen contrary to Figure 45.**



**Figure 45. Many microstructural zones are visible in the transverse cross-section of a 50 mm thick Cu-OFP FSW weld. Forged lid (on the left, retreating side) and extruded tube (on the right, advancing side) are the base materials. (Savolainen et al. 2010)**

Grain structures of the double-sided 10 and 11 mm thick Cu-OF and Cu-DHP, respectively, FSW welds were studied using EBSD. The EBSD maps were taken at the centre of the weld nugget. Figures 46 - 49 show examples of the results obtained with EBSD of the base materials and of the weld nuggets. The orientation maps form pairs. The first map of the pair is the orientation map with colours corresponding to the crystallographic orientation of each point as defined by the Euler angles. The grain boundaries are marked in black, the low angle boundaries (minimum misorientations  $1.2^\circ$ ) in grey and the twin boundaries in yellow. The percentage of the twin boundaries of the total grain boundary length is calculated based on the EBSD results. The amount of twin boundaries is higher in the FSW welds than in the base materials, especially in the Cu-OF base material. In the second map of the pair the intra-grain misorientations caused by the dislocations are calculated and the grains are classified accordingly as deformed (high dislocation density), substructured (low angle boundaries inside the grains), and recrystallized (low dislocation density). (Savolainen et al. 2004)

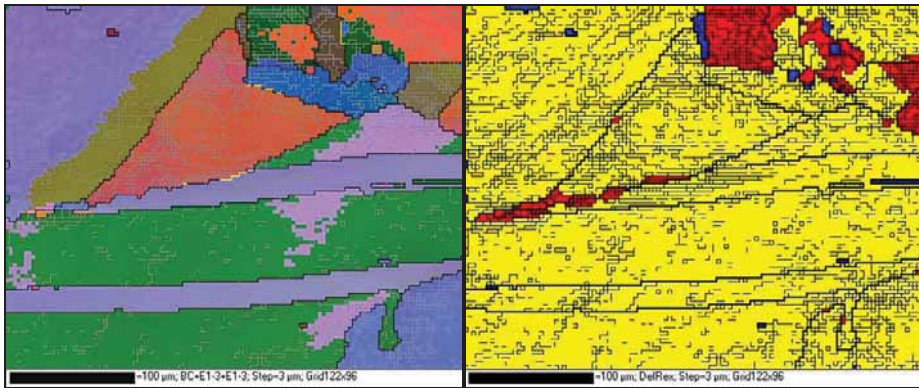


**Figure 46. EBSD maps of the cold-rolled Cu-OF base material. On the left: The percentage of twin boundaries of the total grain boundary length is 2.1 %. The grains are strongly elongated in the horizontal direction. On the right: Recrystallized fraction is shown in blue, substructured in yellow, and deformed in red colour. (Savolainen et al. 2004)**

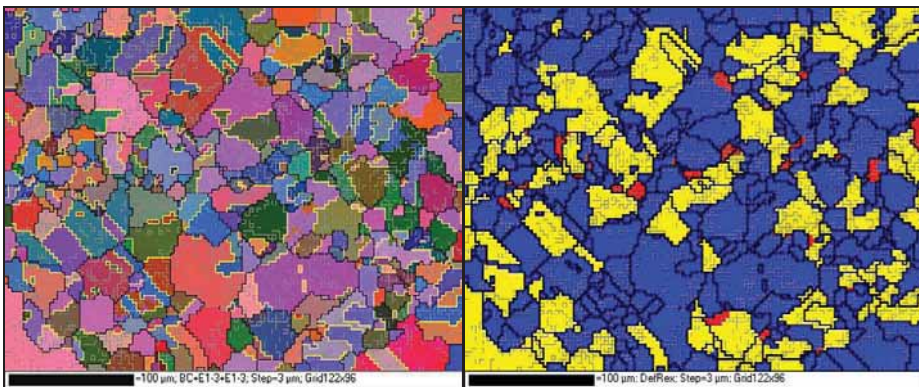


**Figure 47. EBSD maps of the Cu-OF FSW weld nugget. On the left: Twin boundaries are highlighted with yellow colour. The percentage of twin boundaries of the total grain boundary length is 34.9 %. The weld exhibits a fine, uniform, equiaxed grain structure. On the right: Recrystallized fraction is shown in blue, substructured in yellow, and deformed in red colour. (Savolainen et al. 2004)**

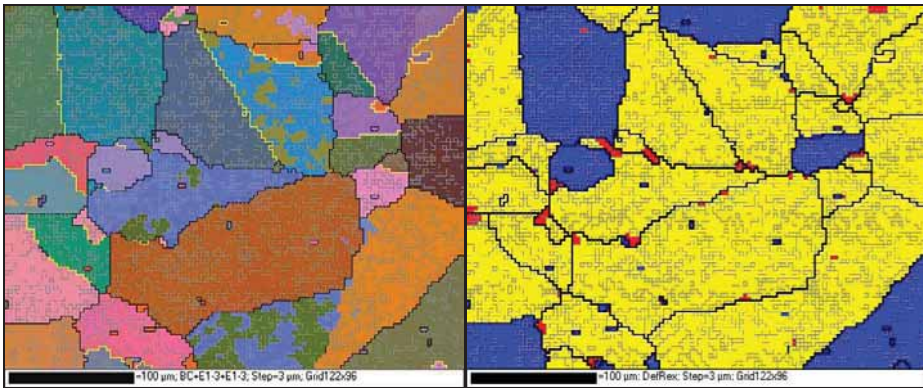


**Figure 48. EBSD maps of the Cu-DHP base material. On the left: Twin boundaries are highlighted with yellow colour. The percentage of twin boundaries of the total grain boundary length is 12.3 %. The grains are slightly elongated in the horizontal direction. On the right: Recrystallized fraction is shown in blue, substructured in yellow, and deformed in red colour. (Savolainen et al. 2004)**

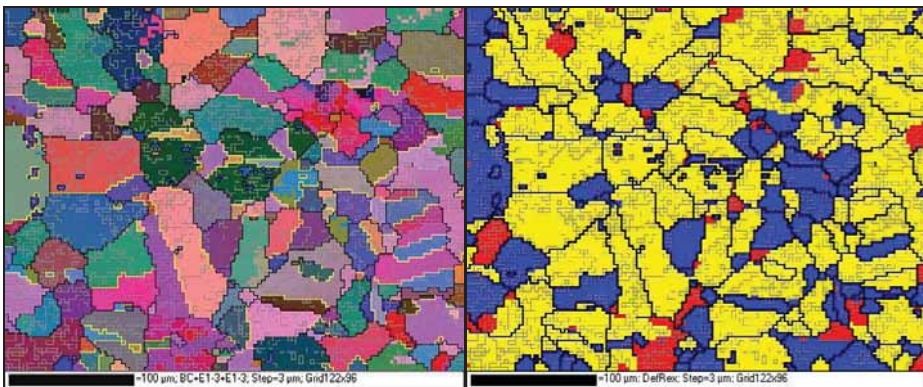


**Figure 49. EBSD maps of the Cu-DHP FSW weld nugget. On the left: Twin boundaries are highlighted with yellow. The percentage of twin boundaries of the total grain boundary length is 18.4 %. The weld exhibits a fine, uniform, equiaxed grain structure as compared to the grain structure of the base material. On the right: Recrystallized fraction is shown in blue, substructured in yellow, and deformed in red colour. (Savolainen et al. 2004)**

### 10.1.2 Grain Size

Grain size of the 10-11 mm thick Cu-OF and Cu-DHP base materials as well as of FSW welds was studied using EBSD. Table 6 shows the results when considering the twin boundaries as grain boundaries (EX + T) and when ignoring the twin boundaries (EX – T). The grain size was studied at the centre of the weld nugget in the FSW welds. FSW resulted in a smaller grain size as compared to that of the base materials. The cold-rolled

Cu-OF base material had a very large grain size of about 145  $\mu\text{m}$  horizontally and 75  $\mu\text{m}$  vertically. The corresponding FSW weld had an equiaxed grain size of about 15-20  $\mu\text{m}$ . The hot-rolled Cu-DHP base material had a smaller initial grain size of 55  $\mu\text{m}$  horizontally and 35  $\mu\text{m}$  vertically. The corresponding Cu-DHP FSW weld had an equiaxed grain size of about 20-25  $\mu\text{m}$ . (Savolainen et al. 2004)

**Table 6. The average grain sizes ( $\mu\text{m}$ ) of the unwelded base materials and of the weld nuggets. The grain sizes are determined by considering the twin boundaries as grain boundaries (EX + T) and by ignoring the twin boundaries (EX – T). (Modified from Savolainen et al. 2004)**

	Location	Direction	EX+T	EX-T
<b>Cu-OF</b>	Base	Horizontal	143	145
		Vertical	73	76
	Nugget	Horizontal	15	22
		Vertical	15	20
<b>Cu-DHP</b>	Base	Horizontal	53	57
		Vertical	35	37
	Nugget	Horizontal	21	24
		Vertical	18	20

The grain sizes of the 50 mm thick Cu-OF FSW and EB welds were compared to those of the forged and extruded base materials. In the base materials the grain size varies from 60 to 75  $\mu\text{m}$  depending on the manufacturing method. In FSW welds the grain size is equal to or smaller (60  $\mu\text{m}$ ) than that in the base materials. In EB welds the grain size is significantly larger than that in the base materials, exhibiting grains up to 12 mm in length. Figures 50 and 51 show the transition regions from the FSW and EB welds to the base materials. The transition from the FSW weld to the base material is smooth (Figure 50), while the grain size gradient between the EB weld and the base material is very steep (Figure 51).

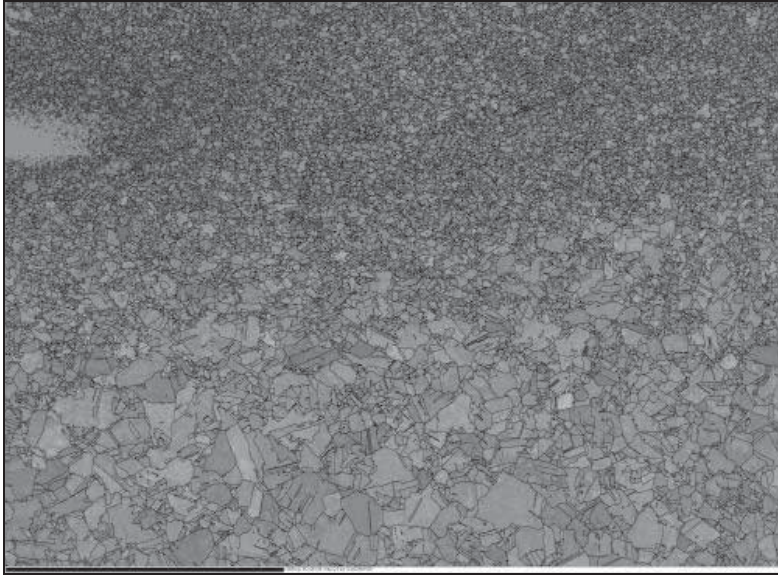


**Figure 50.** An EBSD map of the root of an FSW weld in transverse direction. Part of the original joint line can be seen on the upper left corner. The weld is on the top and forged lid material on the bottom. The transition from the weld to the base material is smooth. Length of the scale bar is 2000  $\mu\text{m}$ . (Savolainen et al. 2010)

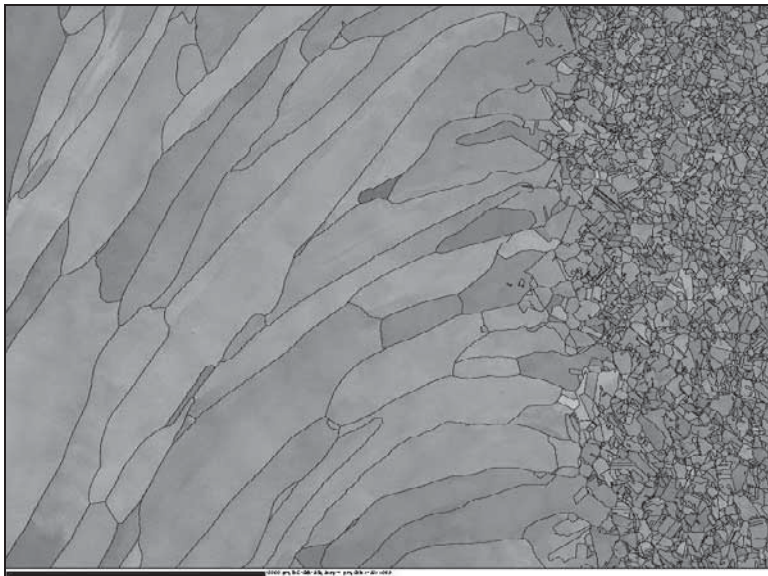


**Figure 51.** An EBSD map showing a top view of an EB weld. Large grain size of the EB weld and the steep grain size gradient can be clearly seen. Base material is on the right. Length of the scale bar is 2000  $\mu\text{m}$ . (Savolainen et al. 2010)

### 10.1.3 Texture

Figure 52 shows the transition from the weld nugget to the base material in a 5 mm thick FSW weld of cold-rolled Cu-OF. The weld is on the left and base material with its large grain size is on the right. Euler maps show the grain structure and pole figures show the texture of the different zones in the weld. On the left hand side, the weld nugget has an equiaxed grain structure and an almost random texture produced by DRX. At the centre, the TMAZ/HAZ material has undergone static recrystallization and exhibits annealing (cube) texture. On the right hand side, the base material shows the typical rolling texture of fcc materials. (Saukkonen et al. 2008)

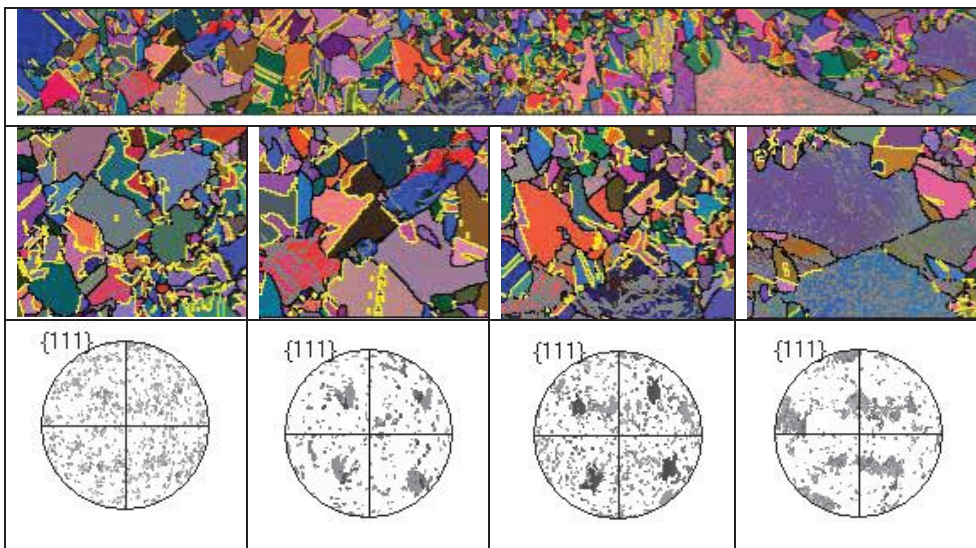


**Figure 52. EBSD images (Euler maps and pole figures) showing the transition across the boundary of the dynamically recrystallized zone in a FSW weld of cold-rolled Cu-OF. The weld nugget is on the left and the HAZ is on the right. Texture changes from almost random to cube to rolling texture can be seen in the pole figures. In the upper part of the image the same area is seen as a continuous orientation image. The twin boundaries are highlighted with yellow. The area of the separate images in the middle of the picture is 366x288  $\mu\text{m}$ . (Saukkonen et al. 2008)**

### 10.1.4 Precipitates

Precipitates of 50 mm thick Cu-OF FSW welds were studied. It was noticed that during FSW, dissolution of certain precipitates, e.g.  $\text{Cu}_2\text{S}$ , into solid solution of copper occurred. Figure 53 shows a macroscopic image of the transverse cross-section of the FSW weld

with sharp contrasts between the zones. The locations of EBSD studies are marked with boxes and letters. (Saukkonen et al. 2008)

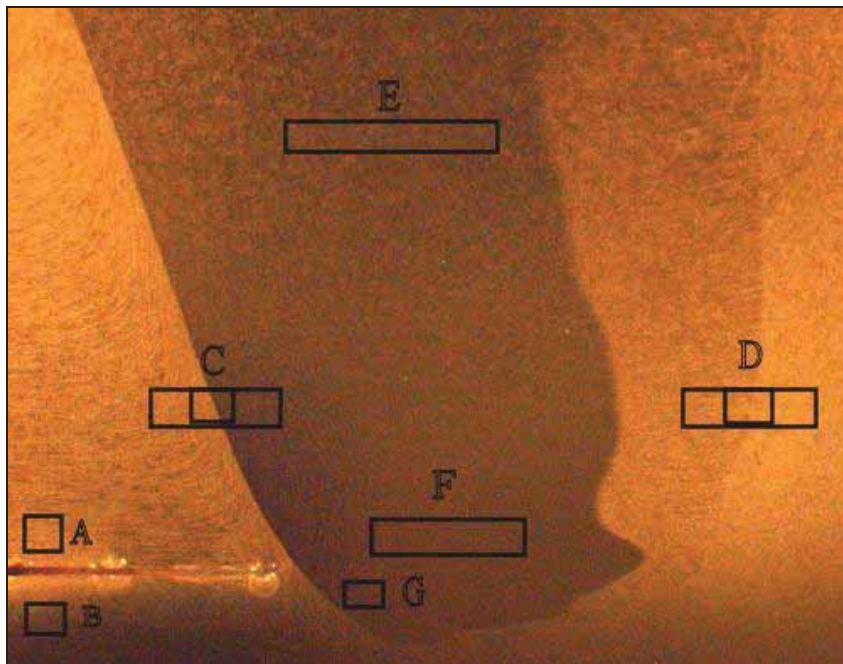


**Figure 53. Transverse cross-section of the lower part of a 50 mm thick copper FSW weld showing different zones of the weld. Boxes and letters mark the areas studied by EBSD. (Saukkonen et al. 2008)**

Figures 54 and 55 show the origin of the sharp contrast differences in Figure 53 at location C between the weld and the base material. The contrast is caused by the dissolution of  $\text{Cu}_2\text{S}$  precipitates during FSW and their subsequent precipitation in a much finer form during cooling. EDS spectrum in Figure 56 shows that the particles consist of copper and sulphur. The solubility of sulphur in copper increases rapidly at temperatures above 800 °C, which is consistent with the dissolution of  $\text{Cu}_2\text{S}$  precipitates in the temperature range of copper FSW, 800-900 °C. Insert in the bottom left corner in Figure 54 shows  $\text{Cu}_2\text{S}$  precipitates of the base material and their “tail” in greater detail. The “tails” are assumed to be an artefact caused by the fast flow of the electrolyte during electrolytic polishing. (Saukkonen et al. 2008)



Figure 54. SEM image showing the origin of the contrast in the FSW weld marked by C in Figure 53. Weld is on the right and base material on the left. EDS study revealed that the features on the left are  $\text{Cu}_2\text{S}$ . The insert shows  $\text{Cu}_2\text{S}$  precipitates of the base material and their “tail” in greater detail (Saukkonen et al. 2008)

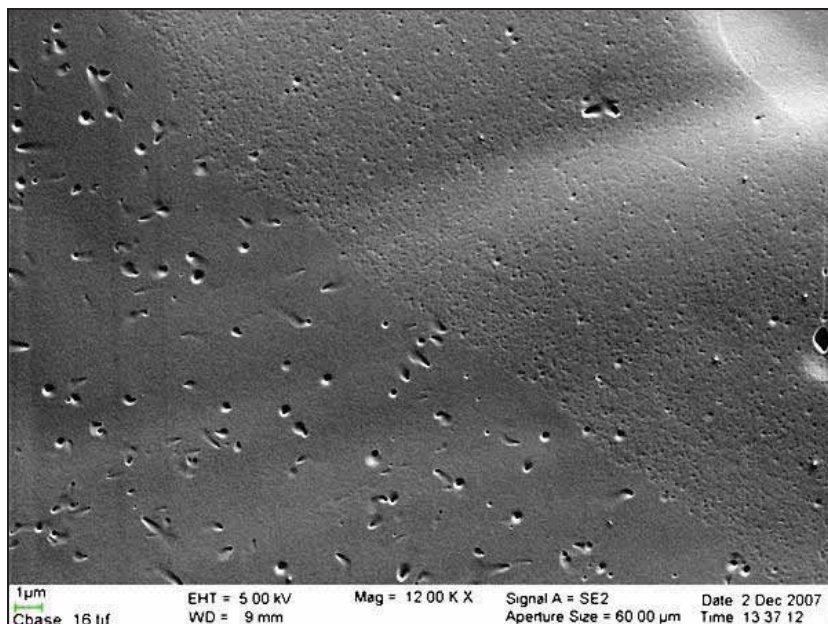
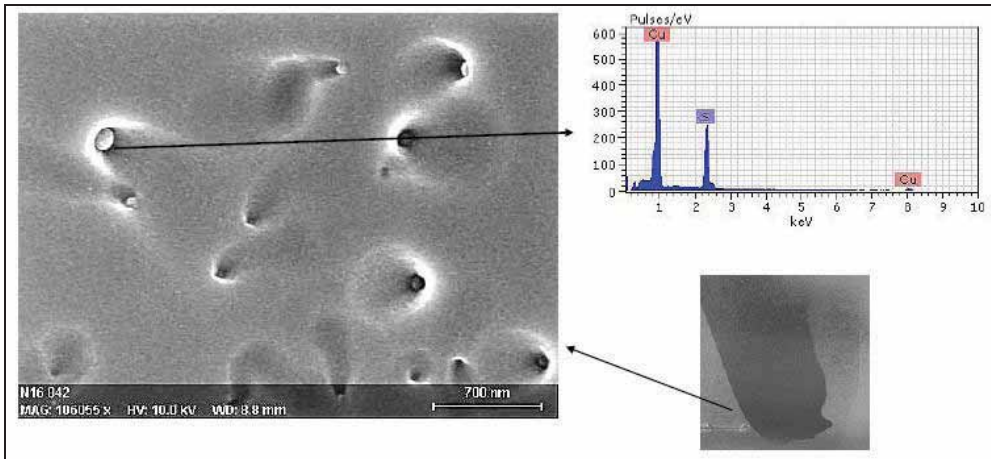


Figure 55. SEM image showing in greater detail the same location of the FSW weld as in Figure 54. Base material with its coarser  $\text{Cu}_2\text{S}$  precipitates is on the left and FSW weld with the finer precipitates is on the right.



**Figure 56.** EDS spectrum shows that the particles seen in the FEG-SEM image contain copper and sulphur.

## 10.2 Banding

A defect-free 6 mm thick Cu-OF bead-on-plate FSW weld was studied using EBSD. The weld was “cold” with a clearly visible banding. Figures 57-59 show EBSD maps of the banding in transverse, longitudinal, and horizontal cross-sections, respectively. The maps provide a 3-dimensional illustration of the bands. In each cross-sectional view the first map (on the left) is the pattern quality map with superimposed grain boundaries. The second map (on the right) shows the local misorientations. Colour key for the local misorientation maps is shown in Figure 60. In Figure 61, a higher magnification of banding in the longitudinal cross-section is shown. Pattern quality map and local misorientation map show that local misorientations are clearly higher in the bands of smaller grains than in the bands of larger grains. Figure 62 shows a high magnification IPF map of banding in longitudinal cross-section in the Z-direction. Colour key is seen in the insert. Texture in the FSW weld is weak. (Savolainen et al. 2012a)

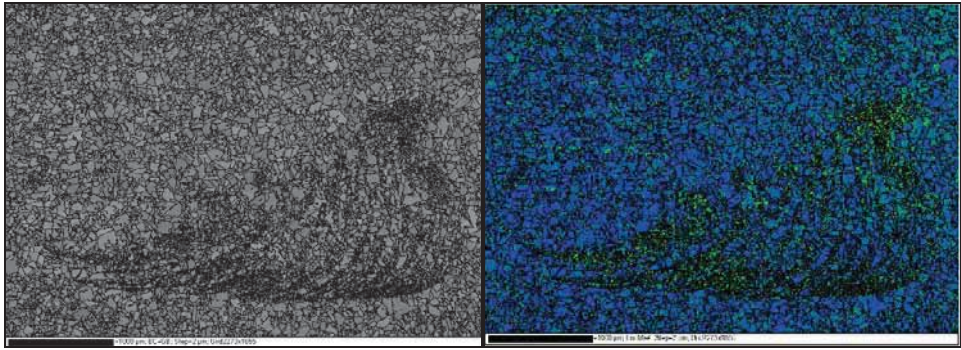


**Figure 57. EBSD maps of the transverse cross-section of banding. Pattern quality map is on the left and local misorientations map is on the right. Advancing side of the FSW weld is on the right. Length of the scale bar is 1000  $\mu\text{m}$ . The colour key for the local misorientations map is given in Figure 60. (Savolainen et al. 2012a)**

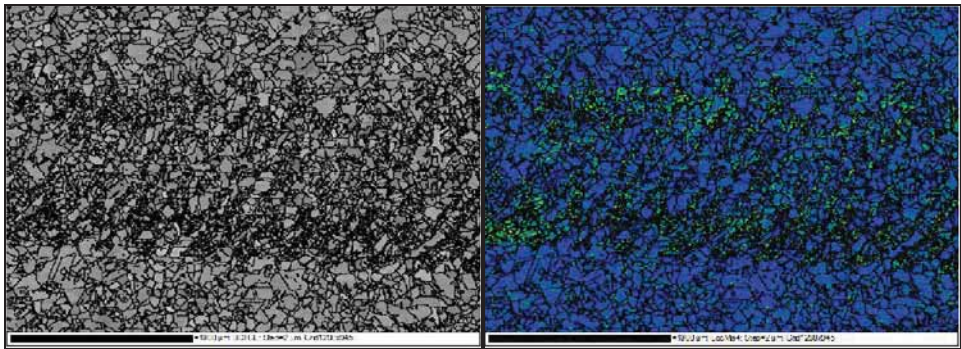


**Figure 58. EBSD maps of the longitudinal cross-section of banding at approximately the centre of the weld, slightly on the retreating side. Pattern quality map is on the left and local misorientations map is on the right. Welding direction is from right to left. Local misorientations are higher in the smaller grains. Length of the scale bar is 1000  $\mu\text{m}$ . The colour key for the local misorientations map is given in Figure 60. (Savolainen et al. 2012a)**

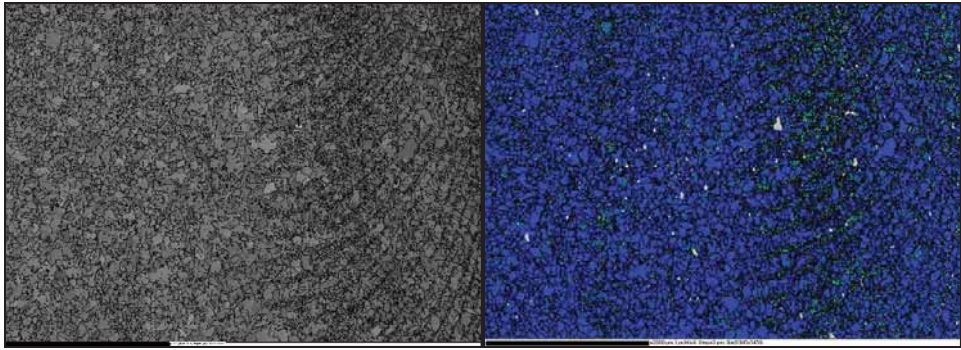


Figure 59. EBSD maps of the horizontal cross-section of banding at the depth of approximately 1 mm. Pattern quality map is on the left and local misorientations map is on the right. Advancing side is on the right. Length of the scale bar is 1000  $\mu\text{m}$ . The colour key for the local misorientations map is given in Figure 60. (Savolainen et al. 2012a)

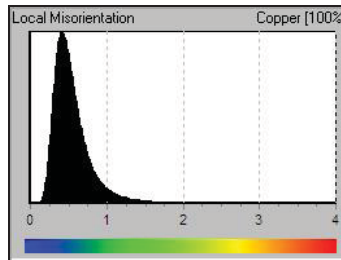


Figure 60. Colour key for the local misorientations maps in Figures 57-59 and Figure 61. (Savolainen et al. 2012a)

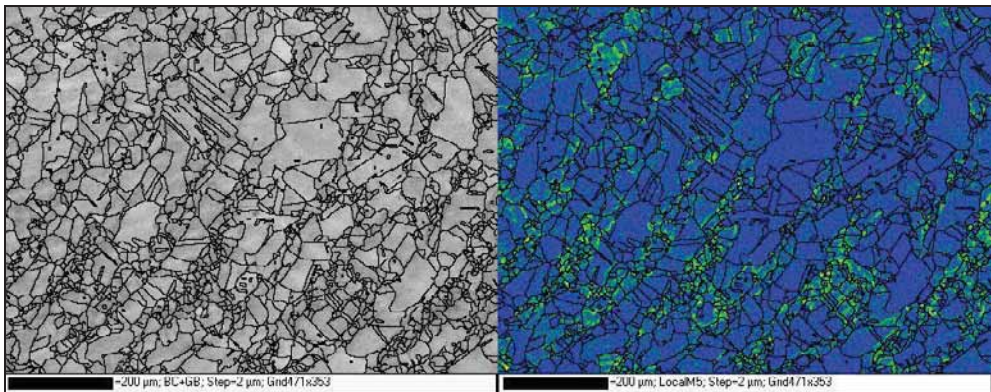
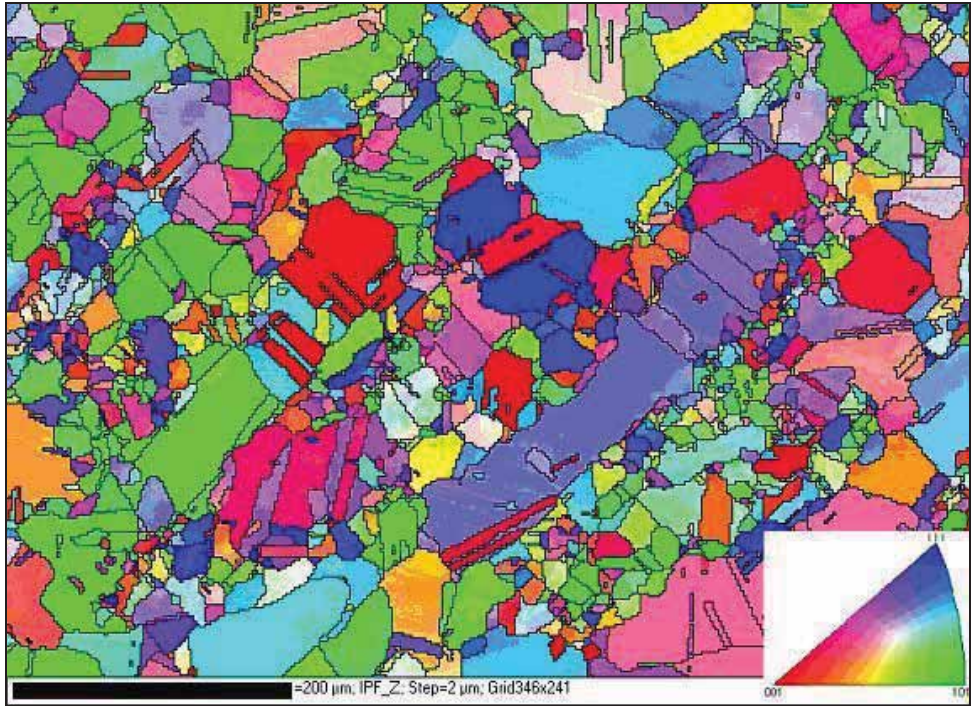
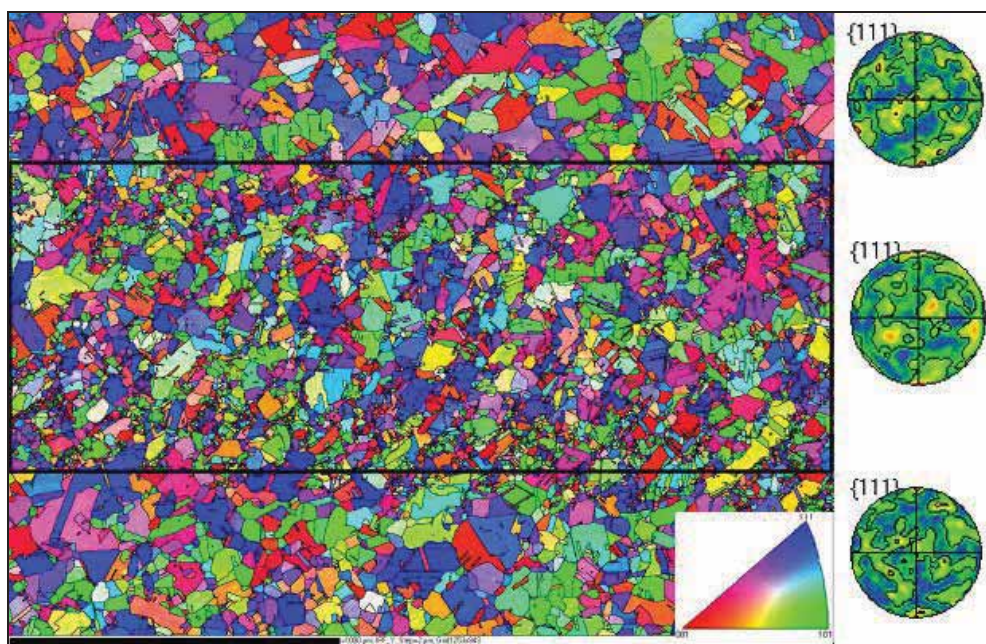


Figure 61. EBSD maps with a higher magnification of the area in the longitudinal cross-section of the Cu-OF FSW weld showing banding. The welding direction is from right to left. The surface of the weld is towards the top of the image. Pattern quality map is on the left and local misorientations map is on the right. Length of the scale bar is 200  $\mu\text{m}$ . The colour key for the local misorientations map is given in Figure 60. (Savolainen et al. 2012a)



**Figure 62. IPF map of banding in a Cu-OF FSW weld in the longitudinal cross-section in the Z-direction. Colour key is shown in the insert. (Savolainen et al. 2012a)**

Figure 63 shows an IPF map of the longitudinal cross-section of a cold FSW weld with banding shown in Figures 57-59. The map is divided into three regions, the area of distinct banding in the centre of the image and the areas above and below it. The areas are separated by black lines. The calculated  $\{111\}$  pole figures of each area are shown next to the corresponding areas. It can be seen from the IPF map that the colouring is almost random also in the areas of distinct banding shown more clearly in Figure 58. The calculated strength values of the  $\{111\}$  pole figures from the top, middle, and bottom regions are 2.3, 2.1, and 2.3 times random, respectively, indicating weak texture. (Savolainen et al. 2012a)



**Figure 63.** Inverse pole figure map showing the longitudinal cross-section of the Cu-OF FSW weld with banding (same weld as in Figure 58). The  $\{111\}$  pole figures calculated from the top, middle, and bottom regions of the image separated by black lines are shown on the right. The strength values of the texture in pole figures are 2.3, 2.1 and 2.3 times random, respectively. The colour key of the IPF map is shown in the insert. (Savolainen et al. 2012a)

### 10.3 Cu/Al Dissimilar Metal FSW

FSW of dissimilar metal joints between copper and aluminium as well as the properties of the welds were studied. The varied welding parameters were tool rotation and traverse speeds (beginning with values which produced good welds in Cu-OF), the sideways (Y-axis) position of the tool (in the centre of the weld line, on copper side, or on aluminium side), the rotation direction (should the stronger material be on the advancing or on the retreating side of the weld), and the tool tilt angle. First the effect of rotation direction was studied with three different combinations of tool rotation and traverse speeds. Then the effect of the probe location was studied using the better rotation direction and the same rotation and traverse speeds as before. The effect of varying the tilt angle was also tested. Finally, the rotation and traverse speed combinations were optimised. The studied welding parameter combinations and the transverse microsections of the samples are presented in Table 7. (Savolainen et al. 2005)

**Table 7. The studied welding parameter combinations and the transverse sections of the Cu/Al dissimilar metal FSW welds (Savolainen et al. 2005).**

Weld	Rotation Speed (rpm)	Traverse Speed (mm/min)	Tilt (°)	Plunge Depth (mm)	Material on Advancing Side	Tool Displacement	Transverse Microsection
14A	1000	100	2.5	6.0	Aluminium	None	-
14B	1000	50	2.5	6.0	Aluminium	None	-
14C	1000	100	2.5	5.8	Aluminium	None	-
14D	1000	100	2.5	5.7	Copper	None	
15A	1000	100	2.5	5.7	Copper	2 mm in Cu	
15B	1000	100	2.5	5.7	Aluminium	2 mm in Cu	-
15C	1000	100	2.5	5.7	Copper	2 mm in Al	
15D	1000	100	2.5	5.7	Aluminium	2 mm in Al	
19A	1250	100	2.5	5.5	Copper	None	-
19B	1250	100	2.5	5.5	Aluminium	2 mm in Al	-
19C	1250	100	2.5	5.5	Copper	2 mm in Cu	
19D	750	100	2.5	5.6	Copper	None	
19E	750	100	2.5	5.6	Aluminium	1.5 mm in Al	-
19F	750	100	2.5	5.6	Copper	1.5 mm in Cu	
19G	1000	100	1.5	5.6	Copper	None	-
19H	750	100	1.5	5.7	Copper	1.5 mm in Cu	-
19J	750	150	2.5	5.6	Copper	1.5 mm in Cu	
20A	750	150	2.5	5.6	Copper	1 mm in Cu	
20B	750	150	2.5	5.6	Copper	0.5 mm in Cu	-
20C	750	200	2.5	5.6	Copper	1.5 mm in Cu	-
21A	1000	200	2.5	5.6	Copper	1.5 mm in Cu	
21B	1250	250	2.5	5.6	Copper	1.5 mm in Cu	
25A+B	750	150	2.5	5.6+5.7	Copper	1.5 mm in Cu	
27A+B	750	100	2.5	5.6+5.7	Copper	1.5 mm in Cu	
27C	750	100	2.5	5.6	Copper	1.5 mm in Cu	-
27D	750	150	2.5	5.6	Copper	1.5 mm in Cu	-

Figures 64-66 show examples of the appearance of good and poor quality Cu/Al dissimilar metal FSW welds. In Figure 64 copper was on the advancing side and the tool displacement was on the copper side. In Figures 65 and 66 aluminium was on the

advancing side and tool displacement was either on the aluminium side (Figure 66) or there was no tool displacement (Figure 65).

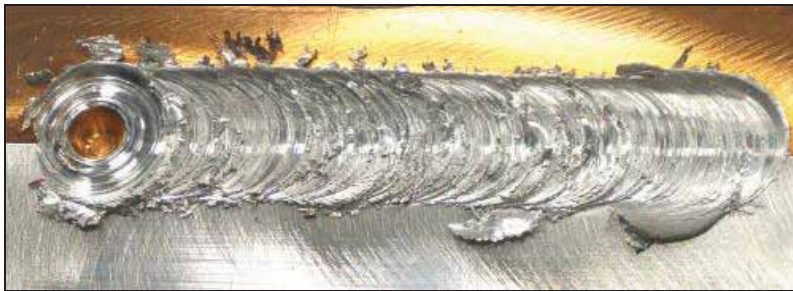


**Figure 64.** An example of a good quality Cu/Al dissimilar metal FSW weld, 2004-10-19J (in Table 7). Copper was on the advancing side of the weld. Tool displacement was 1.5 mm on the copper side. Welding parameters were 750 rpm and 150 mm/min.



**Figure 65.** An example of a poor quality Cu/Al dissimilar metal FSW weld, 2004-10-14A (in Table 7). Aluminium was on the advancing side, no tool displacement. Welding parameters were 1000 rpm and 100 mm/min. No proper joint was formed between the plates.



**Figure 66.** An example of a poor quality Cu/Al dissimilar metal FSW weld, 2004-10-19E (in Table 7). Tool displacement was 1.5 mm on the aluminium side. Aluminium was on the advancing side. Welding parameters were 750 rpm and 100 mm/min. It is noteworthy that with the same welding parameters, a good weld is produced when copper is on the advancing side. With aluminium on the advancing side, a large groove is formed on the aluminium side.

### 10.3.1 Tensile Tests

Transverse tensile tests were performed for one-sided and double-sided Cu/Al dissimilar metal FSW welds of two different welding parameter combinations, 750 rpm / 100 mm/min and 750 rpm / 150 mm/min. Figure 67 shows the measured stress-strain curves. (Savolainen et al. 2005)

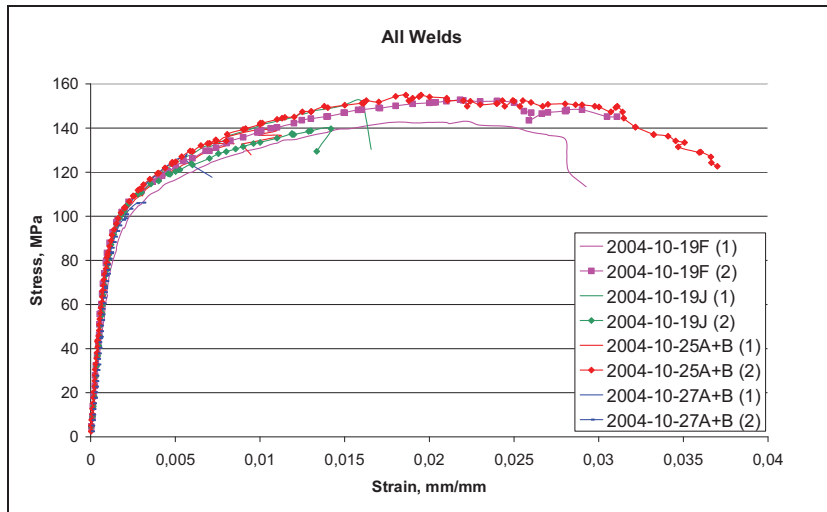


**Figure 67. Transverse tensile test results of the Cu/Al dissimilar metal FSW welds. The welding parameters are given in Table 7. (Savolainen et al. 2005)**

### 10.3.2 Hardness Profiles

Hardness was measured horizontally at the distance of 2 mm from the weld surfaces and vertically from the centre line of the Cu/Al dissimilar metal FSW weld nugget. Figure 68 shows the horizontal hardness profiles of the one-sided Cu/Al dissimilar metal FSW welds. In the vertical hardness profile through the weld nugget (weld 2004-10-27A+B), the hardness varied between 50 HV and 220 HV. Microhardness measurements show that the hardness of the  $\text{Al}_2\text{Cu}$ -phase is 425-470 HV 50g and the hardness of the AlCu-phase is 650-700 HV 50g. (Savolainen et al. 2005)

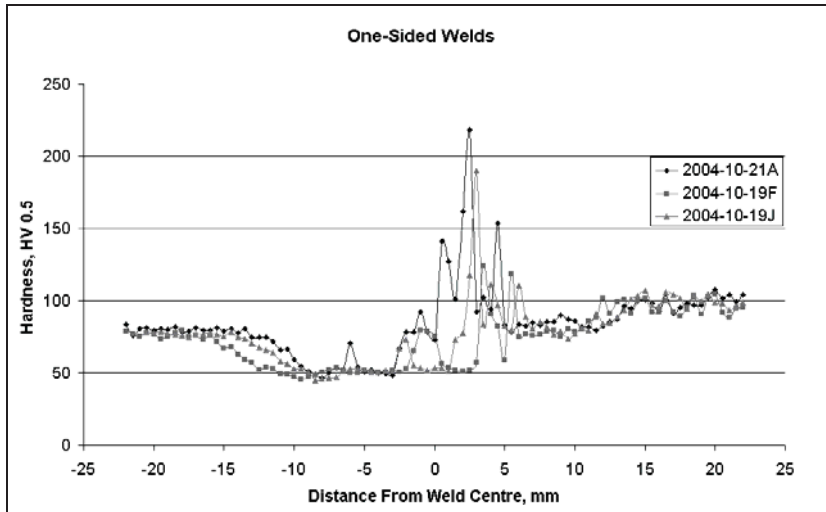


**Figure 68. Horizontal hardness profiles of the one-sided Cu/Al dissimilar metal FSW welds. Aluminium is on the left and copper on the right. The rotation and traverse speed values (rpm / mm/min) of 2004-10-21A, 2004-10-19F, and 2004-10-19J were 1000/200, 750/100, and 750/150, respectively. Other welding characteristics are given in Table 7. (Savolainen et al. 2005)**

### 10.3.3 Electrical Resistivity

The electrical resistivity of the Cu/Al dissimilar metal FSW welds was studied. The electrical resistivity measurement results (Table 8) were used to calculate first the specimen resistivity by normalising the results with taking into account the different cross-sectional areas of the specimens. The results show that the resistivity of the welded joint (29 nΩm) is 2.5 % higher than the average resistivity of both base materials (28.3 nΩm). The additional resistance resulting from welded joint was calculated by using the base material resistances and the welded sample resistances (Table 9). The calculated resistance value of the joint, 0.4 μΩ, corresponds to the resistance of 3.1 mm long copper bar or 1.8 mm long aluminium bar with the same cross-sectional area. (Savolainen et al. 2005)

**Table 8. Electrical resistivity measurement results for copper and aluminium base materials and two Cu/Al dissimilar metal FSW joints (Savolainen et al. 2005).**

Specimen	Cross-section area mm <sup>2</sup>	Resistance μΩ	Resistivity nΩm
Cu	201	10.1	20.5
Al	199	17.9	36.1
Cu/Al joint 10-25-A+B	160	17.9	28.9
Cu/Al joint 10-27-A+B	159	18.0	29.0

**Table 9. Results of the electrical conductivity tests (Savolainen et al. 2005).**

Specimen	Total resistance $\mu\Omega$	Cu Resistance $\mu\Omega$	Al Resistance $\mu\Omega$	Joint resistance $\mu\Omega$
Cu/Al joint 10-25-A+B	17.9	6.33	11.2	0.395
Cu/Al joint 10-27-A+B	18.0	6.36	11.2	0.433

#### 10.3.4 Intermetallic Compounds

Macroscopic images of the structures just below the surface of the weld are presented in Figures 69 and 70. The different joint zones (pure copper, pure aluminium, and their mixture) can be seen in the pictures. They show the form of mixing of copper and aluminium.

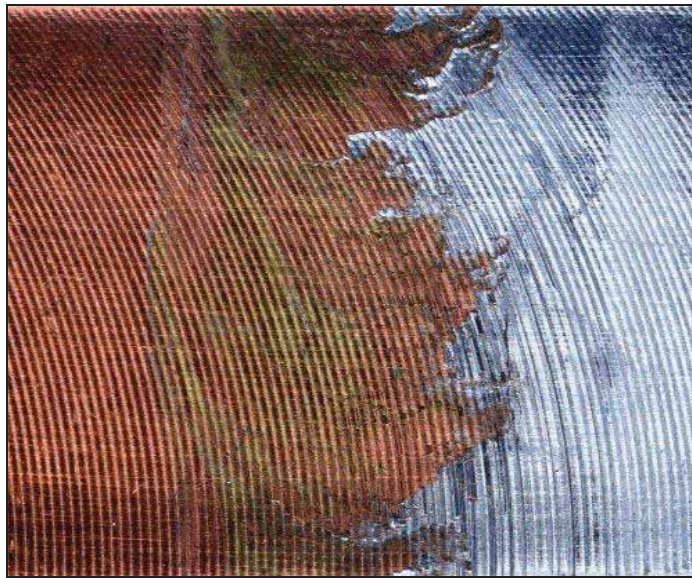


**Figure 69. The Cu/Al dissimilar metal FSW weld 2004-10-25A (Table 7). Welding parameters were 750 rpm and 100 mm/min.**



**Figure 70. The Cu/Al dissimilar metal FSW weld 2004-10-27A (Table 7). Welding parameters were 750 rpm and 150 mm/min.**

Transverse macrosections as well as the tensile test specimens of the Cu/Al dissimilar metal FSW welds were studied using SEM. In backscattered electron (BSE) SEM images the contrast is formed by differences in atomic weight; aluminium is shown as the darker phase and copper as the lighter phase. There was a thin, pale grey layer on the fracture surfaces of the Cu/Al dissimilar metal FSW welds. A BSE image of the cross-section of the nickel-plated fracture surface of a tensile test specimen is shown in Figure 71. A BSE image of the transverse microsection of a Cu/Al dissimilar metal FSW weld revealing various zones of copper, aluminium, and their combinations is shown in Figure 72. (Savolainen et al. 2005)

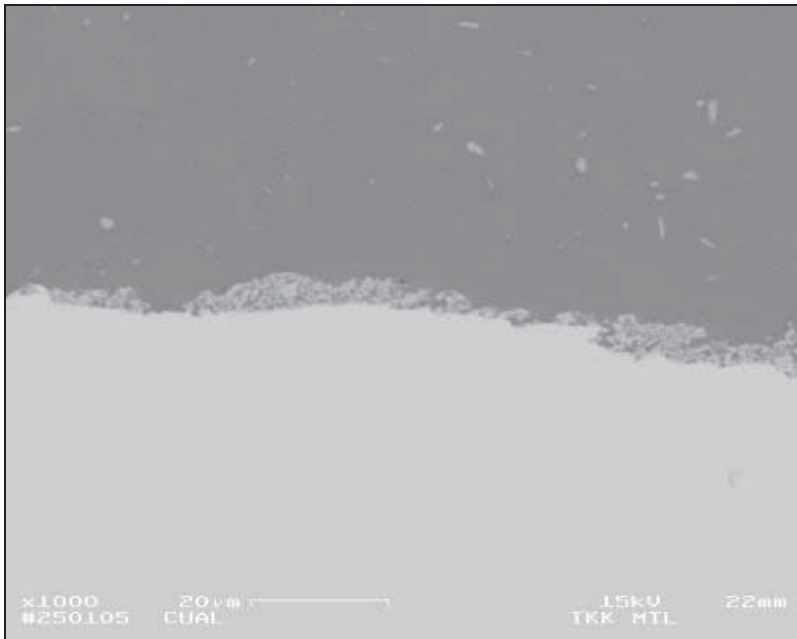


**Figure 71.** A BSE image of the thin discontinuous layer on the fracture surface of a Cu/Al dissimilar metal FSW weld. Aluminium is on the top and nickel-plating on the bottom.

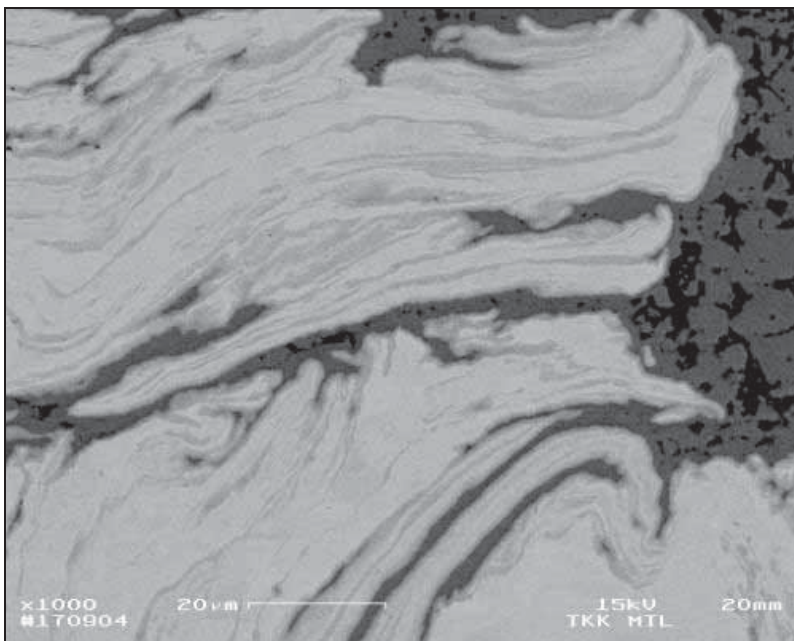


**Figure 72.** A BSE image of a Cu/Al dissimilar metal FSW weld cross-section. Multiple phases in the weld are clearly visible. Copper-rich phases are seen as lighter and aluminium-rich phases as darker fields in the figure. (Savolainen et al. 2005)

Figure 73 shows a BSE image of the intermetallic compounds in the weld nugget. According to EBSD, the two phases are identified as  $\text{Al}_2\text{Cu}$  (darker phase) and  $\text{AlCu}$  (lighter phase). During FSW the intermetallic phases are dispersed (Figure 74). The brittle intermetallic regions contain cracks which are stopped by ductile aluminium at the interface.

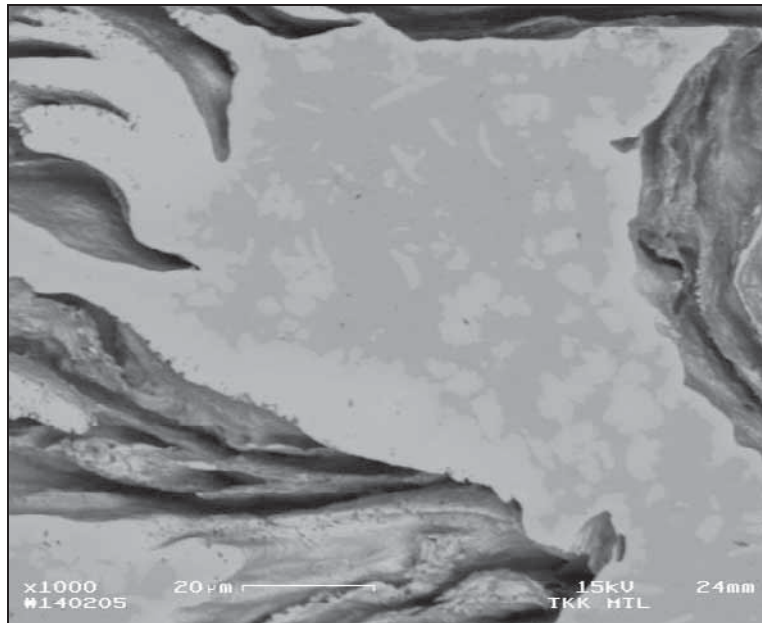


**Figure 73. A BSE image of the intermetallic compounds in the weld nugget of a Cu/Al dissimilar metal FSW weld. The darker phase is identified as  $\text{Al}_2\text{Cu}$  and the lighter phase as  $\text{AlCu}$  by EBSD. The darkest regions at the edges of the image are formed by topographical contrast due to etching during electrolytical polishing.**

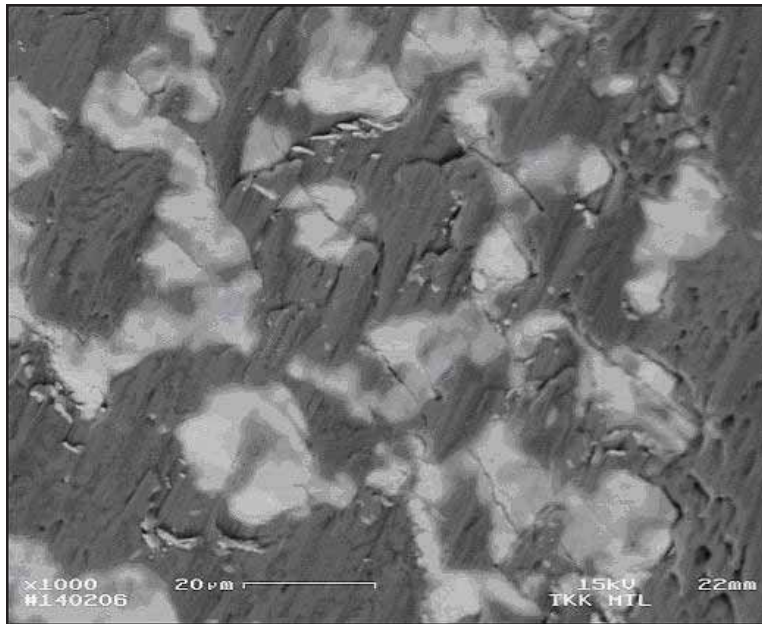


**Figure 74. A BSE image showing the fracture surface of a Cu/Al dissimilar metal FSW weld. Cracks in the brittle IMC (light grey) phase are stopped by the ductile aluminium (dark grey) phase at the interface.**

#### **10.4 Entrapped Oxide Particles**

The origin, avoidance, and effect of entrapped oxide particles in copper FSW welds were studied.

##### 10.4.1 Origin of Entrapped Oxide Particles

The origin and formation of entrapped oxide particle lines were studied using Cu-OFP samples with very narrow electro-discharge machined grooves of varying depth (0, 2, 5, and 8 mm). The grooves were located at the centre line of the weld. The four bead-on-plate welds on grooved samples were made using the same welding parameters but different joint preparation and shielding gas combinations. The studied joint preparation and shielding gas combinations were as follows: 1: no oxide removal and no shielding gas, 2: oxide removal and no shielding gas, 3: no oxide removal and using shielding gas, and 4: oxide removal and using shielding gas. The samples were FSW welded using a tool with a 5.5 mm long tool probe. Figures 75-78 show the formation of the entrapped oxide particle line. The entrapped oxide particle lines originate from the butting surfaces. The deeper the

original groove, the longer the line of entrapped oxide particles. In Figure 78, where the groove is deeper than the tool probe length, a part of the groove remains un-welded. (Savolainen et al. 2008)



**Figure 75. Sample with no groove (Savolainen et al. 2008).**



**Figure 76. Sample with a 2 mm deep groove (Savolainen et al. 2008).**



**Figure 77. Sample with a 5 mm deep groove (Savolainen et al. 2008).**



**Figure 78. Sample with an 8 mm deep groove (Savolainen et al. 2008).**

The development of the typical S-shaped feature of the line of the entrapped oxide particles can be seen in Table 10, especially in samples 2A-2D (enlarged in Figures 75-78). In sample 2A there was no groove and there is no evidence of entrapped oxide particles. In sample 2B, there was a 2 mm deep groove, and a short entrapped oxide particle line can be seen at the top of the weld. In sample 2C, there was a 5 mm deep groove, and entrapped oxide particle line encompasses almost the entire weld depth. In sample 2D, there was an 8 mm deep groove, and in addition to the entrapped oxide particle line, also the unaffected

remnants of the original groove can be seen (vertical section of the entrapped oxide particle line). (Savolainen et al. 2008)

**Table 10. Macroscopic images of the bead-on-plate FSW welded, grooved Cu-OFP samples with different groove depths and different joint preparation and shielding gas combinations. The images are not in the same scale in relation to each other. (Savolainen et al. 2008)**

	A: 0 mm	B: 2 mm	C: 5 mm	D: 8 mm
1: No oxide removal, no shielding gas				
2: Oxide removal, no shielding gas				
3: No oxide removal, shielding gas				
4: Oxide removal, shielding gas				

#### 10.4.2 Avoidance of Entrapped Oxide Particles

Figures 79-82 show details of the bead-on-plate friction stir welded grooved Cu-OFP samples (upmost curve of the entrapped oxide particle line). The samples were hydrogen annealed at 850 °C for 30 min in N<sub>2</sub> + 10 % H<sub>2</sub> gas. The results show the effect of the different studied combinations of oxide removal prior to welding (using 50/50% nitric acid/distilled water) and shielding gas during welding. The sample in Figure 79 was the reference, welded without oxide removal or shielding gas. The sample in Figure 80 was welded after oxide removal, but without shielding gas. Figure 81 shows the sample welded using shielding gas, but with no prior oxide removal. The sample with both oxide removal prior to welding and using shielding gas during welding is shown in Figure 82. (Savolainen et al. 2008)

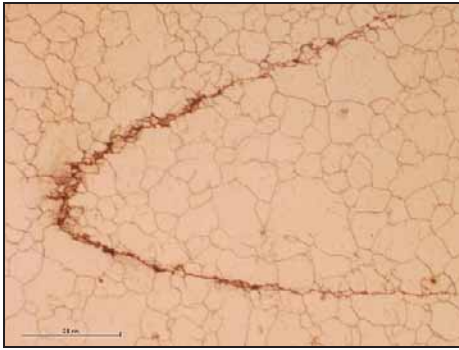


**Figure 79. Detail of hydrogen annealed reference sample FSW welded with no oxide removal or shielding gas. Length of the scale bar is 0.5 mm. (Savolainen et al. 2008)**

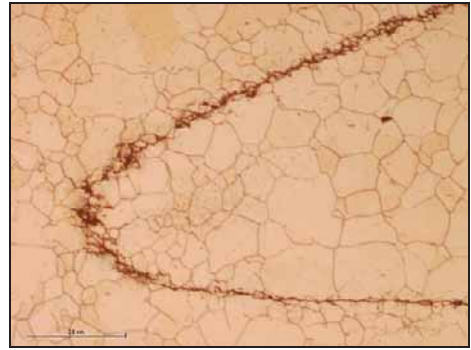


**Figure 80. Detail of hydrogen annealed sample FSW welded with oxide removal and no shielding gas. Length of the scale bar is 0.5 mm. (Savolainen et al. 2008)**

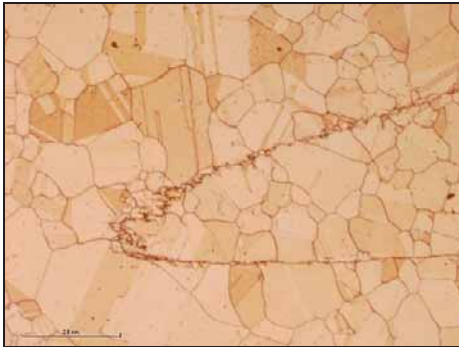


**Figure 81. Detail of hydrogen annealed sample FSW welded with no oxide removal and with shielding gas. Length of the scale bar is 0.5 mm. (Savolainen et al. 2008)**



**Figure 82. Detail of hydrogen annealed sample FSW welded with oxide removal and shielding gas. Length of the scale bar is 0.5 mm. (Savolainen et al. 2008)**

The hydrogen annealed samples 1DV and 2DV contained voids and signs of deformation visible at the region of entrapped oxide particles (Figures 83 and 84). The hydrogen annealed samples 3DV and 4DV showed no voids, only signs of deformation (Figures 85 and 86). The voids indicate the existence of a relatively high amount of entrapped oxide particles in the weld whereas the existence of deformation indicates some reaction between the hydrogen and oxide particles in the welds. (Savolainen et al. 2008)

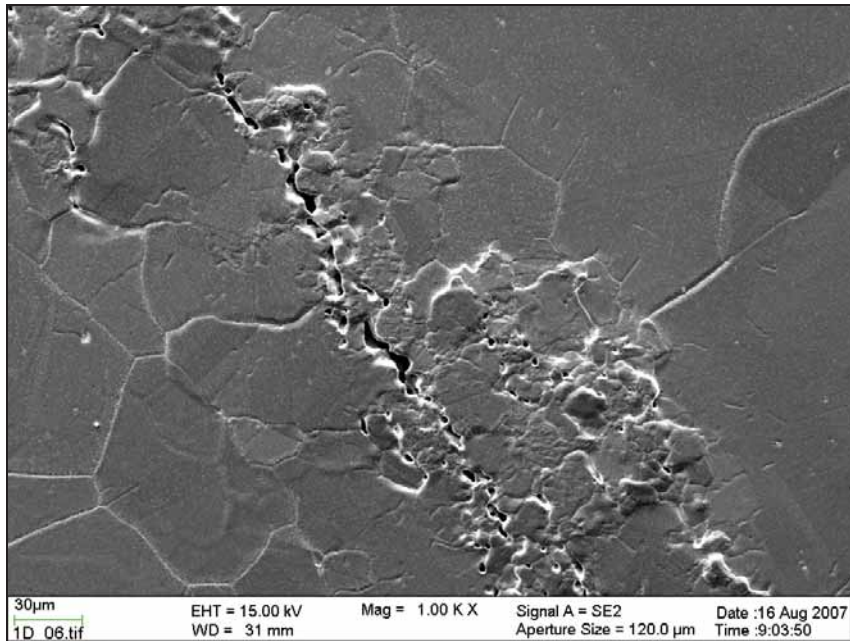


**Figure 83.** SEM image of hydrogen annealed reference sample (1D) FSW welded with no oxide removal prior to welding or use of shielding gas. Voids and plastic deformation are clearly visible in the region of the entrapped oxide particles. (Savolainen et al. 2008)

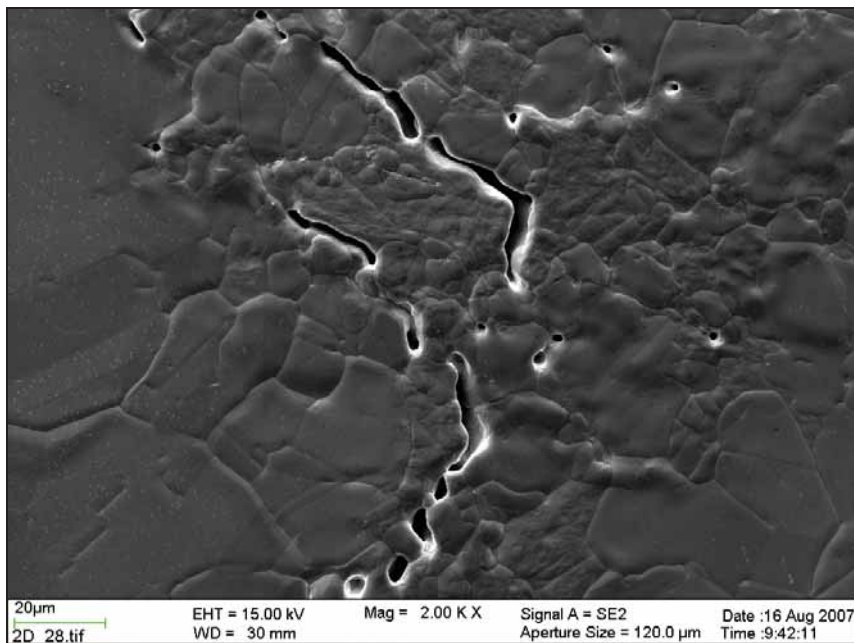


**Figure 84.** SEM image of hydrogen annealed sample (2D) FSW welded with oxide removal and no shielding gas. Voids and deformation are clearly visible at the region of entrapped oxide particles. (Savolainen et al. 2008)

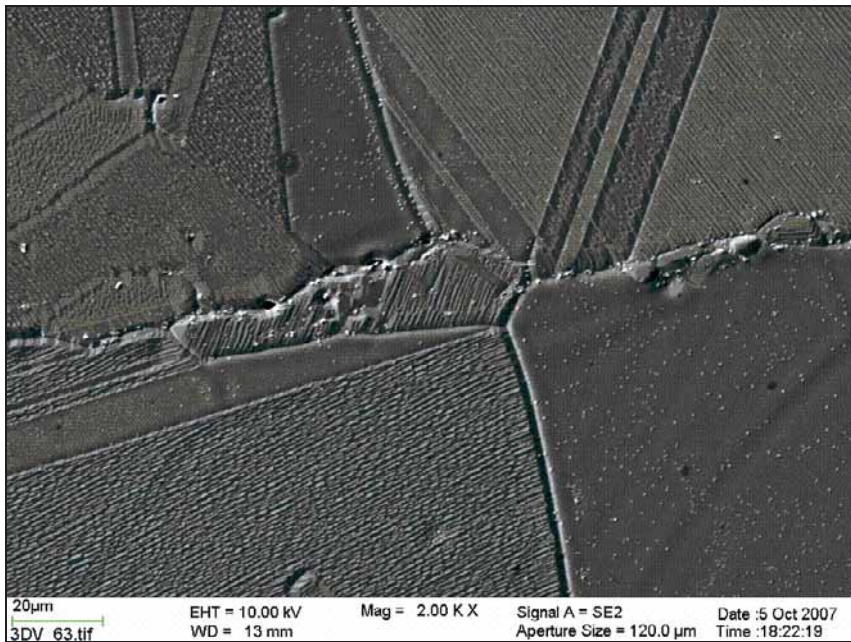


Figure 85. SEM image of hydrogen annealed sample 3D FSW welded with no oxide removal and with shielding gas. Some voids are visible, but there are signs of deformation at the region of entrapped oxide particles. (Savolainen et al. 2008)

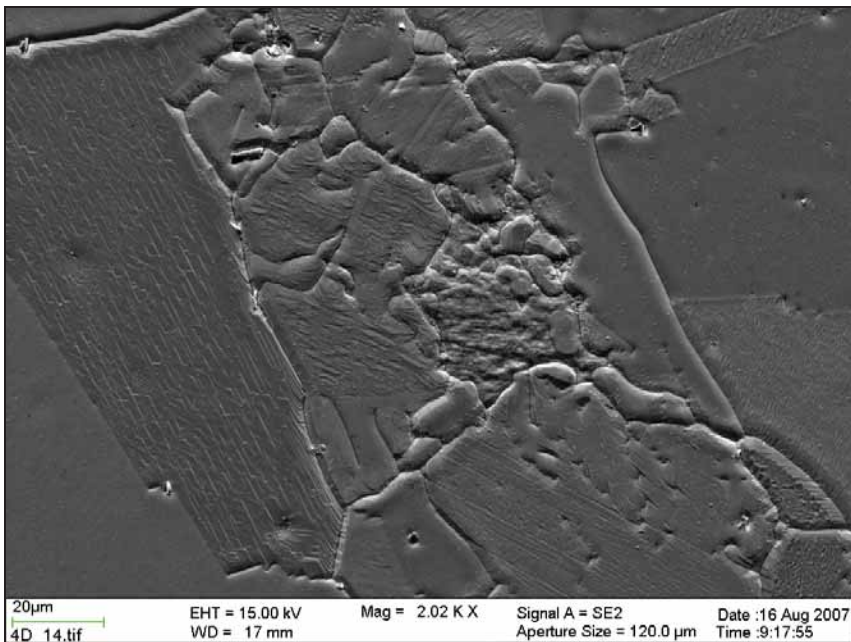
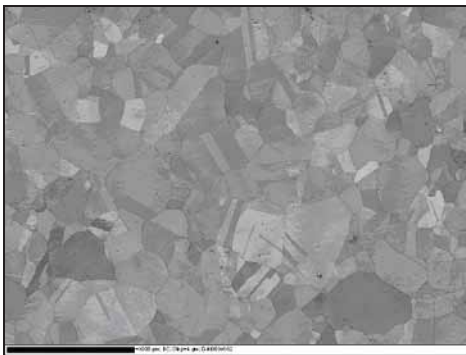


Figure 86. SEM image of hydrogen annealed sample 4D FSW welded with both oxide removal and shielding gas. No voids are visible, but the region of entrapped oxide particles shows signs of deformation. (Savolainen et al. 2008)

Four different EBSD maps were run from the base material and from the upmost curve of the entrapped oxide particle line of the Cu-OFP FSW welds (Figures 87-106). The maps are defined as follows: 1: Pattern quality, 2: Grain boundaries. Both band contrast and grain boundaries (misorientation angle  $10^\circ$ , no small angle boundaries), 3: Euler angles. Twin boundaries fulfil Brandon criterion, and 4: Recrystallized fraction. The minimum angle for subgrain determination was  $2^\circ$ . (Savolainen et al. 2008)

Figures 88-90 show the EBSD maps of the base material. It can be seen that the base material has a large, non-homogeneous grain size. The average grain size is about  $180\ \mu\text{m}$ . The base material was hot rolled and consequently in recrystallized condition. Annealing twins can be seen everywhere in the base material (Figure 89). (Savolainen et al. 2008)



**Figure 87. EBSD pattern quality map of the base material. Length of the scale bar is  $1000\ \mu\text{m}$ . (Savolainen et al. 2008)**

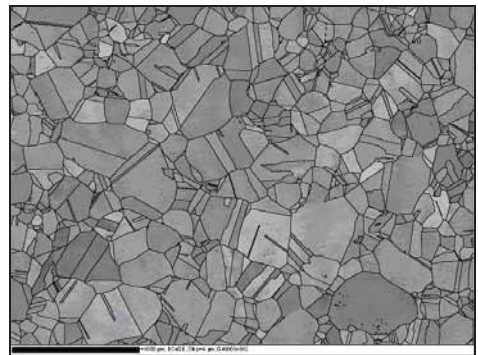


**Figure 88. EBSD pattern quality map with superimposing the grain boundaries shows that the base material has a large, non-homogeneous grain size. Length of the scale bar is  $1000\ \mu\text{m}$ . (Savolainen et al. 2008)**

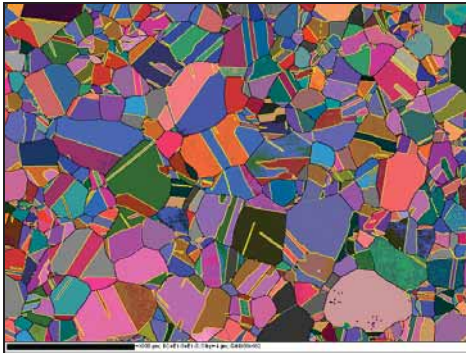


**Figure 89.** Euler map of the base material. Twin boundaries are shown as yellow. Length of the scale bar is 1000  $\mu\text{m}$ . (Savolainen et al. 2008)

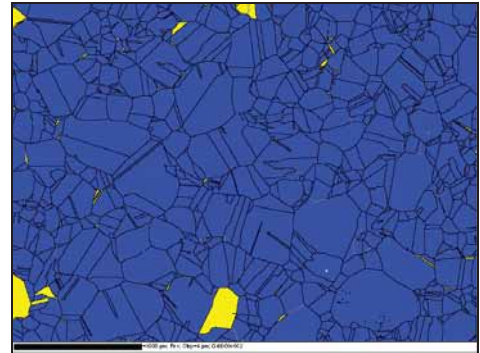


**Figure 90.** Recrystallized fraction map shows that the base material is recrystallized. Recrystallized fraction is shown in blue and substructured in yellow colour. Length of the scale bar is 1000  $\mu\text{m}$ . (Savolainen et al. 2008)

Figures 91-94 show the EBSD maps of sample 1D (8 mm groove, no oxide removal, no shielding gas, no hydrogen annealing). The entrapped oxide particle line can be seen in Figure 91 as a black semi-continuous line. The grain size is considerably smaller than in the base material, about 25  $\mu\text{m}$ . (Savolainen et al. 2008)

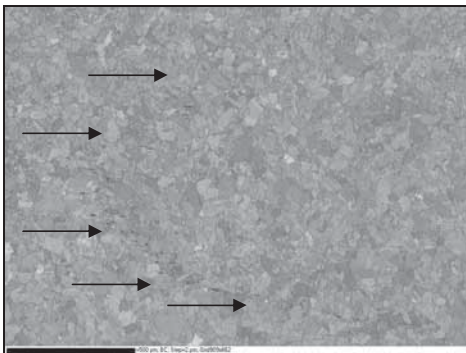


**Figure 91.** EBSD pattern quality map of the reference sample 1D FSW welded with no oxide removal or shielding gas. Location of the entrapped oxide particles can be seen as a black semi-continuous line. Length of the scale bar is 500  $\mu\text{m}$ . (Savolainen et al. 2008)

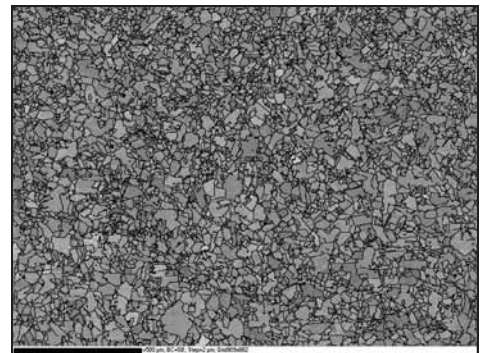


**Figure 92.** EBSD pattern quality map with superimposed grain boundaries of the reference sample 1D. The grain boundaries are seen as black. Grain size is very small. Length of the scale bar is 500  $\mu\text{m}$ . (Savolainen et al. 2008)



**Figure 93.** Euler map of the reference sample 1D. Twin boundaries are shown as yellow. Length of the scale bar is 500  $\mu\text{m}$ . (Savolainen et al. 2008)

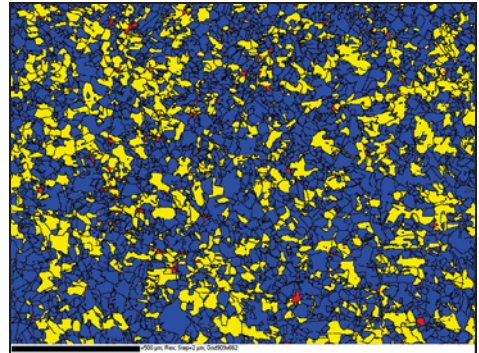


**Figure 94.** Recrystallized fraction map of the reference sample 1D. Recrystallized fraction is shown in blue, substructured in yellow, and deformed in red colour. Length of the scale bar is 500  $\mu\text{m}$ . (Savolainen et al. 2008)

Figures 95-98 show the EBSD maps of sample 1DV (8 mm groove, no oxide removal, no shielding gas, hydrogen annealed). Sample 1DV shows clearly the region of entrapped oxide particles. Grain size has remained small in that region, even though it is larger everywhere else in the sample due to grain growth. The average grain size in the studied location is about 80  $\mu\text{m}$ . (Savolainen et al. 2008)

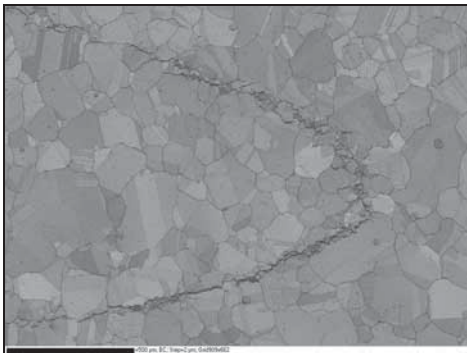


**Figure 95.** EBSD pattern quality map of hydrogen annealed reference sample 1DV FSW welded with no oxide removal or shielding gas shows clearly the region of entrapped oxide particles. Grain size is considerably larger than in the as-welded sample. Grain size is small near the entrapped oxide particles. Length of the scale bar is 500  $\mu\text{m}$ . (Savolainen et al. 2008)

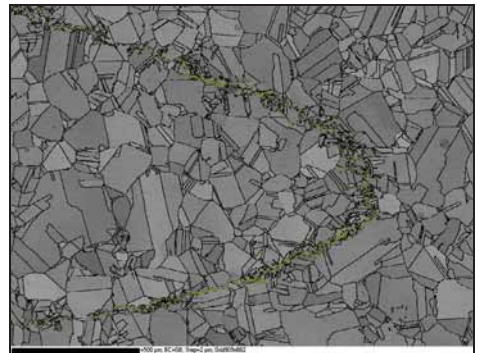


**Figure 96.** EBSD pattern quality map with superimposed grain boundaries of hydrogen annealed reference sample 1DV. Length of the scale bar is 500  $\mu\text{m}$ . (Savolainen et al. 2008)

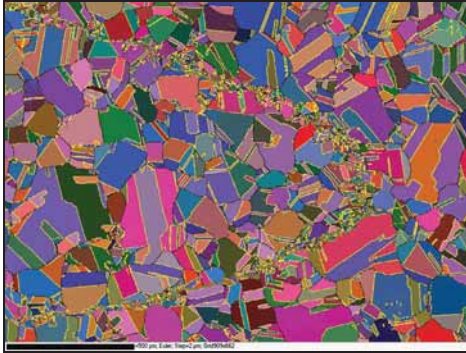


**Figure 97.** Euler map of hydrogen annealed reference sample 1DV. Twin boundaries are seen as yellow. Length of the scale bar is 500  $\mu\text{m}$ . (Savolainen et al. 2008)

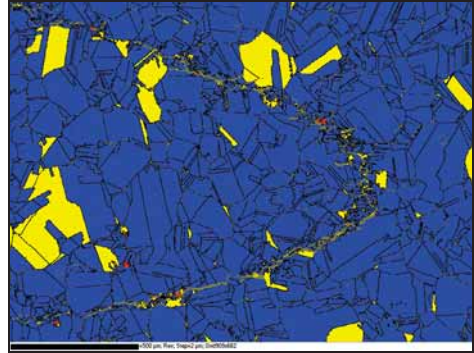


**Figure 98.** Recrystallized fraction map of hydrogen annealed reference sample 1DV. Recrystallized fraction is shown in blue, substructured in yellow, and deformed in red colour. Length of the scale bar is 500  $\mu\text{m}$ . (Savolainen et al. 2008)

Figures 99-102 show the EBSD maps of FSW welded sample 4D (8 mm groove, oxide removal, using shielding gas, no hydrogen annealing). No signs of entrapped oxide particles can be seen. The average grain size (25  $\mu\text{m}$ ) is considerably smaller than that of the base material (180  $\mu\text{m}$ ). (Savolainen et al. 2008)

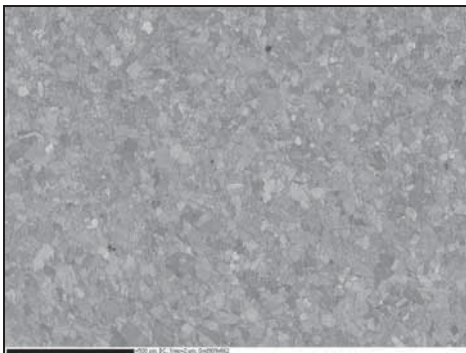


**Figure 99.** EBSD pattern quality map of sample 4D FSW welded with both oxide removal and shielding gas. No entrapped oxide particles can be seen. Length of the scale bar is 500  $\mu\text{m}$ . (Savolainen et al. 2008)

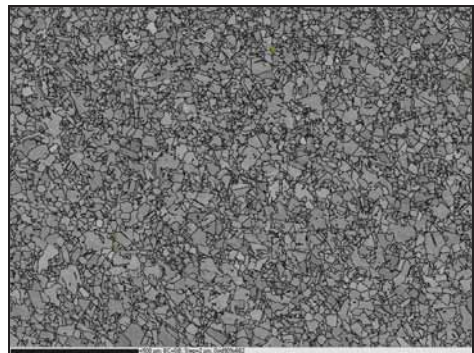


**Figure 100.** EBSD pattern quality map with superimposed grain boundaries of sample 4D. Grain size is very small. Length of the scale bar is 500  $\mu\text{m}$ . (Savolainen et al. 2008)



**Figure 101.** Euler map of sample 4D. Twin boundaries are seen as yellow. Length of the scale bar is 500  $\mu\text{m}$ . (Savolainen et al. 2008)

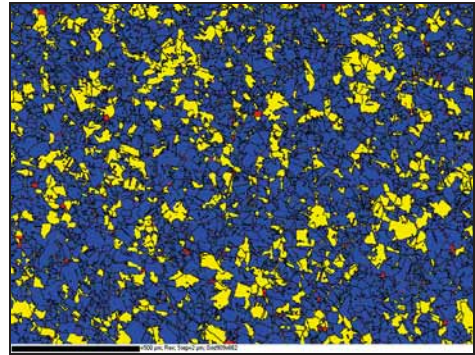


**Figure 102.** Recrystallized fraction map of sample 4D. Recrystallized fraction is shown in blue, substructured in yellow, and deformed in red colour. Length of the scale bar is 500  $\mu\text{m}$ . (Savolainen et al. 2008)

Figures 103-106 show the EBSD maps of FSW welded sample 4DV (8 mm groove, oxide removal, using shielding gas, hydrogen annealing). Sample 4DV shows minor signs of entrapped oxide particles after hydrogen annealing. The grain size has remained small near the oxide particles. The average grain size (130  $\mu\text{m}$ ) is almost double compared to that of sample 1DV (80  $\mu\text{m}$ ) even though the as-welded grain size (samples 1D and 4D) was the same. (Savolainen et al. 2008)

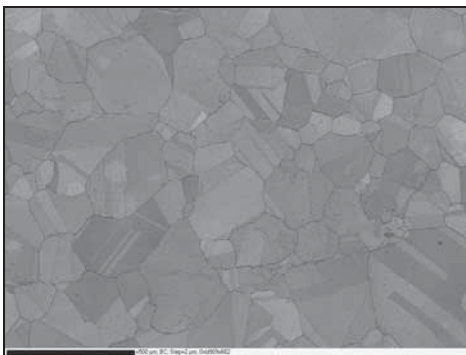


**Figure 103.** EBSD pattern quality map of hydrogen annealed sample 4DV FSW welded with both oxide removal and shielding gas. Grain size is very large compared to the as-welded sample. Entrapped oxide particles can be faintly seen. Length of the scale bar is 500  $\mu\text{m}$ . (Savolainen et al. 2008)

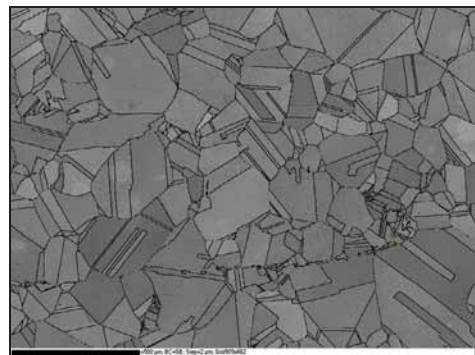


**Figure 104.** EBSD pattern quality map with superimposed grain boundaries of hydrogen annealed sample 4DV. Entrapped oxide particles and the related small grain size can be faintly seen. Length of the scale bar is 500  $\mu\text{m}$ . (Savolainen et al. 2008)

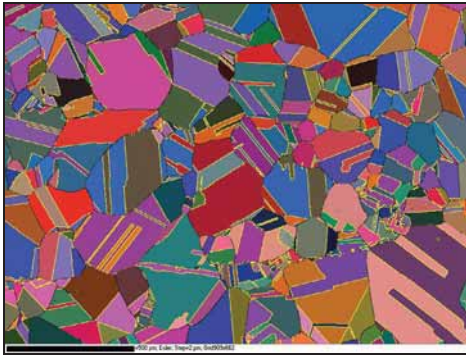


**Figure 105. Euler map of hydrogen annealed sample 4DV. Twin boundaries are seen as yellow. Length of the scale bar is 500  $\mu\text{m}$ . (Savolainen et al. 2008)**

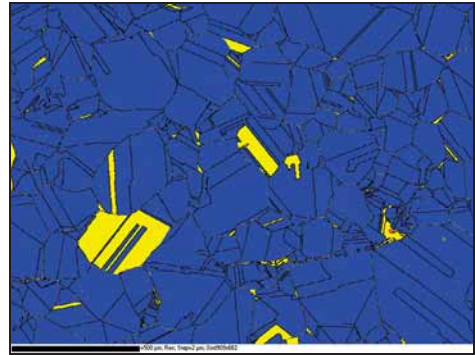


**Figure 106. Recrystallized fraction of hydrogen annealed sample 4DV. Recrystallized fraction is shown in blue and substructured in yellow colour. Length of the scale bar is 500  $\mu\text{m}$ . (Savolainen et al. 2008)**

#### 10.4.3 Pinning Effect of Entrapped Oxide Particles

The entrapped oxide particles in the Cu-OFP bead-on-plate FSW welds had a pinning effect on the grain boundaries and consequent grain size of the welds. Even after annealing the samples at 850°C for 30 min, the grain size in the region of entrapped oxide particles has remained small. Figures 107 and 108 show FSW samples without and with hydrogen annealing, respectively. The samples are mirror images of each other. (Savolainen et al. 2008)

Table 11 shows the average grain size of the base material and the studied bead-on-plate Cu-OFP FSW welds (1D, 1DV, 4D, and 4DV). The grain size in the as-welded condition (samples 1D and 4D) is roughly the same, about 25  $\mu\text{m}$ . In the hydrogen-annealed samples the grain size is significantly larger, about 80 and 140  $\mu\text{m}$  depending on the amount of entrapped oxides particles. The sample FSW welded with no oxide removal or shielding gas has the average grain size of 80  $\mu\text{m}$  and the sample FSW welded with both oxide removal and use of shielding gas has the grain size of about 140  $\mu\text{m}$ . (Savolainen et al. 2008)

Table 11. The average grain size of the Cu-OFP base material and FSW welded samples 1D, 1DV, 4D, and 4DV (Savolainen et al. 2008).

	Grain size ( $\mu\text{m}$ )	
	Horizontal	Vertical
Base material	182	183
1D	26	22
1DV	80	74
4D	25	23
4DV	141	122

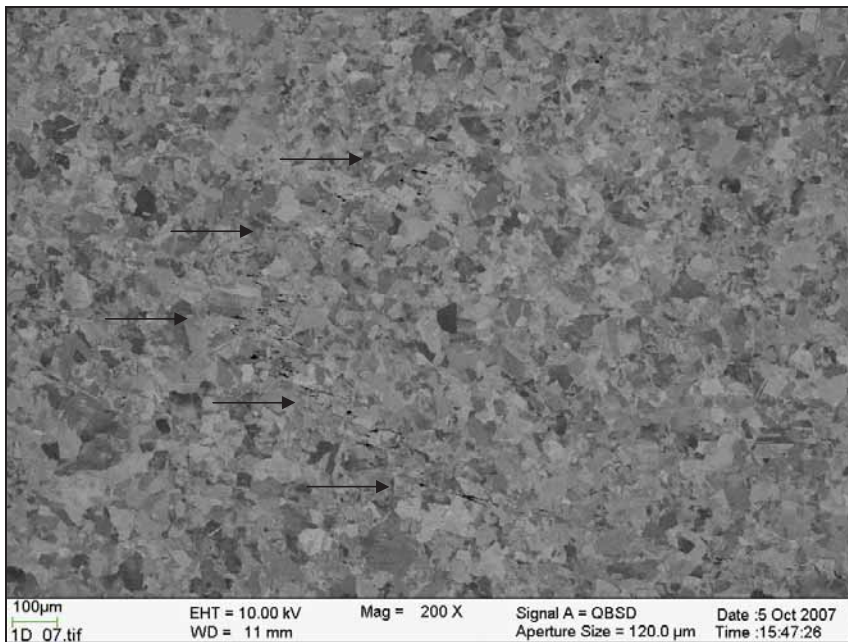
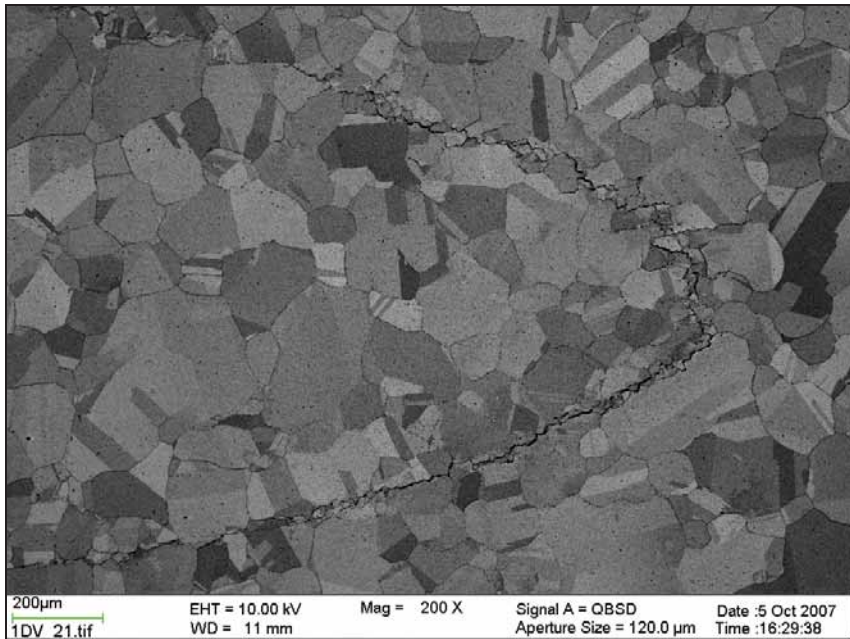


Figure 107. An SEM image of the reference sample 1D (FSW welded with no oxide removal or shielding gas) in the as-welded condition. Entrapped oxide particles can be seen very faintly as a dark semi-continuous line (pointed out by arrows). (Savolainen et al. 2008)



**Figure 108.** An SEM image of the hydrogen annealed reference sample 1D, mirror image of the as-welded reference sample 1D seen in Figure 107. The region of entrapped oxide particles as well as the consequent small grain size can be clearly seen. (Savolainen et al. 2008)

## 10.5 Optical Strain Measurement

Localization of plastic deformation in different parts (forged and extruded Cu-OFP base materials for lid and tube, FSW and EB welds) of the 50 mm thick copper corrosion barrier canister for spent nuclear fuel was studied. Figures 109-112 show the results of the optical strain measurements at the point of fracture. All images have the same scale for strain (0-3.5). All samples exhibit similar uniform elongation with the exception of the EB weld. In EB weld the extruded tube material has much longer elongation than the forged lid material. (Savolainen et al. 2010)

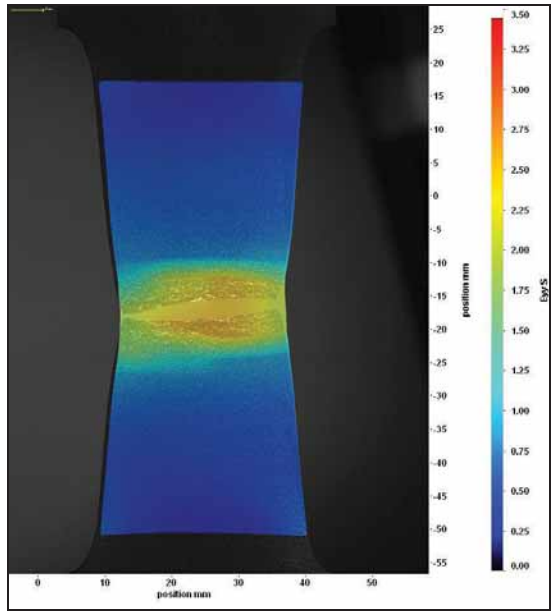


Figure 109. Strain map at the point of fracture of the Cu-OFP lid material of the spent nuclear fuel corrosion barrier canister (Savolainen et al. 2010).

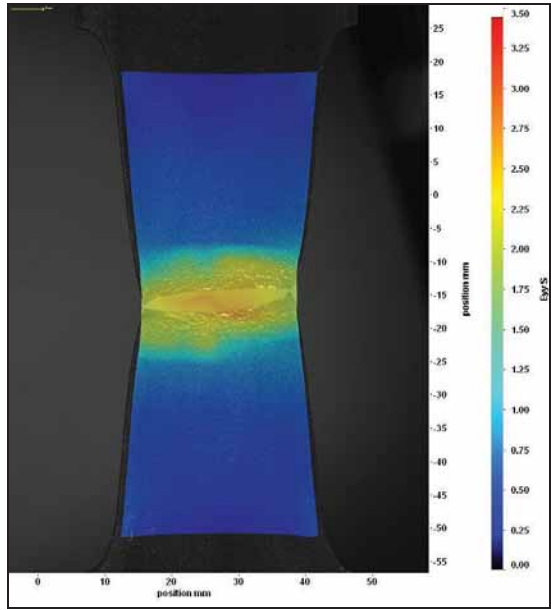


Figure 110. Strain map at the point of fracture of the Cu-OFP tube material of the spent nuclear fuel corrosion barrier canister (Savolainen et al. 2010).

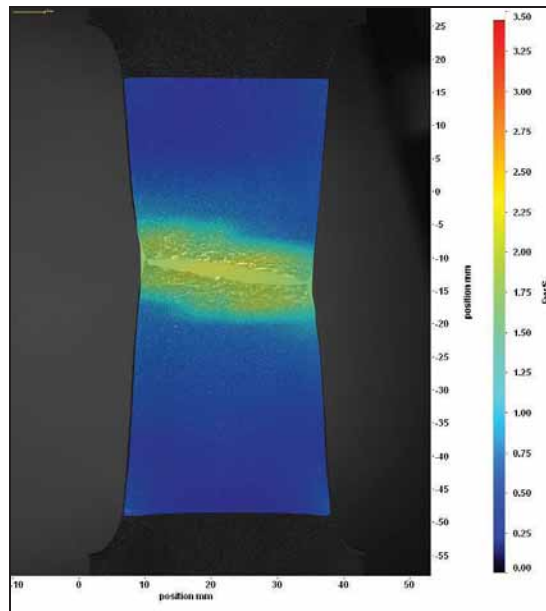


Figure 111. Strain map at the point of fracture of a Cu-OFP FSW weld of the spent nuclear fuel corrosion barrier canister. Lid material is on the top and tube material on the bottom. The fracture occurs in the weld closer to the lid material along a line of entrapped oxide particles. (Savolainen et al. 2010)

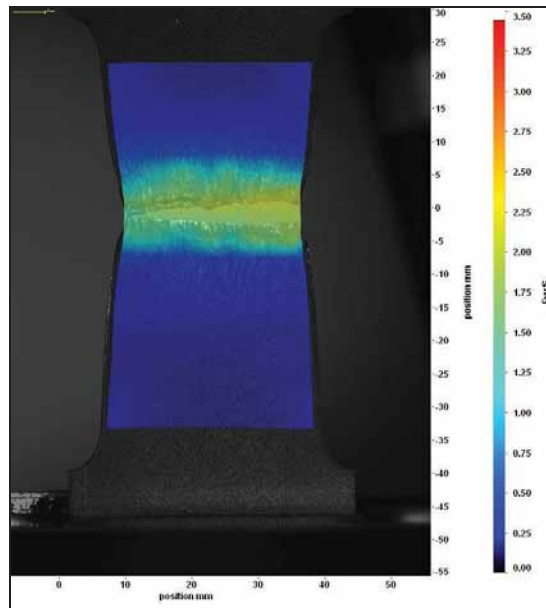
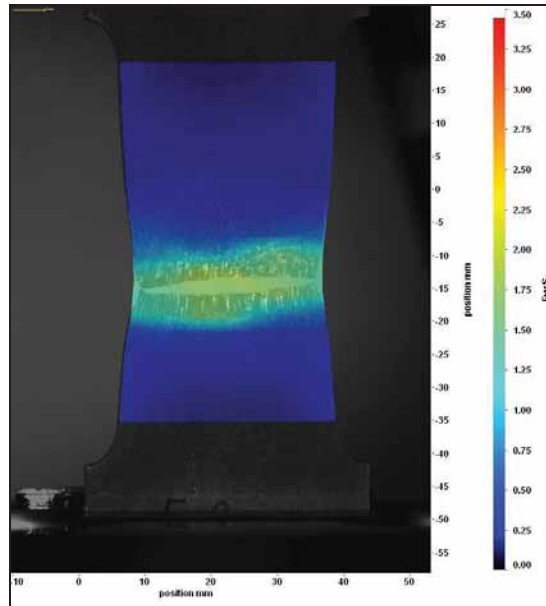


Figure 112. Strain map at the point of fracture of a Cu-OFP EB weld of the spent nuclear fuel corrosion barrier canister. The sample fractured at the centre of the weld. Lid material is on the top and tube material on the bottom. Deformation localizes in the middle of the weld with large grain size. It can also be seen that the extruded tube material has higher elongation than the forged lid material. (Savolainen et al. 2010)



**Figure 113. Strain map at the point of fracture of a Cu-OF EB weld of the spent nuclear fuel corrosion barrier canister. The sample fractured at the HAZ. Tube material is on the top and lid material on the bottom. Deformation localizes to the HAZ. It can also be seen that the extruded tube material has higher elongation than the forged lid material. (Savolainen et al. 2010)**

## 10.6 Mechanical Properties of the Welds

Mechanical properties of the different copper base materials and FSW welds were studied using tensile tests, hardness measurements, and bend tests.

### 10.6.1 Tensile Tests

Table 12 shows the transverse (to the rolling direction in the base materials and welding direction in the FSW welds) tensile test results of 10-11 mm thick Cu-OF (cold-rolled) and Cu-DHP (hot-rolled) base materials and FSW welds. The Cu-OF samples fractured at the weld. Figure 114 shows the Cu-OF FSW weld tensile test specimens and the base material specimen. The Cu-DHP samples fractured at the HAZ. Figure 115 shows the Cu-DHP FSW weld specimens and the base material specimen. (Savolainen et al. 2004)

Table 12. Transverse tensile test results of Cu-OF and Cu-DHP base materials and FSW welds. (Savolainen et al. 2004)

Material	Notation	Yield Strength, MPa	Tensile Strength, MPa	Elongation to Fracture, %
Cu-OF, base	OF1	292	298	13
Cu-OF, weld	07-04-02-VA	128	217	38
Cu-OF, weld	07-04-02-VB	120	217	38
Cu-DHP, base	D1	66	208	56
Cu-DHP, weld	06-19-01-VA	103	216	50
Cu-DHP, weld	06-19-01-VB	112	230	44
Cu-DHP, weld	06-19-02-VA	109	215	47
Cu-DHP, weld	06-19-02-VB	115	215	47
Cu-DHP, weld	06-23-01-VA	108	215	50
Cu-DHP, weld	06-23-01-VB	109	216	47

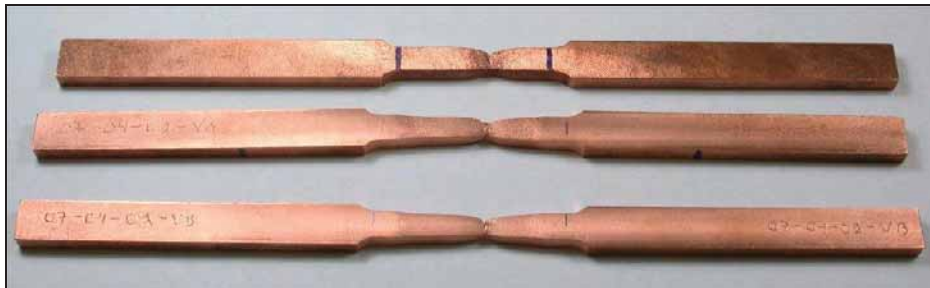


Figure 114. Cu-OF tensile test specimens. The base material specimen is on the top. It can be seen that the FSW welded Cu-OF specimens have failed in the weld metal and that the welded specimens exhibited higher elongations to fracture than the cold worked base material. (Savolainen et al. 2004)



**Figure 115. Cu-DHP tensile test specimens. The base material specimen is on the top. The FSW welds are located at the centre of the gauge lengths. The fracture locations in the HAZ/base material region of the FSW welds can be seen. (Savolainen et al. 2004)**

Localization of plastic deformation in different parts (forged and extruded Cu-OFP base materials, FSW and EB welds) of the 50 mm thick copper corrosion barrier canister for spent nuclear fuel was studied with tensile tests. Large samples containing almost the entire weld or base material thickness were studied using tensile testing with optical strain measurement (see Figures 109-113). The results show that in the base materials the deformation occurs uniformly over the entire gauge length. In FSW welds the deformation localizes in the weld at the line of entrapped oxide particles or at the processing line next to the line of entrapped oxide particles. Fracture occurs in a ductile manner. Figure 118 shows the ductile fracture surface of a copper FSW weld with dimples and shear lips indicating a ductile fracture process. In EB welds the deformation localizes in the large grains in the middle of the weld (EB centreline) or at the steep grain size gradient between the weld and the tube material (EB HAZ). Tensile strength is the lowest in the EB welds (175 MPa as compared to 200 MPa or higher for the other samples). Elongation to fracture in the FSW welds is similar to those of the base materials, but for the EB welds it is significantly lower (appr. 40 % as compared to 65 % in the base materials). Figure 120 shows the stress-strain curves for each  $5 \times 10^{-4}$  1/s test sample. The stress-strain curves for test samples with  $10^{-5}$  and  $10^{-6}$  strain rates were very similar to those of the  $5 \times 10^{-4}$  1/s samples. (Savolainen et al. 2012b)

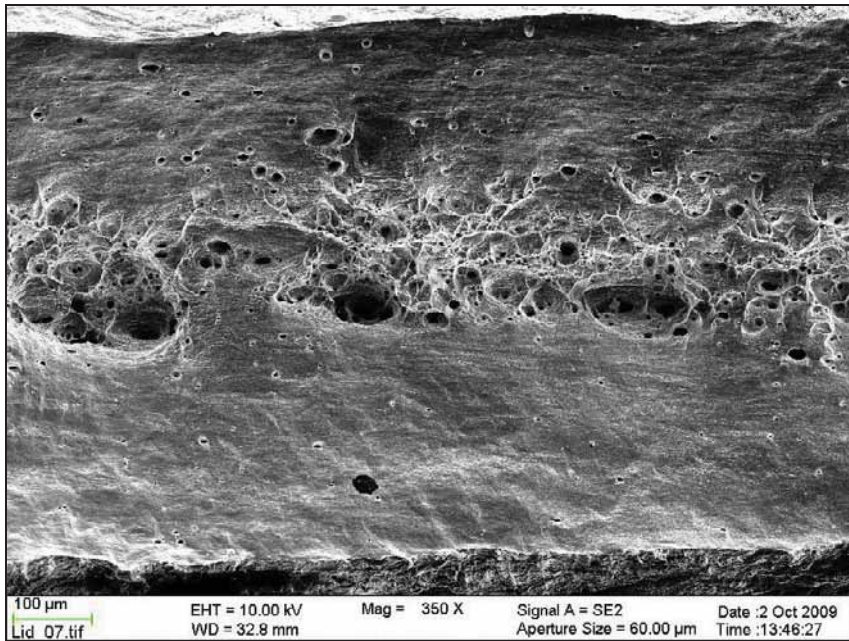


Figure 116. Fracture surface of a tensile test specimen made from 50 mm thick Cu-OFP lid base material. Dimples and shear lips indicate a ductile fracture process.

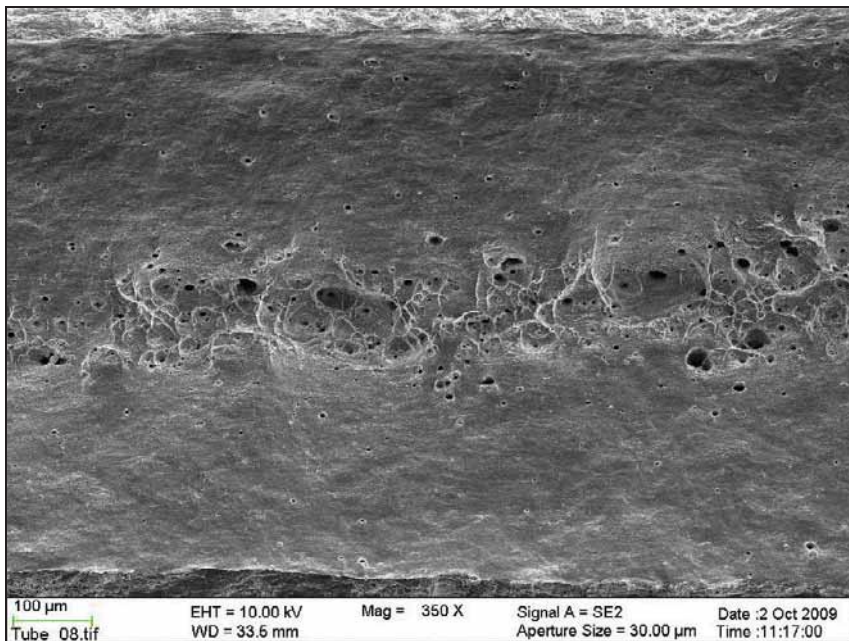
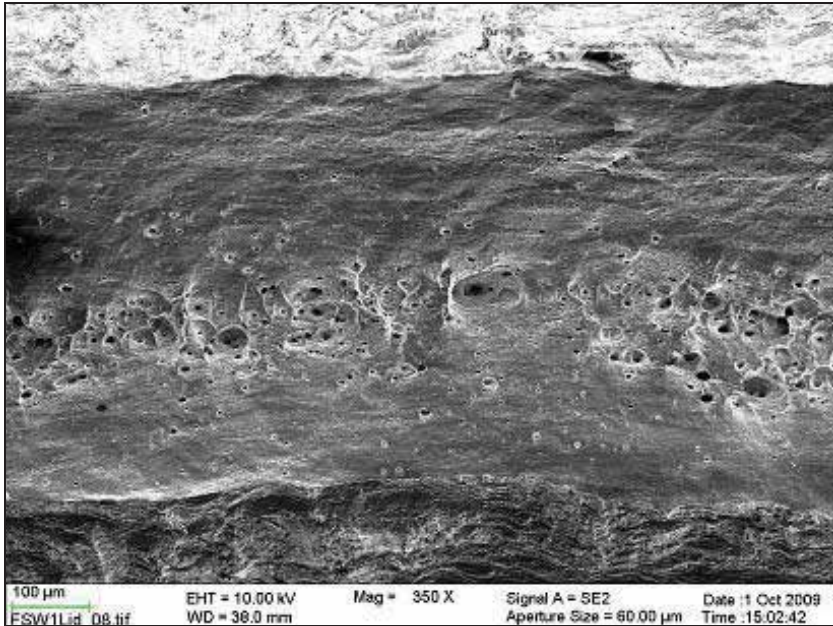
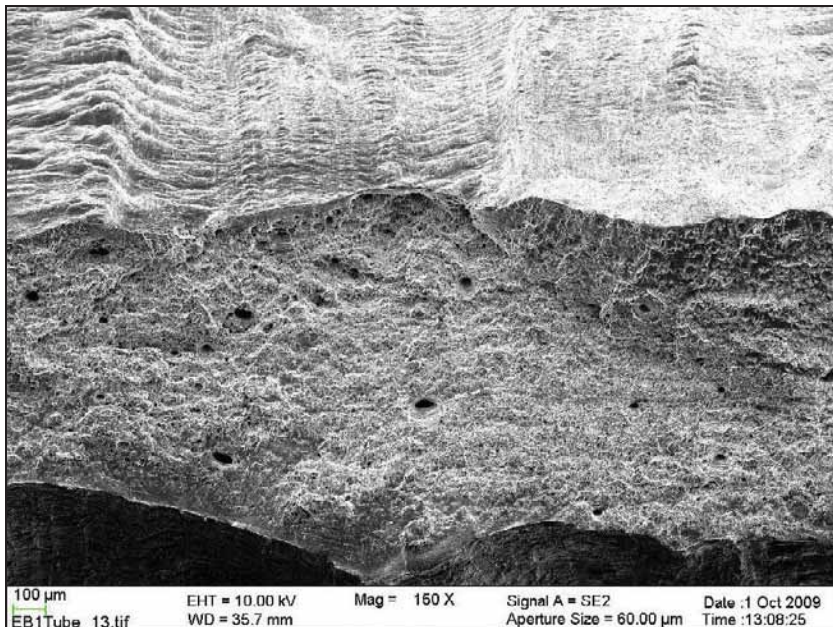


Figure 117. Fracture surface of a tensile test specimen made from 50 mm thick Cu-OFP tube base material. Dimples and shear lips indicate a ductile fracture process.



**Figure 118.** Fracture surface of a transverse tensile test specimen made from 50 mm thick Cu-OFW FSW weld. Dimples and shear lips indicate a ductile fracture process. (Savolainen et al. 2012b)



**Figure 119.** Fracture surface of a transverse tensile test specimen made from 50 mm thick Cu-OFW EB weld shows ductile shear fracture through the whole specimen. The fracture surface appearance differs significantly from those of the base materials and the FSW weld where shear lips formed on both side surfaces of the specimens. (Savolainen et al. 2012b)

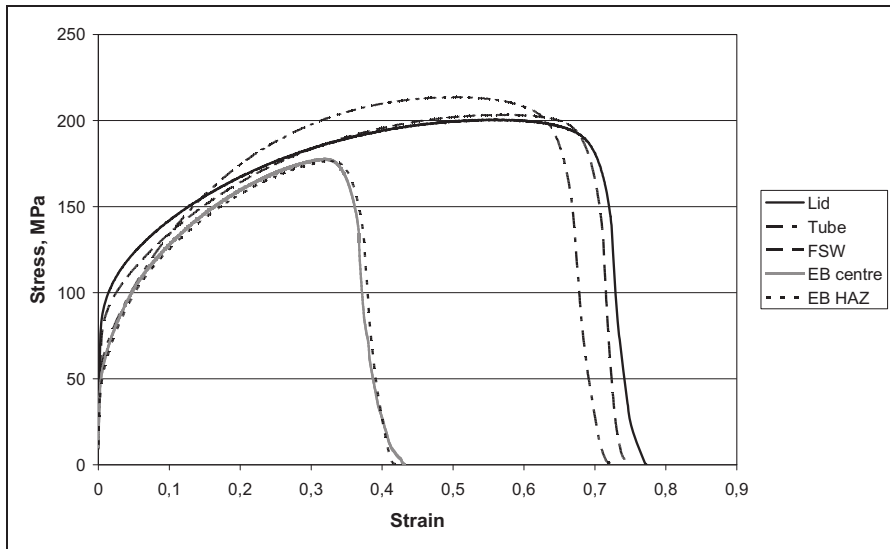


**Figure 120. Typical stress-strain curves of each Cu-OFP tensile test sample. It can be seen that the tensile strength of the EB welds is low as compared to that of the other samples. The tensile strength of the EB weld is 175 MPa as compared to 200 MPa or higher of the other samples. (Savolainen et al. 2010)**

The fracture locations of the FSW welds are shown in Figure 121. FSW welds fractured at two specific locations, either along a processing line close to the line of entrapped oxide particles or along the entrapped oxide particle line. Majority of the samples fractured at the processing line. The fracture locations were determined by cutting the fractured samples in four pieces perpendicular to the fracture on both sides of the fracture and electrolytically polishing the samples to reveal the entrapped oxide particles. (Savolainen et al. 2012b)

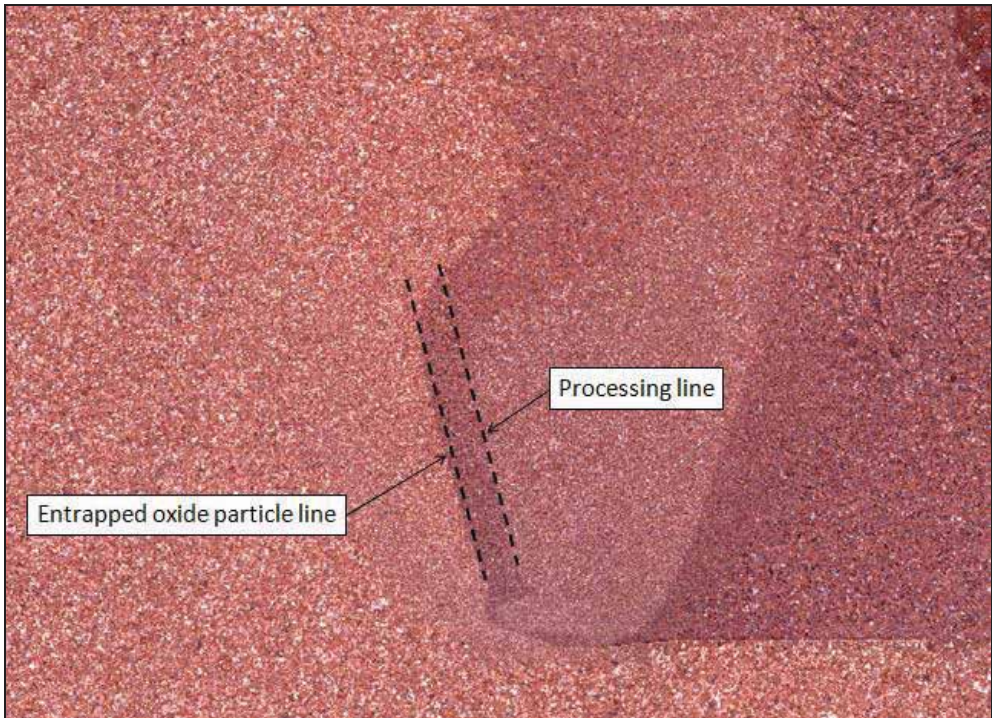


**Figure 121. Fracture locations in a 50 mm thick FSW weld of a copper canister for spent nuclear fuel. Lid material is on the retreating side (right) and tube material on the advancing side (left). (Savolainen et al. 2012b)**

Figures 122-126 show details of the fracture locations in the 50 mm thick Cu-OFP FSW welds. Figure 122 shows an EBSD pattern quality map of a part of the processing line. The processing line cannot be detected by EBSD. Figure 123 shows the local misorientation map of the same location and Figure 124 provides the colour key for the local misorientation map. Figure 125 shows a detail of the entrapped oxide particle line after electrolytic polishing. The voids left by the entrapped oxide particles can be seen due to the used experimental method of electrolytic etching. Figure 126 shows a larger magnification FEG-SEM image of a detail of the entrapped oxide particle line in the same FSW weld. (Savolainen et al. 2012b)

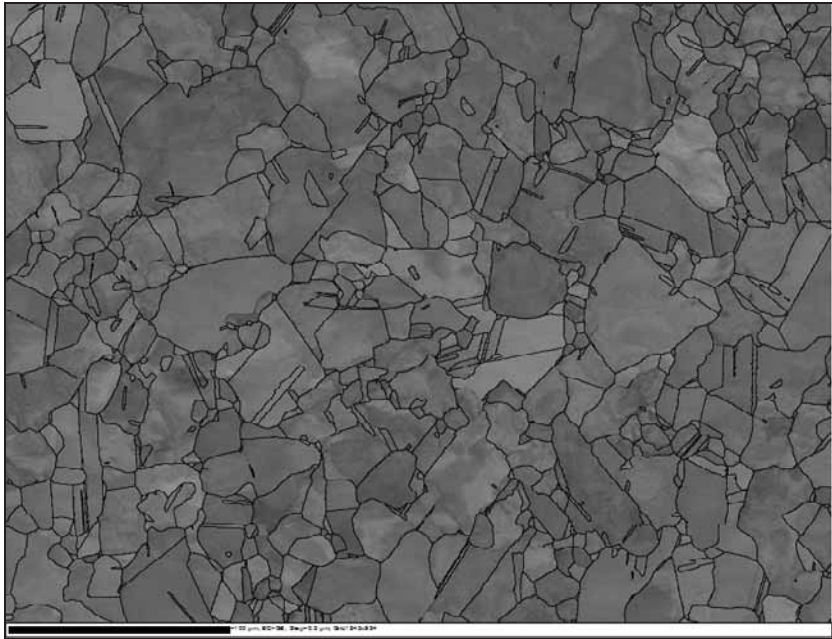


**Figure 122.** EBSD pattern quality map of a detail of the processing line. Length of the scale bar is 100  $\mu\text{m}$ .

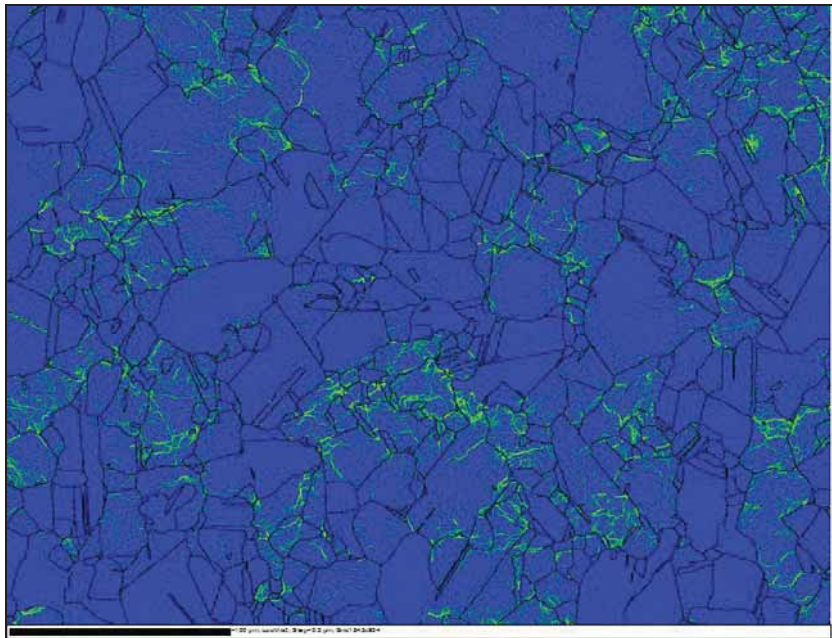


**Figure 123.** Local misorientation map of the same location of the processing line as in Figure 122. Figure 124 provides the colour key. (Savolainen et al. 2012b)

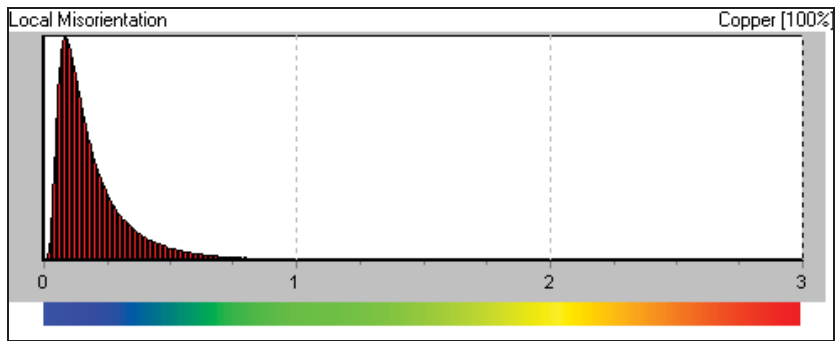
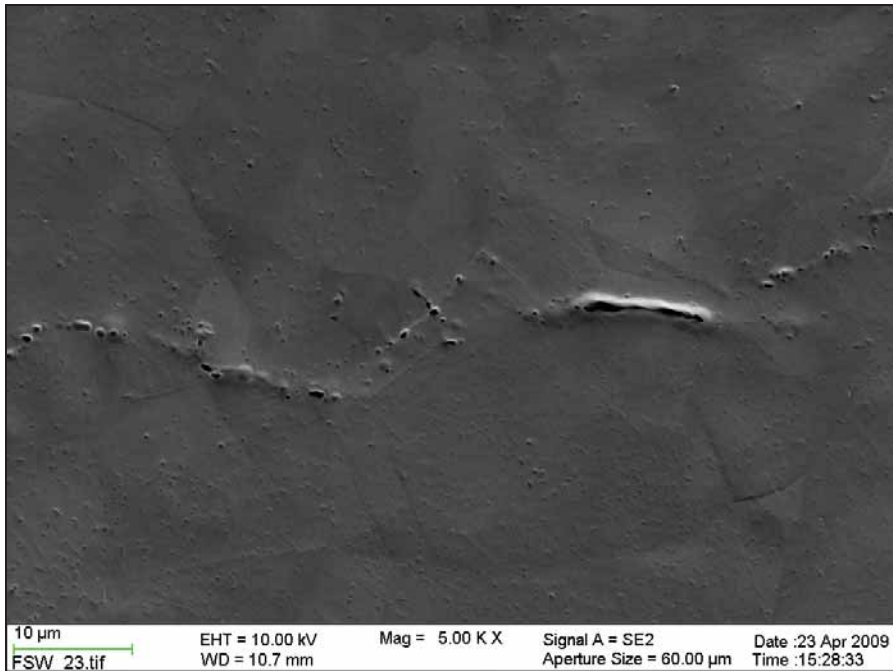


Figure 124. Colour key for the local misorientation map in Figure 123. (Savolainen et al. 2012b)

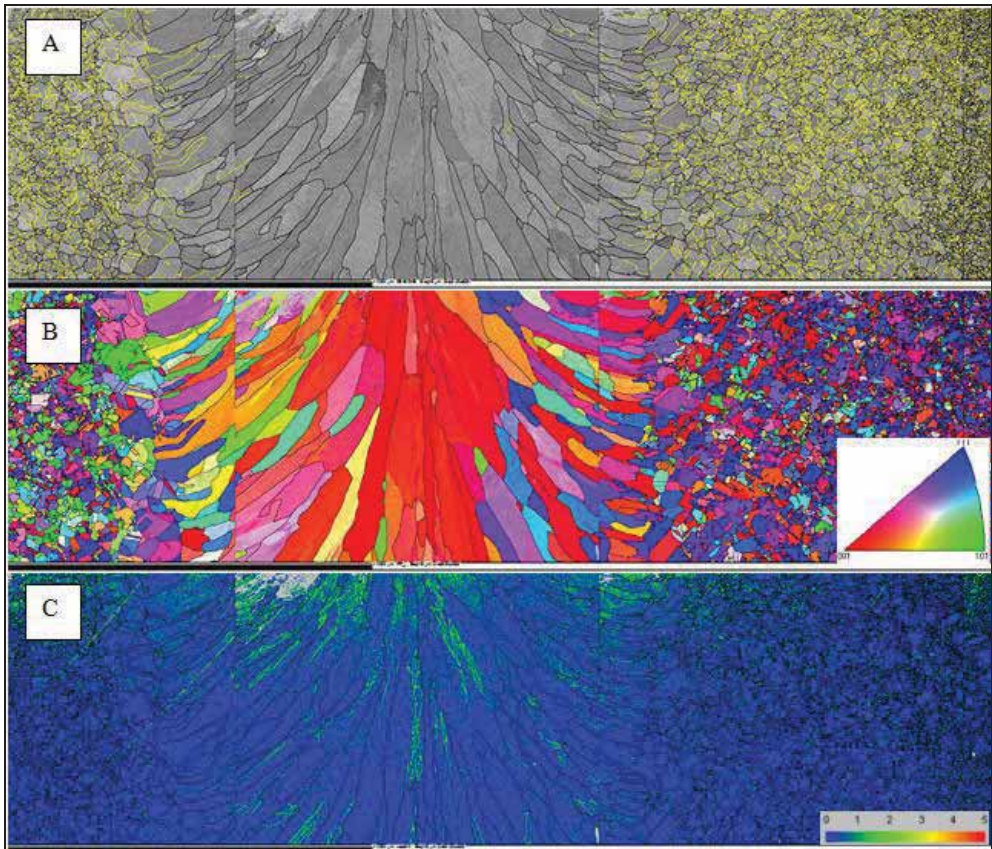


Figure 125. A detail of the entrapped oxide particle line in a 50 mm thick Cu-OFP FSW weld shown in Figure 121. (Savolainen et al. 2012b)



**Figure 126. FEG-SEM image of a detail of the entrapped oxide particle line seen in Figure 121.**

Figure 127 shows EBSD maps of a horizontal cross-section of the EB weld. Lid base material is on the left. Figure 127a is a pattern quality map showing the grain size distribution in the EB weld and in the base materials. The yellow lines show twin boundaries. The amount of twin boundaries is high in the base materials but not in the EB weld. Figure 127b is an inverse pole figure map (IPF) in the Z-direction showing that in the middle of the EB weld a highly oriented microstructure with  $\langle 100 \rangle$  direction is dominating. Figure 127c is a local misorientation map showing the local concentration of higher strain (green colour) at the centreline of the weld and close to the fusion lines between the weld metal and the base materials. (Savolainen et al. 2010; Savolainen et al. 2012b)



**Figure 127. EBSD maps of a horizontal cross-section of the EB weld. Lid base material is on the left. a) Pattern quality map showing the distribution of grain size in the EB weld and the base materials. Twin boundaries are seen yellow. b) IPF map in the Z-direction shows that in the middle of the EB weld a highly oriented microstructure with  $\langle 100 \rangle$  direction is dominating. c) Local misorientation map showing the local concentration of higher strain (green) at the centreline of the weld and close to the fusion lines between the weld metal and the base materials. (Savolainen et al. 2012b)**

Uniform, non-uniform, and total strains of the samples can be seen in Table 13. Elongation to fracture of the base materials and the FSW welds is similar. However, for the EB weld it is significantly reduced as compared to the other materials. The reduction of non-uniform strain in the EB weld is even more pronounced than that of the uniform strain. Table 13 shows also strains at the gauge length as measured by LaVision, the used optical strain measurement system. The results differ from those obtained by the displacement measurement. The discrepancy is most likely due to elongation occurring over the entire

sample, not only at the gauge length, which is taken into account in the LaVision results. (Savolainen et al. 2010)

**Table 13. Uniform, non-uniform, and total strains of the samples as well as the results obtained by LaVision (Savolainen et al. 2010).**

	<b>Uniform strain</b>	<b>Non-uniform strain</b>	<b>Total strain</b>	<b>LaVision</b>
<b>Tube</b>	0.50	0.23	0.73	0.65
<b>Lid</b>	0.56	0.21	0.77	0.66
<b>FSW</b>	0.55	0.18	0.73	0.61
<b>EB centre</b>	0.32	0.11	0.43	0.40
<b>EB HAZ</b>	0.32	0.10	0.42	0.38

#### 10.6.2 Hardness Profiles

Hardness profiles were measured over the transverse cross-section of Cu-OF FSW welds with 10 mm thick cold-rolled base material and Cu-DHP FSW welds with 11 mm thick hot-rolled base material. In the work-hardened Cu-OF material the hardness was clearly lower in the weld than in the base material, corresponding to the hardness of base material in annealed state. Hardness of the Cu-DHP welds was equal to that of the annealed base material. Figure 128 shows the hardness profiles measured at the centre line of the welds. For Cu-OF hardness measurements the weight of 1 kg (HV 1) was used and for Cu-DHP welds the weight was 0.5 kg (HV 0.5). (Savolainen et al. 2004)

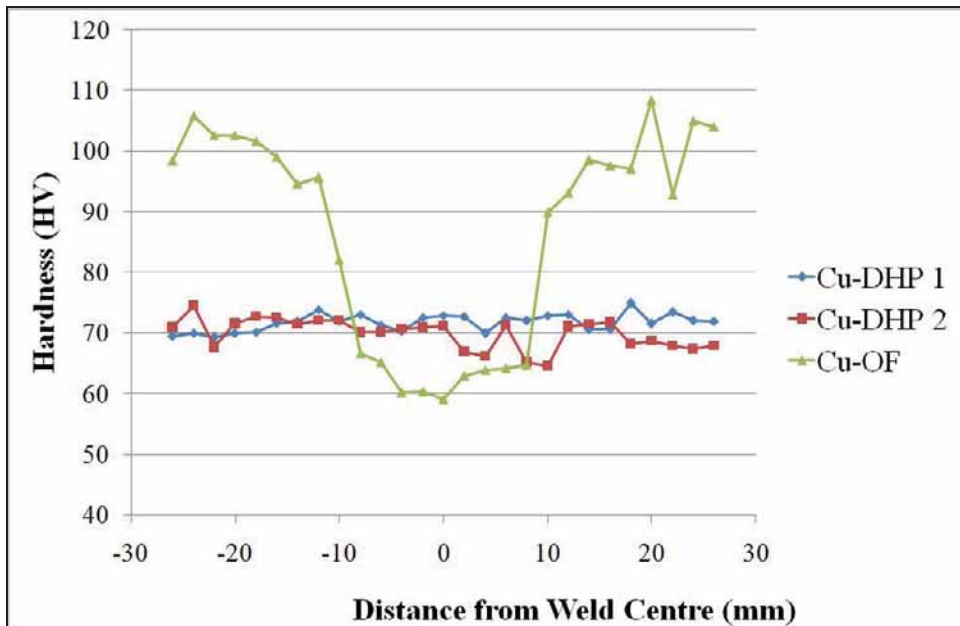


**Figure 128. Hardness profiles of Cu-OF (HV 1) and Cu-DHP (HV 0.5) FSW welds (based on results in Savolainen et al. 2004).**

Horizontal and vertical hardness profiles were measured for 5.5 mm thick Cu-OFP bead-on-plate FSW welds with hot-rolled base material. In the horizontal hardness profiles the hardness is higher in the weld than in the HAZ/base material region. All samples show similar results. Also the vertical hardness profiles show similar tendency for higher hardness in the weld than in the HAZ/base material. Figure 129 shows the measured horizontal hardness profile and Figure 130 the vertical hardness profile. (Savolainen et al. 2008)

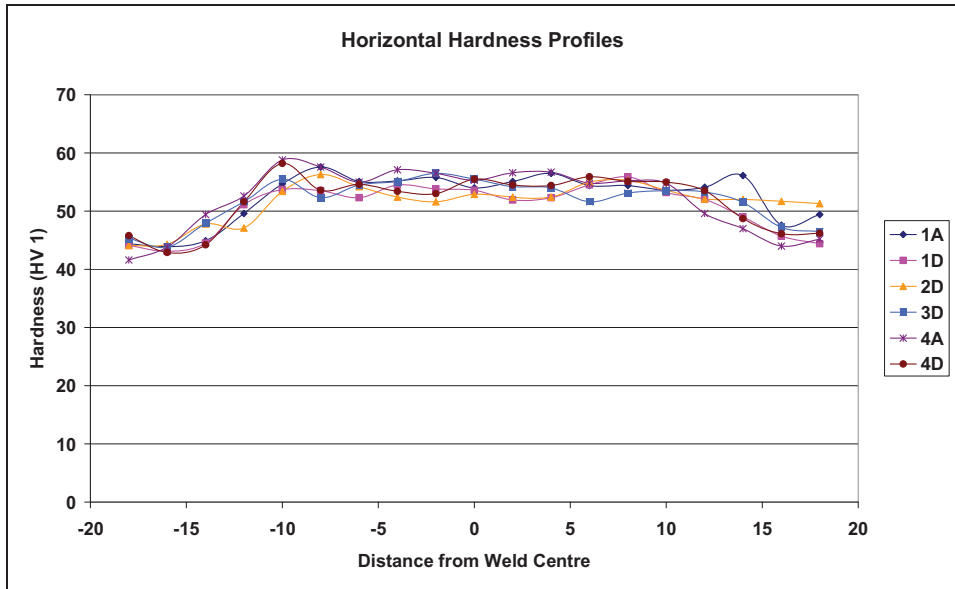


Figure 129. Horizontal hardness profiles of 5.5 mm thick Cu-OFP bead-on-plate FSW welds. Hardness is higher in the weld zone than in the HAZ/base material region. Higher hardness is most likely due to the smaller grain size in the nugget, according to the Hall-Petch relation modified for Cu-OF. (Savolainen et al. 2008)

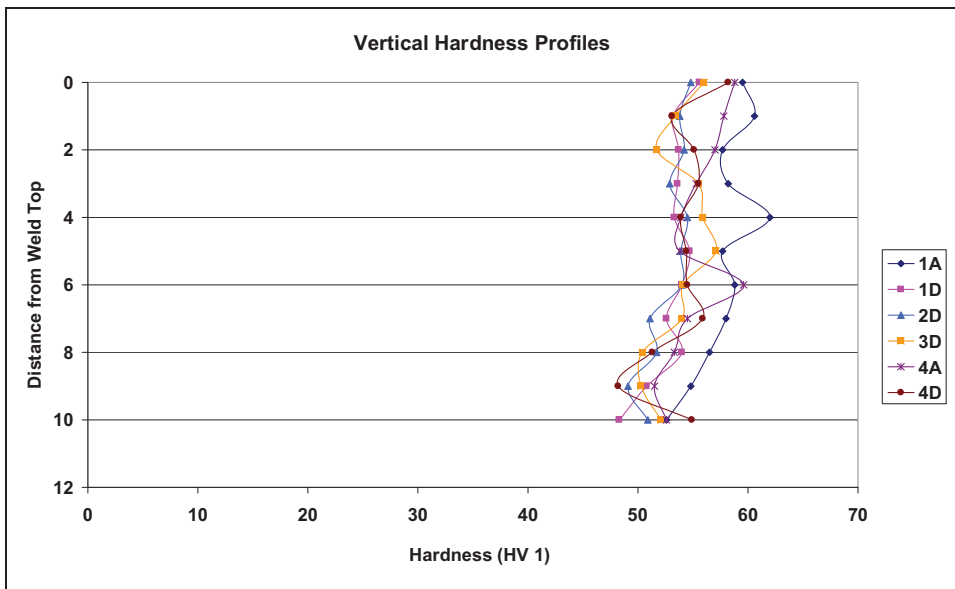


Figure 130. Vertical hardness profiles of 5.5 mm thick Cu-OFP bead-on-plate FSW welds. Results are consistent with those of horizontal hardness measurement. In the weld (0-6 mm) the hardness is slightly higher than in the HAZ/base material (6-10 mm). (Savolainen et al. 2008)

### 10.6.3 Bend tests

Double-sided FSW welds of cold-rolled Cu-OF and hot-rolled Cu-DHP with 10-11 mm plate thickness were studied using 180° three-point bend tests. All samples survived the bend tests without any signs of damage. Figures 131 and 132 show examples of the bend test specimens of Cu-OF and Cu-DHP, respectively. (Savolainen et al. 2004)



**Figure 131. Bend test specimen of Cu-OF (Savolainen et al. 2004).**

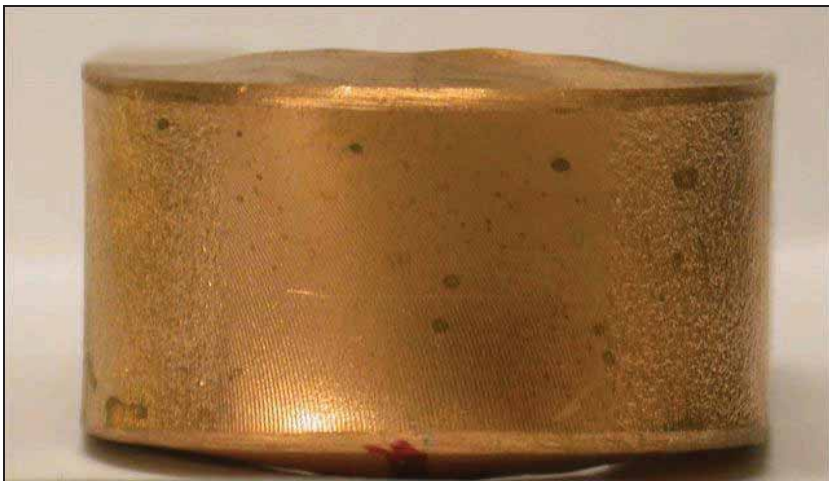


**Figure 132. Bend test specimen of Cu-DHP (Savolainen et al. 2004).**

## 10.7 Temperature Measurements

A typical chart depicting spindle power and tool temperature during FSW welding of copper is shown in Figure 133. Spindle power and tool temperature have a clear correlation, spindle power being slightly ahead the temperature. Welding of both sides of the plates is shown in the figure. The sequences that can be seen in the figure are as follows: plunging is seen as the first increase of both temperature and the spindle power. The shift from plunging to welding sequence is seen as a small decrease, and then the actual welding is observed as the main increase. Ending of the welding is seen as a steep decrease, and finally the lifting of the tool as a low spindle power usage. In some welds the steady state was reached during welding. The experimental welds were rather short due to restrictions caused by clamping. It would have been preferable to use longer welds. Thermal element was located inside the tool, next to a cooling channel. Therefore the absolute values are not reliable. Temperature was measured during welding using external temperature measurement which showed the temperature of about 850 °C.

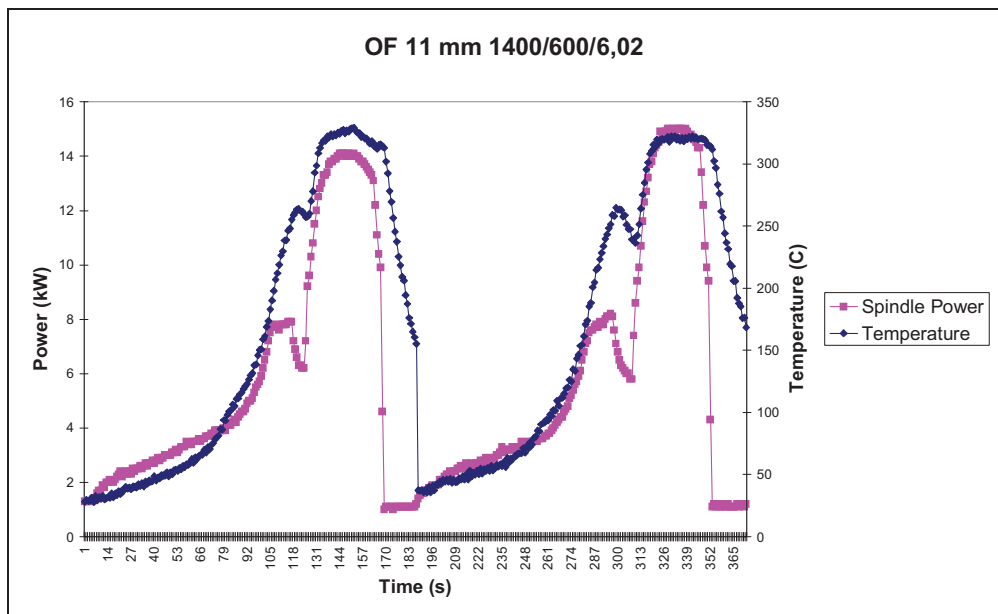


**Figure 133. Spindle power and tool temperature during two FSW welding cycles of Cu-OF. The absolute temperature values are not reliable. The correct maximum/steady state temperature was about 850 °C.**

The use of shielding gas had a large effect on the welding parameters. Parameters producing defect-free welds without the shielding gas produced welds with small voids

when using shielding gas. Temperature measurement showed that the temperature during welding with shielding gas was about 20 °C lower than without shielding gas (735 and 755 °C, respectively), as seen in Figure 134. The decrease of the temperature may be due to lower rotation speed caused by sticking of the material to the tool as there are fewer oxides to promote slipping.

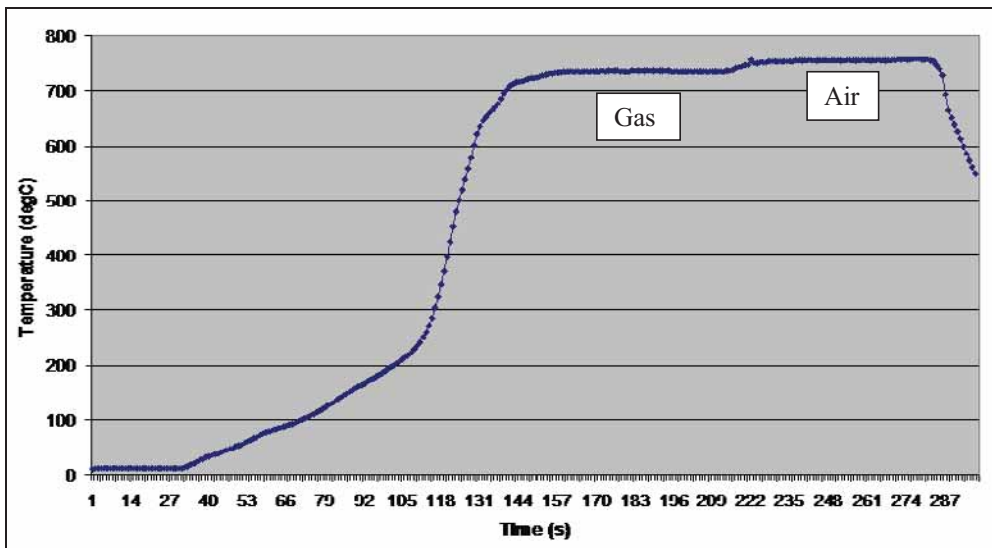


Figure 134. Temperature measurement with and without shielding gas during FSW of Cu-OFP (Savolainen et al. 2008).

## **11 DISCUSSION**

In this Doctoral Thesis, the microstructure and mechanical properties of copper and Cu/Al dissimilar metal FSW welds were studied. The entrapped oxide particles in copper FSW welds and the localization of plastic deformation in different parts of the copper canister for spent nuclear fuel were also explored. In this chapter the results are discussed and compared to those of other studies.

### **11.1 FSW of Copper and Copper Alloys**

FSW is an efficient way to join copper and copper alloys. The heat necessary to plasticise the base material is produced on-site, solving partly the problem caused by the high heat conductivity of copper which makes the use of fusion-based welding method difficult or impossible. Additionally, as no melting occurs during FSW and the joint is formed under hot-working conditions, the grain size remains small. For joining of thick section copper there is only one other available welding method, EB, which however causes extremely large grain size of the joint.

### **11.2 Microstructure of the Welds**

#### **11.2.1 Grain Structure**

EBSO results (Figures 46-49 and 52) show that FSW of copper produces a dynamically recrystallized microstructure with small, equiaxed grains and increased amount of twin boundaries. The results of EBSD studies of copper FSW welds are consistent with those of Lee and Jung (2004). They observed recrystallized grain structure and annealing twins in the nugget of copper FSW welds in transmission electron microscopy (TEM) studies. They also noticed a significant decrease in the density of dislocations as compared to the base material. Dalla Torre et al. (2007) ascribed the increase in the amount of twin ( $\Sigma 3$ ) boundaries to the occurrence of recovery and recrystallization.

### 11.2.2 Grain Size

FSW produces weld joints with a small grain size. Grain size depends on the welding parameters, not on the original grain size of the base materials. Welding parameters define the strain rate and temperature during welding which in turn control the dynamic recrystallization and the resulting grain size.

In copper canisters for spent nuclear fuel the grain size should be smaller than 360  $\mu\text{m}$ . In 50 mm thick copper FSW welds the grain size (60  $\mu\text{m}$ ) is equal to or smaller than that in the base materials (60-70  $\mu\text{m}$  depending on the manufacturing method), consistent with the results of Andersson (2005). In EB welds the grain size is considerably larger, up to 12 mm.

Not only is the grain size of FSW welds in the copper canisters small and similar to the base materials, but also the grain size gradient between the FSW weld and the base material is smooth. Between the EB weld and the base material the grain size gradient is very steep. Both the small grain size and smooth grain size gradient make FSW a more attractive option for sealing the spent nuclear fuel canister, as the differences between the joint and the base materials are small.

### 11.2.3 Texture

Texture in copper FSW welds is dependent only on the welding parameters, not on the grain structure or texture of the base material. Due to the occurrence of DRX, texture is nearly random in the weld nugget.

With cold-rolled Cu-OF base material, the transition from the nugget to the base material can be seen as a change from the nearly random texture of the nugget to cube texture in the TMAZ/HAZ region, and further to rolling texture in the base material (Figure 52). With a hot-worked base material such a change is not necessarily seen and it may be difficult to distinguish the weld zones based on the joint texture. In the copper canisters for spent nuclear fuel, the Cu-OFP base material is in hot-worked condition with a small grain size. An important consideration is the similarity of FSW welds and base materials in copper canisters also in regards to texture.

The texture in copper FSW welds cannot be directly compared to those of aluminium or stainless steels, because the materials have different stacking fault energies and, therefore, different restoration mechanisms form the resulting microstructure. In aluminium and stainless steels, the microstructure is dependent on the original microstructure due to recovery. In copper, the microstructure is formed by recrystallization and it is independent of the original microstructure, defined only by the (hot-forming) conditions.

#### 11.2.4 Precipitates

Precipitates in copper FSW welds have not been previously studied. It was noticed that the intensive deformation and high temperature during FSW cause the dissolution of  $\text{Cu}_2\text{S}$  precipitate particles into solid solution with copper matrix. The  $\text{Cu}_2\text{S}$  precipitate particles subsequently reprecipitate in a much finer form during cooling. The solubility of sulphur in copper increases rapidly at temperatures above 800 °C, consistent with the dissolution of  $\text{Cu}_2\text{S}$  precipitates in the temperature range of copper FSW, 800-900 °C.

### 11.3 Banding

Banding in copper FSW welds has been previously very little studied. Contrary to the aluminium alloy FSW welds, in normal “hot” copper FSW welds the banding is not readily visible. Copper FSW welds made with a large variety of welding parameters have been studied by Savolainen et al. (2004). None of the defect-free “hot” welds showed banding. Banding has only been seen in “cold” FSW welds. Also Xie et al. (2007) linked the formation of banding in copper FSW welds to insufficient heat input. They noticed that at higher rotation speeds (and, therefore, higher heat input) the banding disappeared and a microstructure with a fairly uniform grain size was formed.

EBSD results (Figures 57-63) show that banding consists of layers (or bands) of smaller (appr. 20  $\mu\text{m}$ ) and larger (appr. 60  $\mu\text{m}$ ) grains. Local misorientations are larger in the small grain areas than in the large grain areas. As there are almost no texture variations in the recrystallized copper FSW welds, it can be concluded that the differences in the grain size observed in the “cold” copper FSW welds are due to variations in the deformation

conditions between adjacent bands. The grain size variations are most likely caused by differences in strain rate (due to contact conditions, e.g. stick-slip between the tool and the base material). Higher strain rate leads to smaller grain size. The results are consistent with those of Xie et al. (2007).

#### **11.4 Cu/Al Dissimilar Metal FSW Welds**

FSW has the potential of producing good quality Cu/Al dissimilar metal FSW joints despite the large difference in the base material melting temperatures. Good strength and high electrical conductivity can be achieved, but the elongation to fracture tends to be low due to the formation of brittle intermetallic compounds.

Next to the correct welding parameters, the tool rotation direction and probe location in relation to the base materials are important. The stronger material (copper) must be on the advancing side and weaker material (aluminium) on the retreating side in order to avoid poor weld quality with surface-breaking voids. The result is consistent with other studies (for example, Okamura and Aota 2004; Xue et al. 2011a). Contrary to the general results on the subject, in this study the best results were obtained with the tool probe on the copper side. Tool probe at the joint centre or on the aluminium side resulted in poor weld quality due to the formation of voids. The reason for this is that the tool was designed for FSW of copper. In the other studies the tools were designed for FSW of aluminium. Effective tool geometries vary depending on the base material and the welding parameters, mainly tool rotation and traverse speed. Higher tool rotation and traverse speed values (as are generally used for aluminium) require more complex tool geometries as compared to those used for FSW of copper of similar plate thickness. For FSW of copper lower tool rotation and traverse speeds are used as copper is more difficult to FSW and generally welding speed is not an issue in copper FSW welds. Due to the differences in the welding parameter combinations of the two materials, tool geometry becomes important in dissimilar metal welds. Complicated Al tool geometries are not suitable for FSW of copper at the welding parameter combinations and the simple Cu tools are not capable of welding Al alloys.

#### 11.4.1 Tensile Tests

Tensile strength of the Cu/Al dissimilar metal FSW welds was good, comparable to that of the aluminium base material (Figure 67). However, elongation to fracture was low due to the formation of intermetallic compound layers. The results are consistent with those of other studies, for example by Liu et al. (2008) and Xue et al. (2010).

#### 11.4.2 Hardness Tests

The hardness measurement results (Figure 68) show softening in the HAZ, both in aluminium and copper, as well as high variation of hardness (50-220 HV) in the weld. The softening is due to annealing caused by the thermal cycle of FSW. The high hardness values (as compared to copper and aluminium base materials) in the nugget indicate the presence of intermetallic compounds in this area. The 0.5 kg measurement weight caused too large an indentation to enable the measurement of the real hardness of these IMCs. Further studies and microhardness measurements show that the hardness of the  $\text{Al}_2\text{Cu}$ -phase is 425-470 HV 0.05 and the hardness of the brittle AlCu-phase is 650-700 HV 0.05. The inaccuracies in the microhardness results are due to the thin character of the intermetallic phase layers. Ouyang et al. (2006) studied also FSW of Cu/Al dissimilar metal joints and noticed significant hardness variations in the welds. Hardness varied from 136 to 76 HV 0.2 depending on the microstructure of intermetallic compounds and material flow patterns. Braunović and Alexandrov (1994) measured the microhardness (HV 0.04 load) of the intermetallic phases formed when annealing friction-welded Al-Cu bars. Their results were as follows:  $\text{Cu}_2\text{Al}$ ,  $\text{Cu}_3\text{Al}_2$ ,  $\text{Cu}_4\text{Al}_3$ ,  $\text{CuAl}$ , and  $\text{CuAl}_2$  exhibited microhardness of 35, 180, 624, 648, and 413  $\text{kg/mm}^2$ , respectively. The microhardness values of AlCu and  $\text{Al}_2\text{Cu}$  phases in the study by Braunović and Alexandrov (1994) and this study are consistent with each other.

#### 11.4.3 Electrical Resistivity/Conductivity

The additional electrical resistance resulting from Cu/Al dissimilar metal FSW welds corresponds to the resistance of 3.1 mm long copper bar or 1.8 mm long aluminium bar of the same cross-sectional area. This result shows that the FSW joint is an attractive option for electrical conductivity purposes.

#### 11.4.4 Intermetallic Compounds

SEM studies of dissimilar metal Cu/Al FSW welds showed that all welds contain  $\text{Al}_2\text{Cu}$  compound. Typically, it is formed at the interface and in the nugget next to aluminium in a globular shape. At the studied welding temperatures the phase at the interface is always  $\text{Al}_2\text{Cu}$ . At higher temperatures  $\text{AlCu}$  is formed only in the nugget next to copper as a banded structure. Layers of phases other than  $\text{Al}_2\text{Cu}$  are generally too thin to be reliably analysed, but multiple phases can be seen.

SEM studies of the fracture surfaces of Cu/Al dissimilar metal FSW welds show that the welds fracture through a thin IMC layer. The layer was too thin (less than  $1\ \mu\text{m}$ ) to be reliably characterized with either EDS or EBSD. Elrefaey et al. (2005) noticed also that brittle fracture occurred in Cu/Al dissimilar metal FSW lap welds and that it was caused by the IMC layers. They used XRD to determine that the layers consisted of  $\text{Al}_4\text{Cu}_9$  and  $\text{AlCu}$  IMC phases. According to Braunović and Alexandrov (1994), the mechanical properties of friction welded copper-aluminium joints are strongly and adversely affected when the thickness of the IMC layer at the interface is larger than  $2\ \mu\text{m}$ .

During FSW the IMCs are dispersed and, with correct welding parameters, the amount of interconnecting layers can be minimised. SEM studies of the fracture surfaces of the Cu/Al dissimilar metal FSW welds revealed that the brittle IMC regions contain cracks which are stopped by the ductile aluminium at the interface (Figure 74). A similar effect was noticed by Ouyang et al. (2006). They assumed that local thermal stress concentrations in  $\text{CuAl}_2$  particles are higher than their fracture strength and they begin to crack. Crack growth is stopped by ductile copper lamellae. The restraining effect of copper prevents the formation of crack networks in the weld. An added benefit of IMCs is that their spheroidal form may increase the strength of the joint. Instead of completely avoiding the IMCs, the control of the thickness of the IMC layer at the weld interface as well as the size and distribution of the IMC particles in the nugget zone are the key factors (Xue et al. 2010).

## 11.5 Entrapped Oxide Particles

Entrapped oxide particles in copper FSW welds have been earlier very little studied. They are difficult to discover and require special sample preparation to be detectable. Electrolytic polishing has proved to be successful in revealing the location of the oxide particles. Unfortunately, it also removes the oxide particles from the surface and increases the size of the remaining holes. Another indirect method of observing the location and amount of entrapped oxide particles is hydrogen annealing. Formation of the pattern of entrapped oxide particle lines seems to be closely related to material flow as its pattern is very similar to that of banding. Figure 135 shows an entrapped oxide particle in an electrolytically polished copper FSW weld.

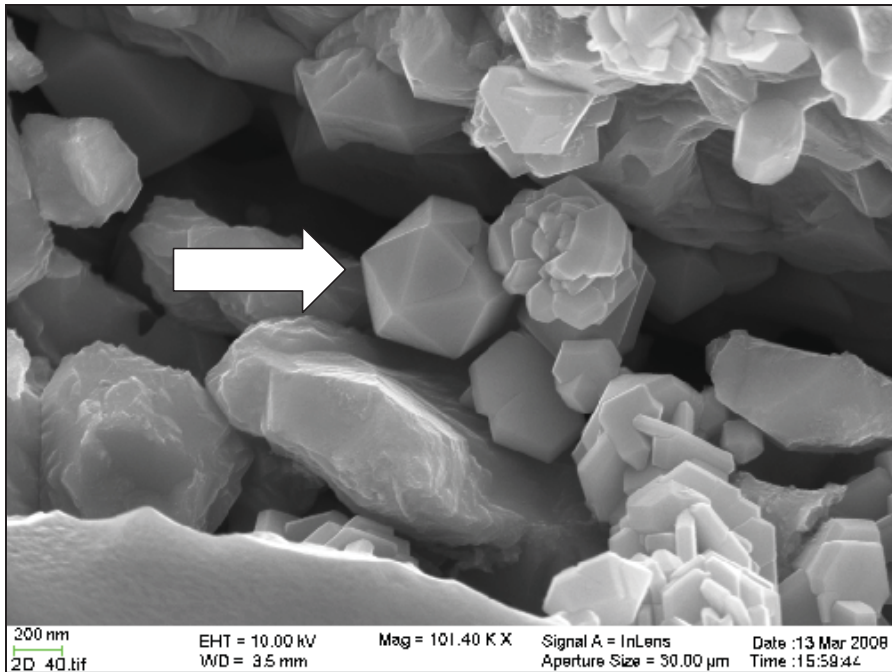


**Figure 135. Entrapped oxide particle in an electrolytically polished FSW weld of copper is marked with an arrow. Diameter of the oxide particle is about 0.5 μm.**

Figures 75-78 show the formation of the entrapped oxide particle line in Cu-OFW FSW welds. It is seen that the entrapped oxide particle lines originate from the butting surfaces. The deeper the original groove, the longer the line of entrapped oxide particles. In Figure 78, where the groove is deeper than the tool probe length, a part of the groove remains un-

welded and clearly shows the origin of the entrapped oxide particle line. The entrapped oxide particle line forms the typical S-curve seen in FSW welds. The results are consistent with those of, for example, Sato et al. (2004) regarding oxide particles in an aluminium alloy.

The effects of different combinations of oxide removal prior to FSW and use of shielding gas during FSW were studied using the same welding parameters and other arrangements for all the welds. The results (Figures 79-106) show that the combination of oxide removal and shielding gas gives the best result with almost no entrapped oxide particle line. Using only shielding gas gives the second best result, suggesting that the majority of oxides originates from air during welding. The oxidation reaction of copper at high temperatures is much faster than at room temperature. An interesting note is that the most pronounced oxide line is not in the reference sample with no treatment, but in the sample with oxide removal prior to welding and no use of shielding gas. This can be attributed to the lack of a protective oxide layer which makes the surface more susceptible to oxidation by air.

The effect of hydrogen annealing on Cu-OFP FSW welds is seen in high magnification in Figures 83-86. The voids indicate the existence of a relatively high amount of entrapped oxide particles in the weld whereas the existence of deformation indicates some reaction between the oxide particles in the welds and the hydrogen.

In addition to surface preparation and the use of shielding gas, the formation of entrapped oxide lines can be affected by the tool. Both tool features and tool location have an effect on the amount of detected oxide particles. More complex tool features (for example a scrolled shoulder) disperse the oxide particles more efficiently. The oxide particles are also more efficiently dispersed if the original joint line is on the advancing side of the tool, not in the centre of the tool (Kumar and Kailas 2010; London et al. 2003). In 50 mm thick welds the oxide particles are not seen in the top region of the weld where the tool features are more pronounced. Welds with more complex tool features also show more complex flow patterns.

What is also interesting to note, is the grain size of the material in each welded sample before and after hydrogen annealing. The weld samples were welded using the same parameters and they originally had the same grain size (before hydrogen annealing). After

hydrogen annealing, the grain size roughly corresponds to the amount of entrapped oxide particles. The higher the amount of entrapped oxide particles is, the smaller the resulting grain size. For example, in sample 1DV (no oxide removal, no shielding gas) the average grain size is half of that in sample 4DV (oxide removal, use of shielding gas). It seems that the small, relatively closely spaced entrapped oxide particles suppress the grain growth by particle pinning of the grain boundaries, i.e. that Zener pinning occurs in the samples with higher amounts of entrapped oxide particles. In Zener pinning the entrapped oxide particles and migrating boundaries interact resulting in the suppression of the grain growth (Humphreys and Ardakani 1996).

## **11.6 Localization of Plastic Strain**

The localization of plastic strain in different parts of the copper canister for spent nuclear fuel was studied in tensile tests with large samples containing almost the entire thickness of the FSW and EB welds as well as the forged lid and extruded tube base materials. In the base materials plastic deformation occurred very uniformly, but it was localized on specific sites in the welds. In FSW welds, deformation and fracture localized mainly on the processing line and occasionally on the line of entrapped oxide particles. The FSW welds and the base materials show similar hot worked microstructure. In EB welds, deformation and fracture localized either at the centre of the weld or at the fusion line between the weld and the forged lid base material. EB welds exhibit large columnar grains and have steep grain size gradients at the fusion lines between the weld metal and the base materials. Maximum allowed grain size in the copper corrosion barrier canisters for spent nuclear fuel is 360  $\mu\text{m}$  and in the EB welds grain sizes up to 12 mm were detected. FSW welds also have mechanical properties similar to those of the base materials. EB welds, however, show significantly smaller elongation to fracture and slightly lower tensile strength. The results on the properties of EB welds are inconsistent with those of Ollonqvist (2007). He measured the tensile properties of 50 mm thick EB welds using the proportional cross-weld tensile specimens with rectangular cross-section (10 mm x 8 mm). In the cross-weld testing failure occurred always in the centreline of the EB weld, but the measured elongations to fracture were high and comparable to the base material testing results. Specimens containing the whole weld area, which were used in this study, give a different view on the ductility of the EB welds. It is important to use full-thickness samples covering

the whole weld to have a realistic constraint of the weld structure with different microstructure and mechanical property gradients.

Fracture surfaces of the base materials and FSW welds (Figures 116-118) were similar with dimples and 45° shear lips on both side surfaces of the sample indicating ductile fracture. Fracture surfaces of EB welds (Figure 119) exhibited significantly different appearance. EB welds also fractured in a ductile manner, but with stronger strain localisation. Fracture occurred along a shear band (in large grains) through the entire weld sample.

## **11.7 Mechanical Properties of FSW Joints**

### 11.7.1 Tensile tests

Double-sided 10 mm thick Cu-OF FSW welds showed significant reduction in tensile strength and almost a three-fold increase in elongation to fracture as compared to the cold-rolled base material. The tensile strength of the FSW weld was 220 MPa and the tensile strength of the base material was 300 MPa. The elongations to fracture were 40 and 13 % for the FSW weld and the base material, respectively. The Cu-OF FSW weld samples failed in the weld. FSW has annealed the cold-worked Cu-OF increasing its ductility and simultaneously decreasing its hardness and strength. Hwang et al. (2010) had similar results. FSW welds of cold-worked C11000 copper had tensile strength of about 60 % as compared to that of the base material, whereas the elongation to fracture reached three times that of the base metal.

Tensile strength and elongation to fracture values of double-sided 11 mm thick Cu-DHP FSW welds were similar to those of the hot-rolled base material. The tensile strength of the FSW welds was slightly higher at 215-230 MPa compared to 210 MPa of the base material. Elongation to fracture of the weld was slightly lower at 50 % as compared to 55 % of the base material. Cu-DHP samples failed in the HAZ/base material region. In the hot-worked Cu-DHP FSW has caused no further annealing, but the difference in the results may be caused by the grain size gradients in the welds. The Cu-DHP results are in agreement with those of Andersson (2005). He compared 50 mm thick FSW welds to forged lid material using tensile testing. Samples were taken across and along the copper FSW weld. The

welds show tensile strength and elongation to fracture values similar to those of the base material (193-209 MPa of the weld as compared to 206 MPa of the base material). Elongation to fracture of the welds was 49-58 % compared to 51 % of the base material.

The results of transverse tensile tests of the entire 50 mm thick Cu-OF FSW and EB welds and of the forged and extruded base materials show similar tensile strength (200 MPa or higher, comparable to the results of Andersson (2005)) in all samples except the EB weld (175 MPa). The extruded tube material showed the highest tensile strength of 220 MPa. However, the elongations to fracture were higher compared to the results of Andersson (2005). The elongation results obtained by the cross-head displacement measurement differ from those measured with LaVision, an optical strain measurement system. The discrepancy is most likely due to the elongation occurring over the entire sample, not only in the gauge length, which is taken into account in the LaVision results. The values of elongation to fracture obtained by LaVision are basically more reliable and they are as follows: for both base materials 65 %, for FSW welds 60 %, and for EB welds 40 %. The influence of strain rate on the mechanical properties was negligible in the studied range ( $5 \times 10^{-4}$ ,  $10^{-5}$ , and  $10^{-6}$  1/s), as the tensile properties and fracture locations were the same for all corresponding test samples independent on the strain rate.

### 11.7.2 Hardness profiles

Hardness profiles of double-sided 10 mm thick Cu-OF FSW welds show that the weld is clearly softer than the cold-rolled base material. The hardness of the FSW weld is 60 HV 1 compared to the hardness of 100 HV 1 of the base material. The smaller grain size in the Cu-OF welds would suggest higher hardness as compared to the base material, but the effect of work hardening in the cold-worked base material exceeds the influence of the grain size refinement due to FSW. The reduction in hardness is visible through the entire width of the shoulder, not only through the width of the probe. Hwang et al. (2010) reported that in C11000 copper the hardness of the FSW weld was about 60 % of that of the base material, 60 HV compared to the hardness of 100 HV of the base material.

In double-sided 11 mm thick Cu-DHP FSW welds there is no difference in hardness between the hot-rolled base material and the weld. Cu-DHP was already in an annealed state; therefore the effects of FSW on the hardness were minimal. The smaller grain size

resulting from FSW had no hardening effect on Cu-DHP, contrary to the prediction based on the Hall-Petch relation. It can be concluded that the annealing softening was more dominant with the used welding parameters than grain refinement. Results similar to those of Cu-DHP were obtained by Andersson and Andrews (1999) for 50 mm thick Cu-OFP FSW welds with hot-worked base material. Hardness profiles across the transverse cross-sections showed relatively constant hardness values (60-70 HV 2.5) regardless of the grain size variations.

The horizontal and vertical hardness profiles (Figures 129 and 130) of 5.5 mm thick Cu-OFP bead-on-plate FSW welds show that the hardness is higher in the weld than in the hot-worked base material. The difference in hardness is due to the considerably smaller grain size in the weld nugget (25  $\mu\text{m}$  as compared to the 180  $\mu\text{m}$  of the base material), as both the base and weld materials are in hot-worked condition. The results are in agreement with the Hall-Petch relation.

### 11.7.3 Bend tests

The bend tests of double-sided FSW welds of cold-rolled Cu-OF and hot-rolled Cu-DHP with 10-11 mm plate thickness gave good results. All samples survived the three-point bend tests without any sign of damage, even when bending the samples by 180°. The results are consistent with those of Andersson and Andrews (1999), where 10 mm thick copper FSW welds were studied using 180° three-point bend tests for the root and face surfaces without failure.

## 12 CONCLUSIONS

The final disposal canister for spent nuclear fuel is the most critical application for FSW of copper. The other available welding method for sealing the corrosion barrier canister is electron beam welding (EBW). Based on the work performed in this Doctoral Thesis it can be concluded that the microstructure and mechanical properties (especially tensile strength and elongation to fracture) of copper FSW welds are very similar to those of the hot-worked base materials and superior as compared to EB welds. Based on these characteristics, FSW can be considered as a more suitable method for sealing the copper corrosion barrier canisters for spent nuclear fuel than EBW.

The microstructure of copper FSW welds has been little studied. It was noticed that FSW produces copper welds with a fine-grained recrystallized microstructure and almost random texture. The microstructure is complicated and it was studied using many different methods for a variety of copper grades and plate thicknesses. Studies included different weld zones, grain structure and size, texture, and precipitates.

Banding in copper FSW welds occurs as a difference in the grain size of the adjacent bands. It was noticed that local misorientations are larger in the small grain areas than in the large grain areas. It is assumed that the spatial differences in the grain size are due to variations in the strain rate (caused by contact conditions between the tool and base material).

Welding defects occurring in copper FSW welds are different from those in traditional fusion welds due to the solid state nature of the process. The welding defects are caused by instabilities in material flow (too cold or too hot conditions) or by geometric factors such as too short tool probe, too large tool displacement from the joint line, or plate thickness mismatch. A classification of the welding defects occurring in copper FSW welds in general and in 50 mm thick Cu-OFP FSW welds in particular was given.

The existence of entrapped oxide particles in copper FSW welds was confirmed. Their detection is difficult and requires complicated sample preparation. Entrapped oxide particles were confirmed to be originating from the butting surfaces. Their amount can be

reduced or even eliminated by removing the oxides from the butting surfaces prior to welding and by using shielding gas during welding.

The fracture in tensile tests of 50 mm thick copper FSW welds occurs either at the processing line next to the line of entrapped oxide particles or at the line of entrapped oxide particles. Fracture occurs in a ductile manner.

FSP is the most important variant of FSW. It is a method for local altering of the microstructure and the resulting properties. It can be used, for example, to heal casting defects, homogenize microstructure, produce surface composites, and to improve the formability.

Defect-free dissimilar metal FSW joints between copper and aluminium were successfully produced. The welds exhibit good tensile strength and electrical conductivity. However, the elongation to fracture was poor due to the formation of brittle intermetallic compounds. Cu/Al dissimilar metal FSW welds are of particular interest for the electrical power industry.

### 13 SUGGESTIONS FOR FUTURE WORK

Studies for the development of improved (easy and direct) ways of detecting entrapped oxide particles are recommended. Currently the entrapped oxide particles can be detected only indirectly using either electrolytic polishing which removes the oxide particles and enlarges the remaining holes or by hydrogen annealing in which hydrogen and oxygen react at elevated temperatures producing water vapour.

Fatigue testing of samples containing entrapped oxide particle lines might reveal most reliably the largest oxide particles present in the copper FSW welds.

The amount of entrapped oxide particles in 50 mm thick copper FSW welds can be reduced by oxide removal prior to welding and by the use of shielding gas during FSW.

Entrapped oxide particles in 50 mm thick copper FSW welds could maybe be more widely distributed by displacing the tool so that the original butting faces are on the advancing side during welding and by using higher plunge depth to ensure better mixing of the original oxide layers of the butting faces.

Further studies on the effects of entrapped oxide particles for example by multi-axial tensile and creep testing are needed.

Even if the main features of the microstructure of copper FSW welds have been determined, in this work it is recommended that further studies on the microstructure are performed. Subjects include the behaviour of different precipitate particles (e.g. copper sulphides and phosphides) during FSW and the distribution of different types of grain boundaries as well as their effects.

The comparison of the welds produced by the two competing welding methods (FSW and EBW) for the sealing of spent nuclear fuel copper canisters regarding the mechanical properties in the relevant loading directions occurring in the repository is recommended.

The comparison of heterogeneous weld microstructures (local misorientations, anisotropy, and texture) produced by the two competing welding methods (FSW and EBW) for the sealing of the copper canister for spent nuclear fuel would be informative for the understanding of the long-term properties of the copper canisters.

An important question is why the deformation localizes and subsequently the fracture occurs on the processing line of the FSW weld. There is no apparent reason for this behaviour, such as a change in the grain structure or the existence of small voids.

## 14 REFERENCES

- Abbasi, M., Karimi Taheri, A., and Salehi, M.T. (2001) Growth Rate of Intermetallic Compounds in Al/Cu Bimetal Produced by Cold Roll Welding Process. *Journal of Alloys and Compounds* (319). Pp. 233-241.
- Ahmed, M.M.Z., Wynne, B.P., Rainforth, W.M., and Threadgill, P.L. (2008) Quantifying Crystallographic Texture in the Probe-Dominated Region of Thick-Section Friction-Stir-Welded Aluminium. *Scripta Materialia* 59. Pp. 507-510.
- Andersson, C.-G. and Andrews, R.E. (1999) Fabrication of Containment Canisters for Fuel and Waste Management Co (SKB). 1<sup>st</sup> International Symposium on Friction Stir Welding. Thousand Oaks, CA, USA, 14-16 June.
- Andersson, C.-G., Andrews, R.E., Dance, B.G.I., Russell, M.J., Olden, E.J., and Sanderson, R.M. (2000) A Comparison of Copper Canister Fabrication by the Electron Beam and Friction Stir Processes. 2<sup>nd</sup> International Symposium on Friction Stir Welding. Gothenburg, Sweden, 26-28 June.
- Andersson, H. (2005) Tensile Testing of Friction Stir Welds of Copper at Room Temperature and at 100 °C. Contract Research Report, Corrosion & Metals Research Institute (KiMab). 6 p.
- Arbegast, W.J. (2006) Friction Stir Welding after a Decade of Development – It's Not Just Welding Anymore. *Welding Journal* 85 (3). Pp. 28-35.
- Arbegast, W.J. (2008) A Flow-Partitioned Deformation Zone Model for Defect Formation during Friction Stir Welding. *Scripta Materialia* 58. Pp. 372-376.
- Avettand-Fènoël, M.-N., Taillard, R., Herbelot, C., and Imad, A. (2010) Structure and Mechanical Properties of Friction Stirred Beads of 6082-T6 Al Alloy and Pure Copper. *Materials Science Forum* 638-642. Pp. 1209-1214.

Barmouz, M., Asadi, P., Besharati Givi, M.K., and Taherishargh, M. (2011a) Investigation of Mechanical Properties of Cu/SiC Composite Fabricated by FSP: Effect of SiC Particles' Size and Volume Fraction. *Materials Science and Engineering A* 528. Pp. 1740-1749.

Barmouz, M., Besharati Givi, M.K., and Seyfi, J. (2011b) On the Role of Processing Parameters in Producing Cu/SiC Metal Matrix Composites via Friction Stir Processing: Investigating Microstructure, Microhardness, Wear, and Tensile Behaviour. *Materials Characterization* 62. Pp. 108-117.

Belyakov, A., Miura, H., and Sakai, T. (1998) Dynamic Recrystallization under Warm Deformation of Polycrystalline Copper. *ISIJ International* 38 (6). Pp. 595-601.

Bendzsak, G.J., North, T.H., and Smith, C.B. (2000) An Experimentally Validated 3D Model for Friction Stir Welding. 2<sup>nd</sup> International Symposium on Friction Stir Welding. Gothenburg, Sweden, 26-28 June.

Berbon, P.B., Bingel, W.H., Mishra, R.S., Bampton, C.C., and Mahoney, M.W. (2001) Friction Stir Processing: A Tool to Homogenize Nanocomposite Aluminum Alloys. *Scripta Materialia* 44. Pp. 61-66.

Bird, C. (2003) Ultrasonic Phased Array Inspection Technology for the Evaluation of Friction Stir Welds. 4<sup>th</sup> International Symposium on Friction Stir Welding. Park City, Utah, USA, 14-16 May.

Booth, D.P.P., Starink, M.J., and Sinclair, I. (2007) Analysis of Local Microstructure and Hardness of 13 mm Gauge 2024-T351 AA Friction Stir Welds. *Materials Science and Technology* 23 (3). Pp. 276-284.

Braunović, M. and Alexandrov, N. (1994) Intermetallic Compounds at Aluminium-to-Copper Electrical Interfaces: Effect of Temperature and Electric Current. *IEEE Transactions on Components, Packaging, and Manufacturing Technology A* 17 (1). Pp. 78-85.

Çam, G. (2011) Friction Stir Welded Structural Materials: Beyond Al-Alloys. *International Materials Reviews* 56 (1). Pp. 1-48.

Cavaliere, P., De Santis, A., Panella, F., and Squillace, A. (2009) Effect of Welding Parameters on Mechanical and Microstructural Properties of Dissimilar AA6082-AA2024 Joints Produced by Friction Stir Welding. *Materials and Design* 30. Pp. 609-616.

Cederqvist, L. (2006) FSW to Manufacture and Seal 5 cm Thick Copper Canisters for Sweden's Nuclear Waste. 6<sup>th</sup> International Symposium on Friction Stir Welding. Saint-Sauveur, Canada, 10-13 October.

Cederqvist., L. (2011) Friction Stir Welding of Copper Canisters Using Power and Temperature Control. Doctoral Thesis. Lund University, Faculty of Engineering.

Cederqvist, L. and Andrews, R.E. (2003) A Weld that Lasts for 100,000 Years: FSW of Copper Canisters. 4<sup>th</sup> International Symposium on Friction Stir Welding. Park City, Utah, USA, 14-16 May.

Charit, I. and Mishra, R.S. (2003) High Strain Rate Superplasticity in a Commercial 2024 Al Alloy via Friction Stir Processing. *Materials and Engineering A* 359. Pp. 290-2966.

Chen, Z.W. and Cui, S. (2007) On the Forming Mechanism of Banded Structures in Aluminium Alloy Friction Stir Welds. *Scripta Materialia* 58. Pp. 417-420.

Chen, Z.W. and Maginnes, R. (2004) Formation of Weld Zones during Friction Stir Welding of Aluminium Alloys. 5<sup>th</sup> International Friction Stir Welding Symposium. Metz, France, 14-16 September.

Choi, D.-H., Ahn, B.-W., Lee, C.-Y., Yeon, Y.-M., Song, K., and Jung, S.-B. (2011) Formation of Intermetallic Compounds in Al and Mg Alloys during Friction Stir Spot Welding. *Intermetallics* 19. Pp. 125-130.

Colegrove, P.A. and Shercliff, H.R. (2005) 3-Dimensional CFD Modelling of Flow Round a Threaded Friction Stir Welding Tool Profile. *Journal of Materials Processing and Technology* 169. Pp. 320-327.

Colegrove, P.A., Shercliff, H.R., and Threadgill, P.L. (2003). Modelling and Development of the Trivex™ Friction Stir Welding Tool. 4th International Symposium on Friction Stir Welding. Park City, Utah, USA, 14-16 May.

Colligan, K. (1999) Material Flow Behaviour during Friction Stir Welding of Aluminium. *Welding Journal* 78 (7). Pp. 229-237.

Colligan, K.J., Konkol, P.J., Fisher, J.J., and Pickens, J.R. (2003) Friction Stir Welding Demonstrated for Combat Vehicle Construction. *Welding Journal* 82 (3). Pp. 34-40.

Colligan, K.J. and Mishra, R.S. (2008) A Conceptual Model for the Process Variables Related to Heat Generation in Friction Stir Welding of Aluminum. *Scripta Materialia* 58. Pp. 327-331.

Colligan, K.J. and Pickens, J.R. (2005) Friction Stir Welding of Aluminium Using a Tapered Shoulder Tool. In: Jata, K.V., Mahoney, M.W., Mishra, R.S., and Lienert, T.J. (eds.), *Friction Stir Welding and Processing III*. Pennsylvania, USA: The Minerals, Metals & Materials Society. Pp. 161-170. ISBN 0-87339-584-0.

Cram, D.G., Zurob, H.S., Brechet, Y.J.M., and Hutchinson, C.R. (2009) Modelling Discontinuous Dynamic Recrystallization Using a Physically Based Model for Nucleation. *Acta Materialia* 57. Pp. 5218-5228.

Cui, G.R., Ma, Z.Y., and Li, S.X. (2008) Periodical Plastic Flow Pattern in Friction stir Processed Al-Mg Alloy. *Scripta Materialia* 58. Pp. 1082-1085.

Dalla Torre, F.H., Gazder, A.A., Gu, C.F., Davies, C.H.J., and Pereloma, E.V. (2007) Grain Size, Misorientation, and Texture Evolution of Copper Processed by Equal Channel

Angular Extrusion and the Validity of the Hall-Petch Relationship. *Metallurgical and Materials Transactions* 38 A. Pp. 1080-1095.

Dawes, C.J. (1995) Causing a Stir in Welding Circles. *Sheet Metal Industries*, 72 (9). Pp. 22-26.

Dawes, C.J. and Thomas, W.M. (1999) Development of Improved Tool Designs for Friction Stir Welding of Aluminium. 1<sup>st</sup> International Symposium on Friction Stir Welding. Thousand Oaks, CA, USA, 14-16 June.

De Vuyst, T., Magotte, O., Robineau, A., Goussain, J.-J., and D'Alvice, L.D. (2006) Multi-Physics Simulation of the Material Flow and Temperature Field Around FSW Tool. 6<sup>th</sup> International Symposium on Friction Stir Welding. Saint-Sauveur, Canada, 10-13 October.

Doherty, R.D., Hughes, D.A., Humphreys, F.J., Jonas, J.J., Juul Jensen, D., Kassner, M.E., King, W.E., McNelley, T.R., McQueen, H.J., and Rollett, A.D. (1997) Current Issues in Recrystallization: A Review. *Materials Science and Engineering A* 238. Pp. 219-274.

Dong, P., Lu, F., Hong, J.K., and Cao, Z. (1999) Analysis of Weld Formation Process in Friction Stir Welding. 1<sup>st</sup> International Symposium on Friction Stir Welding. Thousand Oaks, CA, USA, 14-16 June.

Dressler, U., Biallas, G., and Mercado, U.A. (2009) Friction Stir Welding of Titanium Alloy TiAl6V4 to Aluminium Alloy AA2024-T3. *Materials Science and Engineering A* 526. Pp. 113-117.

Dubourg, L., Gagnon, F.-O., Nadeau, F., St-Georges, L., and Jahazi, M. (2006) Process Window Optimization for FSW of Thin and Thick Sheet Al Alloys Using Statistical Methods. 6<sup>th</sup> International Symposium on Friction Stir Welding. Saint-Sauveur, Canada, 10-13 October.

Elrefaey, A., Takahashi, M., and Ikeuchi, K. (2005) Preliminary Investigation of Friction Stir Welding Aluminium/Copper Lap Joints. *Welding in the World* 49 (3/4) Pp. 93-101.

Fehrenbacher, A., Cole, E.G., Zinn, M.R., Ferrier, N.J., Duffie, N.A., and Pfefferkorn, F.E. (2011) Towards Process Control of Friction Stir Welding for Different Aluminium Alloys. In: Mishra, R., Mahoney, M.W., Sato, Y., Hovanski, Y., and Verma, R. (eds.) Friction Stir Welding and Processing VI. Pennsylvania, USA: The Minerals, Metals & Materials Society. Pp. 381-388. ISBN 978-1-11800-201-8.

Fonda, R.W. and Bingert, J.F. (2007) Texture Variations in an Aluminium Friction Stir Weld. *Scripta Materialia* 57. Pp. 1052-1055.

Fonda, R.W., Bingert, J.F., and Colligan, K.J. (2004) Development of Grain Structure during Friction Stir Welding. *Scripta Materialia* 51. Pp. 243-248.

Fujii, H., Yamaguchi, Y., Kiguchi, S., and Nogi, K. (2008) Surface Hardening of Cast Irons by Friction Stir Processing. *Materials Transactions* 49 (12). Pp. 2837-2843.

Fuller, C.B. (2007) Friction Stir Tooling: Tool Materials and Designs. In: Mishra, R.S. and Mahoney, M.W. (eds.) Friction Stir Welding and Processing. Ohio, USA: ASM International. Pp. 7-36. ISBN 0-87170-840-X.

Fuller, C., Mahoney, M., and Bingel, W. (2003) Friction Stir Processing of Aluminium Fusion Welds. 4<sup>th</sup> International Friction Stir Welding Conference. Park City, Utah, USA, 14-16 May.

Fuller, C., Mahoney, M., and Bingel, W. (2004) A Study on Friction Stir Processing Tool Designs for Microstructural Modifications as Demonstrated in Aluminium Fusion Welds. 5<sup>th</sup> International Friction Stir Welding Conference. Metz, France, 14-16 September.

Gao, W., Belyakov, A., Miura, H., and Sakai, T. (1999) Dynamic Recrystallization of Copper Polycrystals with Different Purities. *Materials Science and Engineering A* 265. Pp. 233-239.

Gould, J.E., Lienert, T.J., and Feng, Z. (1998) Recent Development in Friction Stir Welding. *Journal of Materials and Manufacturing* 107. Pp. 1093-1100.

Guerra, M., McClure, J.C., Murr, L.E., and Nunes, A.C. (2001) Metal Flow during Friction Stir Welding. In: Jata, K.V., Mahoney, M.W., Mishra, R.S., Semiatin, S.L., and Field, D.P. (eds.), Friction Stir Welding and Processing. Pennsylvania, USA: The Minerals, Metals & Materials Society. Pp. 25-34. ISBN 0-87339-502-6.

Guerra, M., Schmidt, C., McClure, J.C., Murr, L.E., and Nunes, A.C. (2003) Flow Patterns in Friction Stir Welding. *Materials Characterization* 49. Pp. 95-101.

Hamilton, C., Dymek, S., and Blicharski, M. (2008) A Model of Material Flow during Friction Stir Welding. *Materials Characterization* 59. Pp. 1206-1214.

Hautala, T. (2001) Kuparin kitkahitsaus pyörivällä työkalulla (Friction Stir Welding of Copper). M.Sc. Thesis. Tampere University of Technology, Institute of Materials Science.

Heurtier, P., Jones, M.J., Desrayaud, C., Driver, J.H., Montheillet, F., and Allehaux, D. (2006) Mechanical and Thermal Modelling of Friction Stir Welding. *Journal of Materials Processing Technology* 171. Pp. 348-357.

Humphreys, F.J. and Hatherly, M. (1995) Recrystallization and Related Annealing Processes. Oxford, UK: Elsevier Science Ltd. ISBN 0-08-041884-8.

Hwang, Y.M., Fan, P.L., and Lin, C.H. (2010) Experimental Study on Friction Stir Welding of Copper Materials. *Journal of Materials Processing Technology* 210. Pp. 1667-1672.

Jasthi, B.K., Chen, E.Y., Arbogast, W.J., Heringer, M., Bice, D.R., and Howard, S.M. (2011) Friction Stir Processing of Cast Inconel 718. In: Mishra, R., Mahoney, M.W., Sato, Y., Hovanski, Y., and Verma, R. (eds.) Friction Stir Welding and Processing VI. Pennsylvania, USA: The Minerals, Metals & Materials Society. Pp. 253-264. ISBN 978-1-11800-201-8.

Jene, T., Dobmann, G., Wagner, G., and Eifler, D. (2006) Oxide Fragments in Friction Stir Welds – Distribution and Effects on Crack Initiation. 6<sup>th</sup> International Symposium on Friction Stir Welding. Saint-Sauveur, Canada, 10-13 October.

Kallee, S. and Nicholas, D. (1998) Causing a Stir in the Future. *Welding and Joining Journal*. Pp. 18-21.

Karlsson, L., Larsson, H., Bergqvist, E.-L., and Stoltz, S. (2000) Friction Stir Welding of Dissimilar Al-Alloys. 2<sup>nd</sup> International Symposium on Friction Stir Welding. Gothenburg, Sweden, 26-28 June.

Krishnan, K.N. (2002) On the Formation of Onion Rings in Friction Stir Welds. *Materials Science and Engineering A* 327. Pp. 246-251.

Kumar, K. and Kailas, S.V. (2008) The Role of Friction Stir Weld Tool on Material Flow and Weld Formation. *Materials Science and Engineering A* 485. Pp. 367-374.

Kumar, K. and Kailas, S.V. (2010) Positional Dependence of Material Flow in Friction Stir Welding: Analysis of Joint Line Remnants and Its Relevance to Dissimilar Metal Welding. *Science and Technology of Welding and Joining* 15 (4). Pp. 305-311.

Kwon, Y.-J., Shigematsu, I., and Saito, N. (2003) Production of Ultra-Fine Grained Aluminium Alloy Using Friction Stir Process. *Materials Transactions* 44 (7). Pp. 1343-1350.

Källgren, T. (2010) Investigation and Modelling of Friction Stir Welded Copper Canisters. Doctoral Thesis. Royal Institute of Technology, Department of Materials Science and Engineering.

Källgren, T. and Sandström, R. (2003) Microstructure and Temperature Development in Copper Welded by the FSW-Process. 4<sup>th</sup> International Symposium on Friction Stir Welding. Park City, Utah, USA, 14-16 May.

Lee, I.S., Kao, P.W., and Ho, N.J. (2008) Microstructure and Mechanical Properties of Al-Fe in-situ Nanocomposite Produced by Friction Stir Welding. *Intermetallics* 16. Pp. 1104-1108.

Lee, W.-B., Bang, K.-S., and Jung, S.-B. (2005) Effects of Intermetallic Compound on the Electrical and Mechanical Properties of Friction Welded Cu/Al Bimetallic Joints during Annealing. *Journal of Alloys and Compounds* 390. Pp. 212-219.

Lee, W.-B. and Jung, S.-B. (2004) The Joint Properties of Copper by Friction Stir Welding. *Materials Letters* 58. Pp. 1041-1046.

Lee, W.-B., Schmuecker, M., Mercardo, U.A., Biallas, G., and Jung, S.-B. (2006) Interfacial Reaction in Steel-Aluminium Joints Made by Friction Stir Welding. *Scripta Materialia* 55. Pp. 355-358.

Leonard, A.J. and Lockyer, S.A. (2003) Flaws in Friction Stir Welds. 4<sup>th</sup> International Symposium on Friction Stir Welding. Park City, Utah, USA, 14-16 May.

Li, Y., Murr, L.E., and McClure, J.C. (1999) Flow Visualization and Residual Microstructures Associated with the Friction-Stir Welding of 2024 Aluminium to 6061 Aluminium. *Materials Science and Engineering A* 271. Pp. 213-223.

Liu, P., Shi, Q., Wang, W., Wang, X., and Zhang, Z. (2008) Microstructure and XRD Analysis of FSW Joints for Copper T2/Aluminium 5A06 Dissimilar Materials. *Materials Letters* 62. Pp. 4106-4108.

London, B., Mahoney, M., Bingel, W., Calabrese, M., Bossi, R.H., and Waldron D. (2003) Material Flow in Friction Stir Welding Monitored with Al-SiC and Al-W Composite Markers. In: Jata, K.V., Mahoney, M.W., Mishra, R.S., Semiatin, S.L., and Lienert, T. (eds.) *Friction Stir Welding and Processing II*. Pennsylvania, USA: The Minerals, Metals & Materials Society. Pp. 3-12. ISBN 0-87339-536-0.

Ma, Z.Y., Mishra, R.S., and Mahoney, M.W. (2004) Superplasticity in Cast A356 Induced via Friction Stir Processing. *Scripta Materialia* 50 (7). Pp. 931-935.

Ma, Z.Y., Mishra, R.S., Mahoney, M.W., and Grimes, R. (2003) High Strain Rate Superplasticity in Friction Stir Processed Al-Mg-Zr Alloy. *Materials Science and Engineering A* 351 (1-2). Pp. 148-153.

Mahoney, M. (2003) Flow and Temperature Response during FSP of High Temperature Alloys. Megastir Friction Stir Welding Workshop. Provo, Utah, USA, 19-20 May.

Mahoney, M.W., Bingel, W.H., and Mishra, R.S. (on-line) Microstructural Modification and Resultant Properties of Friction Stir Processed Cast NiAl Bronze. Available at: <http://darpa.mil/dso/thrust/matdev/fsp/prespub.html>. Printed August 18, 2004.

Mahoney, M.W. and Lynch, S.P. (on-line) Friction-Stir Processing. Available at: <http://darpa.mil/dso/thrust/matdev/fsp/prespub.html>. Printed August 18, 2004.

Mahoney, M.W., Mishra, R., and Nelson, T. (2001a) High Strain Rate Superplasticity in Thick Section 7050 Aluminium Created by Friction Stir Processing. 3<sup>rd</sup> International Friction Stir Welding Conference. Kobe, Japan, 27-28 September.

Mahoney, M., Mishra, R.J., Nelson, T., Flintoff, J., Islamgaliev, R., and Hovansky, Y. (2001b) High Strain Rate, Thick Section Superplasticity Created via Friction Stir Processing. In: Jata, K.V., Mahoney, M.W., Mishra, R.S., Semiatin, S.L., Field, D.P. (eds) Friction Stir Welding and Processing. Warrendale, PA, USA, TMS. Pp. 183-194. ISBN 0-87339-502-6, 2001.

McNelley, T.R., Oh-Ishi, K., and Zhilyaev, P. (2007) Microstructures and Properties of Copper Alloys after Friction Stir Welding/Processing. In: Mishra, R.S. and Mahoney, M.W. (eds.) Friction Stir Welding and Processing. Ohio, USA: ASM International. Pp. 155-174. ISBN 0-87170-840-X.

Mishra, R.S. and Ma, Z.Y. (2005) Friction Stir Welding and Processing. Materials Science and Engineering R 50. Pp. 1-78.

Mishra, R.S., Ma, Z.Y., and Charit, I. (2003) Friction Stir Processing: A Novel Technique for Fabrication of Surface Composite. Materials Science and Engineering A 341. Pp. 307-310.

Nandan, R., DebRoy, T., and Bhadeshia, H.K.D.H. (2008) Recent Advances in Friction-Stir Welding – Process, Weldment Structure, and Properties. *Progress in Materials Science* 53. Pp. 980-1023.

Nelson, T. W. (2005) Friction Stir Welding – A Brief Review and Perspective for the Future. In: Jata, K.V., Mahoney, M.W., Mishra, R.S., and Lienert, T. (eds.) *Friction Stir Welding and Processing III*. Pennsylvania, USA: The Minerals, Metals & Materials Society. Pp. 149-159. ISBN 0-87339-548-0.

Okamoto, K., Doi, M., Hirano, S., Aota, K., Okamura, H., Aono, Y., and Ping, T.C. (2001) Fabrication of Backing Plates of Copper Alloy by Friction Stir Welding. 3<sup>rd</sup> International Friction Stir Welding Conference. Kobe, Japan, 27-28 September.

Okamura, H. and Aota, K. (2004) Joining of Dissimilar Materials with Friction Stir Welding. *Welding International* 18 (11). Pp. 852-860.

Okamura, H., Aota, K., Sakamoto, M., Ezumi, M., and Ikeuchi, K. (2002) Behaviour of Oxides during Friction Stir Welding of Aluminium Alloy and Their Effect on Its Mechanical Properties. *Welding International* 16 (4). Pp. 266-275.

Ollonqvist, P. (2007) Microstructural Characterization and Mechanical Properties of Electron Beam Welded Thick Phosphorous Microalloyed Oxygen Free Copper (Cu-OFP). M.Sc. Thesis. Helsinki University of Technology, Laboratory of Engineering Materials.

Ouyang, J., Yarrapareddy, E., and Kovacevic, R. (2006) Microstructural Evolution in the Friction Stir Welded 6061 Aluminium Alloy (T6-Temper Condition) to Copper. *Journal of Materials Processing Technology* 172. Pp. 110-122.

Palm, F., Steiger, H., and Henneböhle, U. (2003) The Origin of Particle (Oxide) Traces in Friction Stir Welds. 4<sup>th</sup> International Symposium on Friction Stir Welding. Park City, Utah, USA, 14-16 May.

Posada, M. (2006) Variable Ductility Evaluation of Friction Stir Processed Nickel Aluminium Bronze Castings. 6<sup>th</sup> International Symposium on Friction Stir Welding. Saint-Sauveur, Canada, 10-13 October.

Prangnell, P.B. and Heason, C.P. (2005) Grain Structure Formation during Friction Stir Welding Observed by the 'Stop Action Technique'. *Acta Materialia* 53. Pp. 3179-3192.

Prasad, Y.V.R.K. and Rao, K.P. (2004) Influence of Oxygen on Rate-Controlling Mechanisms in Hot Deformation of Polycrystalline Copper: Oxygen-free versus Electrolytic Grades. *Materials Letters* 58. Pp. 2061-2066.

Raiko, H. (2005) Disposal Canister for Spent Nuclear Fuel – Design Report. Posiva report 2005-02.

Record, J.H., Covington, J.L., Nelson, T.W., Sorensen, C.D., and Webb, B.W. (2004) Fundamental Characterization of Friction Stir Welding. 5<sup>th</sup> International Friction Stir Welding Conference. Metz, France, 14-16 September.

Reynolds, A.P. (2008) Flow Visualization and Simulation in FSW. *Scripta Materialia* 58. Pp. 338-342.

Ronneteg, U., Cederqvist, L., Rydén, H., Öberg, T, and Müller, C. (2006) Reliability in Sealing of Canister for Spent Nuclear Fuel. Report R-06-26. Swedish Nuclear Fuel and Waste Management Co.

Sarrafi, R., Kokabi, A.H., Abbasi Gharacheh, M., and Shalchi, B. (2011) Evaluation of Microstructure and Mechanical Properties of Aluminium to Copper Friction Stir Butt Welds. In: Mishra, R., Mahoney, M.W., Sato, Y., Hovanski, Y., and Verma, R. (eds.) *Friction Stir Welding and Processing VI*. Pennsylvania, USA: The Minerals, Metals & Materials Society. Pp. 253-264. ISBN 978-1-11800-201-8.

Sato, Y.S., Yamashita, F., Sugiura, Y., Park, S.H.C., and Kokawa, H. (2004) FIB-Assisted TEM Study of an Oxide Array in the Root of a Friction Stir Welded Aluminium Alloy. *Scripta Materialia* 50. Pp. 365-369.

Saukkonen, T., Savolainen, K., Mononen J., and Hänninen, H. (2008) Microstructure and Texture Analysis of Friction Stir Welds of Copper. In: Rollet, A.D. (ed.) Materials Processing and Texture. Ceramic Transactions (Vol. 200). A Collection of Papers Presented at the 15th International Conference on Textures of Materials, 1-6 June, Pittsburgh, Pennsylvania. USA: John Wiley & Sons. Pp 53-60. ISBN 978-0-470-40834-6.

Savolainen, K., Mononen, J., and Hänninen, H. (2006) State-of-the-Art of Friction Stir Processing (FSP). *Steel Research International*, 77 (5), 370-376.

Savolainen, K., Mononen, J., Saukkonen, T., and Hänninen, H. (2005) A Preliminary Study on Friction Stir Welding of Dissimilar Metal Joints of Copper and Aluminium. 6th International Symposium on Friction Stir Welding. Saint-Sauveur, Canada, 10-13 October. 10 p.

Savolainen, K., Mononen, J., Saukkonen, T., Hänninen, H., and Koivula, J. (2004) Friction Stir Weldability of Copper Alloys. 5th International Friction Stir Welding Conference, September 14-16, Metz, France. 19 p.

Savolainen, K., Saukkonen, T., and Hänninen, H. (2010) Optical Strain Measurement of Plastic Strain Localization in Nuclear Waste Copper Canisters. In: Auerkari, P. and Veivo, J. (eds.) Proceedings of Baltica VIII – International Conference on Life Management and Maintenance for Nuclear Power Plants. Espoo, Finland: VTT. Pp. 163-177. ISBN: 978-951-38-77591-6.

Savolainen, K., Saukkonen, T., and Hänninen, H. (2012a) Banding in Copper Friction Stir Weld - Microstructure, Texture and Local Misorientations. *Science and Technology of Welding and Joining* 17. Pp. 111-115.

Savolainen, K., Saukkonen, T., and Hänninen, H. (2012b) Localization of Plastic Deformation in Copper Canisters for Spent Nuclear Fuel 2. Pp. 16-22.

Savolainen, K., Saukkonen, T., Mononen, J., and Hänninen, H. (2008) Entrapped Oxide Particles in Copper Friction Stir Welds. 7th International Symposium on Friction Stir Welding, May 20-22, Awaji Island, Japan. 20 p.

Schmidt, H.N.B., Dickerson, T.L., and Hattel, J.H. (2006) Material Flow in Butt Friction Stir Welds in AA2024-T3. *Acta Materialia* 54. Pp. 1199-1209.

Schneider, J., Beshears, R., and Nunes, A.C.Jr. (2006) Interfacial Sticking and Slipping in the Friction Stir Welding Process. *Materials Science and Engineering A* 435. Pp. 297-304.

Seidel, T.U. and Reynolds, A.P. (2001) Visualization of the Material Flow in AA2195 Friction-Stir Welds Using a Marker Insert Technique. *Metallurgical and Materials Transactions A* 32. Pp. 2879-2884.

Sharma, S.R., Ma, Z.Y., Mishra, R.S. (2004) Effect of Friction Stir Processing on Fatigue Behaviour of A356 Alloy. *Scripta Materialia* 51. Pp. 237-241.

Shercliff, H.R. and Colegrove, P.A. (2002) Modelling of Friction Stir Welding. In: Cerjak, H. (ed.) *Mathematical Modelling of Weld Phenomena 6*. London, UK: Maney Publishing. Pp. 927-974. (Materials Modelling Series). ISBN 1-902653-56-4.

SKB (2005) Friktionssvetsning av kopparkapslar rapport 1 (Friction Stir Welding of Copper Capsules, Report 1). Status Report R-05-73. Swedish Nuclear Fuel and Waste Management Co.

SKB (2007) RD&D Programme 2007 – Programme for Research, Development and Demonstration of Methods for the Management and Disposal of Nuclear Waste. Technical report TR-07-12.

Song, M. and Kovacevic, R. (2003) Thermal Modeling of Friction Stir Welding in a Moving Coordinate System and Its Validation. *International Journal of Machine Tools & Manufacture* 43. Pp. 605-615.

Sorensen, C., Nelson, B., and Sanderson, S. (2007) Properties and Structure of Friction Stir Welded Alloy 718. In: Mishra, R.S., Mahoney, M.W., Lienert, T.J., and Jata, K.V. (eds.) Friction Stir Welding and Processing IV. Pennsylvania, USA: The Minerals, Metals & Materials Society. Pp. 285-293. ISBN 978-0-87339-661-5.

Sterling, C.J., Nelson, T.W., Sorensen, C.D., and Posada, M. (on-line) Effects of Friction Stir Processing on the Microstructure and Mechanical Properties of Fusion Welded 304L Stainless Steel. Available at: <http://darpa.mil/dso/thrust/matdev/fsp/prespub.html>. Printed August 18, 2004.

Su, J.-Q., Nelson, T.W., McNelley, T.R., and Mishra, R.S. (2011) Development of Nanocrystalline Structure in Cu during Friction Stir Processing. Materials Science and Engineering A 528. Pp. 5458-5464.

Sun, Y.F. and Fujii, H. (2010) Investigation of the Welding Parameter Dependent Microstructure and Mechanical Properties of Friction Stir Welded Pure Copper. Materials Science and Engineering A 527. Pp. 6879-6886.

Surekha, K. and Els-Botes, A. (2011) Development of High Strength, High Conductivity Copper by Friction Stir Processing. Materials and Design 32. Pp. 911-916.

Sutton, M.A., Reynolds, A.P., Yang, B., and Taylor, R. (2003) Mode I Fracture and Microstructure for 2024-T3 Friction Stir Welds. Materials Science and Engineering A354. Pp. 6-16.

Tanaka, T., Morishige, T., and Hirata, T. (2009) Comprehensive Analysis of Joint Strength for Dissimilar Friction Stir Welds of Mild Steel to Aluminium Alloys. Scripta Materialia 61. Pp. 756-759.

Thomas, W.M., Nicholas, E.D., and Needham, J.C. (1991) Improvements Relating to Friction Welding. European Patent Application No. 92923936.6.

Threadgill, P.L. (2003) A Review of Friction Stir Welding: Part 2, Selection of Tool Materials. TWI Member Report 761/2003.

Threadgill, P.L. and Nunn, M.E. (2003) A Review of Friction Stir Welding: Part 1, Process Preview. TWI Member Report 760/2003.

Uzun, H., Dalle Donne, C., Argagnotto, A., Ghidini, T., and Gambaro, C. (2005) Friction Stir Welding of Dissimilar Al 6013-T4 to X5CrNi18-10 Stainless Steel. *Materials and Design* 26. Pp. 41-46.

Vugrin, T., Schmücker, M., and Staniek, G. (2005) Root Flaws of Friction Stir Welds – An Electron Microscopy Study. In: Jata, K.V., Mahoney, M.W., Mishra, R.S., and Lienert, T.J. (eds.) *Friction Stir Welding and Processing III*. Pennsylvania, USA: The Minerals, Metals & Materials Society. Pp. 227-284. ISBN 0-87339-584-0.

Warsinski, K., West, M., Freeman, J., and Curtis, T. (2011) Investigation of Lazy S Feature in Self-Reacting Tool Friction Stir Welds. In: Mishra, R., Mahoney, M.W., Sato, Y., Hovanski, Y., and Verma, R. (eds.) *Friction Stir Welding and Processing VI*. Pennsylvania, USA: The Minerals, Metals & Materials Society. Pp. 171-176. ISBN 978-1-11800-201-8.

Watanabe, T., Takayama, H., and Yanagisawa, A. (2006) Joining of Aluminium Alloy to Steel by Friction Stir Welding. *Journal of Materials Processing Technology* 178. Pp. 342-349.

Xie, G.M., Ma, Z.Y., and Geng, L. (2007) Development of a Fine-Grained Microstructure and the Properties of a Nugget Zone in Friction Stir Welded Pure Copper. *Scripta Materialia* 57. Pp. 73-76.

Xu, S. and Deng, X. (2008) A Study of Texture Patterns in Friction Stir Welds. *Acta Materialia* 56. Pp. 1326-1341.

Xue, P., Ni, D.R., Wang, D., Xiao, B.L., and Ma, Z.Y. (2011a) Effect of Friction Stir Welding Parameters on the Microstructure and Mechanical Properties of the Dissimilar Al-Cu Joints. *Materials Science and Engineering A* 528. Pp. 4683-4689.

Xue, P., Xiao, B.L., Ni, D.R., and Ma, Z.Y. (2010) Enhanced Mechanical Properties of Friction Stir Welded Dissimilar Al-Cu Joint by Intermetallic Compounds. *Materials Science and Engineering A* 527. Pp. 5723-5727.

Xue, P., Xiao, B.L., Zhang, Q., and Ma, Z.Y. (2011b) Achieving Friction Stir Welded Pure Copper Joints with Nearly Equal Strength to the Parent Metal via Additional Rapid Cooling. *Scripta Materialia* 64. Pp. 1051-1054.

Yan, J., Sutton, M.A., and Reynolds, A.P. (2004) Process-Structure-Property Relationship for Nugget and HAZ Regions of AA2524-T351 FSW Joints. 5<sup>th</sup> International Friction Stir Welding Conference. Metz, France, 14-16 September.

Yang, B., Yan, J., Sutton, M.A., and Reynolds, A.P. (2004) Banded Microstructure in AA2024-T351 and AA2524-T351 Aluminium Friction Stir welds – Part I. Metallurgical Studies. *Materials Science and Engineering A* 364. Pp. 55-65.

Zettler, R., dos Santos, J.F., Donath, T., Beckmann, F., and Lohwasser, D. (2006) Material Flow in Friction Stir Butt Welded Aluminium Alloys. 6<sup>th</sup> International Symposium on Friction Stir Welding. Saint-Sauveur, Canada, 10-13 October.

Zettler, R., Vugrin, T., and Schmücker, M. (2010) Effects and Defects in Friction Stir Welds. In: Lohwasser, D. and Chen, Z. (eds.) *Friction Stir Welding – From Basics to Applications*. Woodhead Publishing Limited, UK. Pp. 245-276. ISBN: 978-1-84569-450-0.

Zhang, H.-W., Zhang, Z., Bie, J., Zhou, L., and Chen, J.-T. (2006) Effect of Viscosity on Material Behaviour in Friction Stir Welding Process. *Transactions of Nonferrous Metals Society China* 16. Pp. 1045-1052.

Zhang, H.W., Zhang, Z., and Chen, J.T. (2005) The Finite Element Simulation of the Friction Stir Welding Process. *Materials Science and Engineering A* 403. Pp. 340-348.

Zhang, H.W., Zhang, Z., and Chen, J.T. (2007) 3D Modelling of Material Flow in Friction Stir Welding under Different Process Parameters. *Journal of Materials Processing Technology* 183. Pp. 62-70.





ISBN 978-952-60-4500-9 (pdf)  
ISSN-L 1799-4934  
ISSN 1799-4942 (pdf)

**Aalto University**  
**School of Engineering**  
**Department of Engineering Design and Production**  
[www.aalto.fi](http://www.aalto.fi)

**BUSINESS +  
ECONOMY**

**ART +  
DESIGN +  
ARCHITECTURE**

**SCIENCE +  
TECHNOLOGY**

**CROSSOVER**

**DOCTORAL  
DISSERTATIONS**